

國立交通大學

電子工程學系 電子研究所碩士班

碩士論文

脈衝雷射沉積鋁氧電阻層

全透式電阻式記憶體研究

**Pulse-laser deposition of LaAlO_3 as resistive switching layer
of fully transparent resistive random access memory**

研究生：黃俊傑

指導教授：張國明 博士

中華民國 九十九 年 八 月

脈衝雷射沉積鋁氧電阻層
全透式電阻式記憶體研究

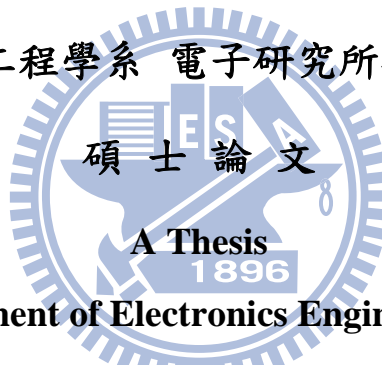
**Pulse-laser deposition of LaAlO₃ as resistive switching layer
of fully transparent resistive random access memory**

研究生：黃俊傑 Student：Jun-Jie Huang

指導教授：張國明 博士 Advisor：Dr. Kow-Ming Chang

國立交通大學

電子工程學系 電子研究所碩士班



Submitted to Department of Electronics Engineering and Institute of
Electronics

College of Electrical and Computer Engineering

National Chiao Tung University

in Partial Fulfillment of the Requirements

for the Degree of Master in

Electronics Engineering

August 2010

Hsinchu, Taiwan

中華民國九十九年八月

脈衝雷射沉積鋁氧電阻層 全透式電阻式記憶體研究

學生：黃俊傑

指導教授：張國明 博士

國立交通大學

電子工程學系 電子研究所碩士班

摘 要

隨著數位科技的日新月異，非揮發性記憶體在生活中扮演著極重要的角色，透明化產品也逐漸掀起潮流。快閃式記憶體雖然是目前最大宗的非揮發性記憶體，但它有其不可微縮的極限，包含高操作電壓，低存取速度和較短的保存時限。電阻式記憶體具有簡單結構，低操作電壓和高微縮能力的優點，故很可能成為下一個世代的記憶體。

三氧化鋁鍍為下個世代互補式金屬氧化物半導體的熱門高介電質材料。三氧化鋁鍍具有高介電常數、不容易與矽反應、在製程中有低的擴散率且不會在介面和矽產生二氧化矽而造成介電常數等效下降等優點。如果能利用三氧化鋁鍍作為電阻式記憶體的 material，將很容易跟互補式金屬氧化物半導體製程相容。

在本論文中，我們成功使用 ITO/三氧化鋁鍍/ITO 製程結構和材料探討記憶體的操作特性和並藉由電操作特性提出機制。

Pulse-laser deposition of LaAlO_3 as resistive switching layer of fully transparent resistive random access memory

Student: Jun-Jie Huang

Advisor: Dr. Kow-Ming Chang

Department of Electronics Engineering and Institute of Electronics
National Chiao Tung University, Hsinchu, Taiwan

ABSTRACT

With the arrival of Digital Age, nonvolatile memory (NVM) plays an important role in our life, and the transparent products are also a trend. The flash memory is the mainstream NVM so far, but it meets the challenge for scaling down, including high operation voltage, low operation speed, and poor retention. Resistive random access memory (RRAM) has many advantages including simple structure, low operation voltage, and scaling down. RRAM is possible to become the next generation NVM.

LaAlO_3 is a candidate high k material for next COMS generation. LaAlO_3 is a promising material due to its higher k , lack of reactivity with Si, and larger band offset with Si. Particularly, LaAlO_3 has much lower atomic diffusion rate and fewer tendencies to form the SiO_2 -based interfacial layer during processing. If we can use LaAlO_3 as a next generation memory, it is compatible with CMOS processes.

In this paper, we succeed in the research of the ITO/ LaAlO_3 /ITO as the RRAM and proposed a mechanism by the electrical properties.

誌 謝

經過這兩年的碩士班學習，不僅讓我學到研究的方法，也讓我更加了解自己對元件物理領域的興趣。首先感謝 張國明教授在這兩年的指導並提供舒適的學習環境。也感謝長庚大學 劉國辰教授在實驗方面的提供和討論，激發了我多元的想法與敏銳的思考。

其次感謝曾文賢學長，在研究過程中不斷的指導和討論。也感謝長庚的學弟蕭煌錡在實驗過程中不斷的幫忙，讓實驗過程進行得更順利。感謝實驗室的同學和學弟，在碩士班這兩年帶來歡笑和鼓勵，讓我在做實驗的時候解決很多問題，進而完成論文。

此外，感謝國家奈米元件實驗室 (NDL) 與交通大學奈米中心 (NCTU - NFC) 的服務人員以及曾經訓練我機台的學長姐和工程師，因為有你們熱心的幫忙和服務，才能讓我順利進行實驗。

最後，感謝我的家人和女友錢乃瑜，在我挫折的時後給予支持，在我開心的時候分享喜悅，也因為你們，我才能全力以赴在課業上努力，謝謝你們。

Contents

摘 要 ii

ABSTRACT iii

Table Contents vii

Figure Contents vii

Chapter1 Introduction 1

1.1 Introduction to nonvolatile memory 1

1.2 Introduction to resistive random access memory 3

1.3 Conduction mechanisms 3

1.4 Resistive switching mechanisms 6

Chapter 2 Experimental Detail 16

2.1 DC magnetron sputtering system 16

2.2 Pulse Laser Deposition (PLD) system 17

2.3 Fabrication of resistive switching memory device 21

2.4 Material analysis 22

2.5 Electrical analysis 25

Chapter 3 Result and Discussion of Investigation of LaAlO₃ Thin

Film with Various Oxygen Pressures 30

3.1 Introduction 30

3.2 Electrical characterization 30

3.3 Physical Characterization 31

Chapter 4 Results and Discussion of the LaAlO₃ as a Resistive

Switching Layer in RRAM 49

4.1 Specified some resistive switching parameters 49

4.2 Comparison of switching properties between LAO thin films

with different oxygen pressure	50
4.3 Two pads test to detect the rupture position of the filament	53
4.4 Proposed resistive switching mechanisms for ITO/LAO/ITO structure	54
Chapter 5 Conclusion	81
Chapter 6 Future Work	82
References	83

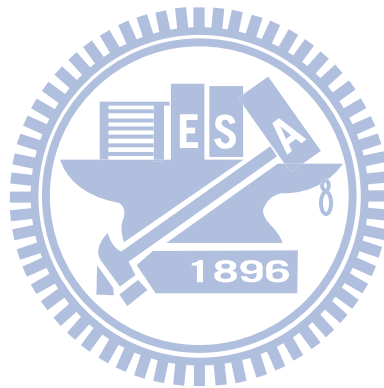


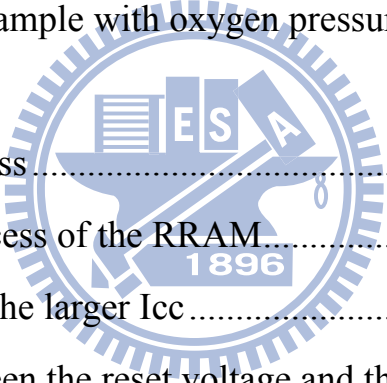
Table Contents

Table 3- 1	33
------------------	----

Figure Contents

Fig. 1- 1 Flash memory cell structure [1]	11
Fig. 1- 2 The polarization hysteresis curve of the ferroelectric material..	11
Fig. 1- 3 Valence change systems [1]	12
Fig. 1- 4 Evidences for the filament model by CAFM [8]	12
Fig. 1- 5 Evidences for the filament model by CAFM [9]	13
Fig. 1- 6 Schematic for charge trapping and detrapping I-V curve [10] ..	13
Fig. 1- 7 Schematic for phase change mechanism.....	14
Fig. 1- 8 Schematic for electrochemical metallization mechanism [10] ..	14
Fig. 1- 9 Schematic for schottky barrier mechanism [12].....	15
Fig. 2- 1 Magnetron sputtering system.....	27
Fig. 2- 2 PLD deposition system	27
Fig. 2- 3 Process flow of the MIM structure	28
Fig. 2- 4 Atomic Force Microscopy.....	29
Fig. 2- 5 Scanning electron microscopy system.....	29
Fig. 3- 1 Leakage current of LAO films deposited under various oxygen pressures.....	33
Fig. 3- 2 Ohmic conduction fitting of the sample in oxygen pressure of the 7×10^{-3} torr.....	34
Fig. 3- 3 Ohmic conduction fitting of the sample in oxygen pressure of the 1.4×10^{-2} torr.....	34

Fig. 3- 4 Ohmic conduction fitting of the sample in oxygen pressure of the 2.8×10^{-2} torr.....	35
Fig. 3- 5 Schottky conduction fitting of the sample in oxygen pressure of the 7×10^{-3} torr.....	35
Fig. 3- 6 Schottky conduction fitting of the sample in oxygen pressure of the 1.4×10^{-2} torr.....	36
Fig. 3- 7 Schottky conduction fitting of the sample in oxygen pressure of the 2.8×10^{-2} torr.....	36
Fig. 3- 8 Breakdown negative voltage with three samples with various oxygen pressures.....	37
Fig. 3- 9 Breakdown positive voltage with three samples with various oxygens.....	37
Fig. 3- 10 Breakdown voltage of the sample with oxygen pressure of 7×10^{-3} torr in various temperatures.....	38
Fig. 3- 11 Breakdown voltage of the sample with oxygen pressure of 1.4×10^{-2} torr in various temperatures.....	38
Fig. 3- 12 Breakdown voltage of the sample with oxygen pressure of 2.8×10^{-2} torr in various temperature.....	39
Fig. 3- 13 Power to breakdown voltage of the sample with oxygen pressure of 7×10^{-3} torr in various temperatures.....	39
Fig. 3- 14 Power to breakdown voltage of the sample with oxygen pressure of 1.4×10^{-2} torr in various temperatures.....	40
Fig. 3- 15 Power to breakdown voltage of the sample with oxygen pressure of 2.8×10^{-2} torr in various.....	40
Fig. 3- 16 AFM of the sample with oxygen pressure of 7×10^{-3} torr.....	41
Fig. 3- 17 AFM of the sample with oxygen pressure of 1.4×10^{-2} torr.....	41

Fig. 3- 18 AFM of the sample with oxygen pressure of 1.4×10^{-2} torr	42
Fig. 3- 19 SEM of the sample with oxygen pressure of 7×10^{-3} torr	42
Fig. 3- 20 SEM of the sample with oxygen pressure of 1.4×10^{-2} torr	43
Fig. 3- 21 SEM of the sample with oxygen pressure of 2.8×10^{-2} torr	43
Fig. 3- 22 XRD of the samples with different oxygen pressure	44
Fig. 3- 23 XPS result of La 3d peak with different oxygen pressure	44
Fig. 3- 24 XPS result of La 3d peak with different oxygen pressure	45
Fig. 3- 25 XPS result of La 3d peak with different oxygen pressure	45
Fig. 3- 26 TEM of the sample with oxygen pressure of 7×10^{-3} torr	47
Fig. 3- 27 TEM of the sample with oxygen pressure of 1.4×10^{-2} torr	47
Fig. 3- 28 TEM of the sample with oxygen pressure of 2.8×10^{-2} torr	48
	
Fig. 4- 1 Forming process	56
Fig. 4- 2 Operation process of the RRAM	56
Fig. 4- 3 Heat effect in the larger I_{cc}	57
Fig. 4- 4 Relation between the reset voltage and the current in the LAO thin film with oxygen pressure of 7×10^{-3} torr	57
Fig. 4- 5 Relation between the reset voltage and the current in the LAO Thin film with oxygen pressure of 1.4×10^{-2} torr	58
Fig. 4- 6 Relation between the reset voltage and the current in the LAO Thin film with oxygen pressure of 2.8×10^{-2} torr	58
Fig. 4- 7 Detail of the reset current from different magnitude of the reset voltage in LAO thin film with oxygen pressure of 7×10^{-3} torr	59
Fig. 4- 8 Detail of the reset current from different magnitude of the reset voltage in LAO thin film with oxygen pressure of 1.4×10^{-2} torr	59
Fig. 4- 9 Detail of the reset current from different magnitude of the reset	

	voltage in LAO thin film with oxygen pressure of 2.8×10^{-2} torr	60
Fig. 4- 10	Relation of the HRS and the different magnitude of the reset voltage in LAO thin film with oxygen pressure of 7×10^{-3} torr...	60
Fig. 4- 11	Relation of the HRS and the different magnitude of the reset voltage in LAO thin film with oxygen pressure of 1.4×10^{-2} torr	61
Fig. 4- 12	Relation of the HRS and the different magnitude of the reset voltage in LAO thin film with oxygen pressure of 2.8×10^{-2} torr	61
Fig. 4- 13	Relation between the negative voltage and the current in the LAO thin film with oxygen pressure of 7×10^{-3} torr.....	62
Fig. 4- 14	Relation between the negative voltage and the current in the LAO thin film with oxygen pressure of 1.4×10^{-2} torr.....	62
Fig. 4- 15	Relation between the negative voltage and the current in the LAO thin film with oxygen pressure of 2.8×10^{-2} torr.....	63
Fig. 4- 16	Detail of the set current from different magnitude of the negative voltage in LAO thin film with oxygen pressure of 7×10^{-3} torr.....	63
Fig. 4- 17	Detail of the set current from different magnitude of the negative voltage in LAO thin film with oxygen pressure of 1.4×10^{-2} torr.....	64
Fig. 4- 18	Detail of the set current from different magnitude of the negative voltage in LAO thin film with oxygen pressure of 2.8×10^{-2} torr.....	64
Fig. 4- 19	Relation of the LRS and the different magnitude of the negative voltage in LAO thin film with oxygen pressure of 7×10^{-3} torr.....	65
Fig. 4- 20	Relation of the LRS and the different magnitude of the	

negative voltage in LAO thin film with oxygen pressure of 1.4x10 ⁻² torr.....	65
Fig. 4- 21 Relation of the LRS and the different magnitude of the negative voltage in LAO thin film with oxygen pressure of 2.8x10 ⁻² torr.....	66
Fig. 4- 22 Relation of the LRS and the different magnitude of the compliance current in LAO thin film with oxygen pressure of 7x10 ⁻³ torr.....	66
Fig. 4- 23 Relation of the LRS and the different magnitude of the compliance current in LAO film with oxygen pressure of 1.4x10 ⁻² torr.....	67
Fig. 4- 24 Relation of the LRS and the different magnitude of the compliance current in LAO film with oxygen pressure of 2.8x10 ⁻² torr.....	67
Fig. 4- 25 Endurance of the ITO/LAO/ITO sample with oxygen pressure of 7x10 ⁻³ torr	68
Fig. 4- 26 Endurance of the ITO/LAO/ITO sample with oxygen pressure of 1.4x10 ⁻² torr	68
Fig. 4- 27 Endurance of the ITO/LAO/ITO sample with oxygen pressure of 2.8x10 ⁻² torr	69
Fig. 4- 28 Eetention of the ITO/LAO/ITO sample with oxygen pressure of 7x10 ⁻³ torr	69
Fig. 4- 29 Eetention of the ITO/LAO/ITO sample with oxygen pressure of 1.4x10 ⁻² torr	70
Fig. 4- 30 Retention of the ITO/LAO/ITO sample with oxygen pressure of 2.8x10 ⁻² torr	70

Fig. 4- 31 V_{set}/V_{reset} distribution of the sample with oxygen pressure of 7×10^{-3} torr.....	71
Fig. 4- 33 V_{set}/V_{reset} distribution of the sample with oxygen pressure of 2.8×10^{-2} torr.....	72
Fig. 4- 34 Relation between the HRS and the temperature show semiconductor-like behavior.....	72
Fig. 4- 35 Frenkel Poole behavior of the HRS	73
Fig. 4- 36 Relation between the HRS and the temperature show metallic behavior.....	73
Fig. 4- 37 Ohmic behavior of the LRS	74
Fig. 4- 38 Schematic diagram of a cross section of the sample structure for the I-V measurement of the ITO/LAO/ITO/LAO/ITO sample	74
Fig. 4- 39 Abnormal forming of the two pads test.....	75
Fig. 4- 40 Resistances change of the different configuration after abnormal forming of the two pads test	75
Fig. 4- 41 Resistances change of the different configuration After the subsequent reset and set processes of the two pads test	76
Fig. 4- 42 Pristine state of the ITO/LAO/ITO structure	76
Fig. 4- 43 E-Field generated from the external bias lead to oxygen migration	77
Fig. 4- 44 Oxygen migrate from the cathode to the anode.....	77
Fig. 4- 45 More vacancies migrate from the anode to the cathode	78
Fig. 4- 46 Regions near the anode and the cathode show different polarity and resistance result from the migration of the oxygen.....	78
Fig. 4- 47 Reverse polarity of the E-Field leads to the migration of the	

oxygen from the cathode the to the anode	79
Fig. 4- 48 HRS after the reset operation	79
Fig. 4- 49 E-Field makes the oxygen migration from the virtual cathode to the anode	80
Fig. 4- 50 LRS after the set operation.....	80



Chapter1 Introduction

1.1 Introduction to nonvolatile memory

With the popularity of various portable electronics, nonvolatile memories play an important role in our life. An ideal nonvolatile memory has the following advantages: low operation voltage, high operation speed, high endurance, long retention time, and simple structure. There are many kinds of advanced nonvolatile memories, but no one can meet all requests.

1.1.1 Flash

The Flash memory is the mainstream nonvolatile memory, including NOR and NAND flash. The primary structure of the flash memory is a MOSFET-like transistor with an inner floating gate as shown in Fig 1-1. The data stored in the floating gate is by the current charges. When charge stored in the floating gate, it changes the threshold voltage (V_t) of the cell, so the modified V_t causes the cell to be on or off region.

NOR and NAND flash are different from their properties and applications. NOR flash has the advantage for high speed, so it is suitable for the mobile electronics. NAND flash has the advantage for high density, so it is suitable for the large data storage.

With the trend for scaling down the cell size, flash memories meet the challenge due to high operation voltage, low operation speed, and poor retention time. There are many advanced nonvolatile memories to become the next generation memories including ferroelectric random access memory (FeRAM), The magnetic random access memory

(MRAM), and Resistive random access memory (RRAM).

1.1.2 MRAM

The magnetic random access memory (MRAM) is also an advanced nonvolatile memory. The data stored in the magnetic material is not by the charges but by the magnetic storage elements. The basic MRAM cell consists of two magnetic layers sandwiching a thin tunneling layer. One of the two magnetic layers is a permanent magnet. By applying external field, the other's field will be changed. To read data, a small nondestructive voltage is applied to recognize the resistance state.

1.1.3 FeRAM

Ferroelectric random access memory (FeRAM) is possible being next generation nonvolatile memory. A ferroelectric material has two type polarizations. The dielectric constant of a ferroelectric is typically much higher than that of a linear dielectric because of the effects of semi-permanent electric dipoles formed in the crystal structure of the ferroelectric material. When an external bias is applied across the ferroelectric material, the dipoles can be aligned with the external bias. By changing the dipoles direction, we can store "0" or "1" information in the material.

The polarization hysteresis curve of the ferroelectric material is shown in [Fig 1-2\[1\]](#).

1.1.4 RRAM

Resistive random access memory (RRAM) is another candidate for

the next generation nonvolatile memory devices. The details of the RRAM are discussed in next section.

1.2 Introduction to resistive random access memory

Resistive random access memory (RRAM) is one of the most promising candidates for next generation storage applications because of its nonvolatility, simple structure, great scalability potential, and compatibility with current complementary metal oxide semiconductor technology.

1.3 Conduction mechanisms

RRAM has been research for a period of time, but the mechanism of the resistive switching (RS) is not carrier up to now. The theories to explain RS character are conduction mechanisms. The conduction mechanisms mostly involved are Schottky emission, Frenkel-Poole emission, Tunnel or Field emission, Space-charge-limited-current, Ohmic conduction, and Ionic conduction. The six basic conduction mechanisms in insulator are summarized in [Table1-1](#).

1.3.1 Schottky emission

The Schottky emission is caused by thermionic emission of carriers across the barrier height of the interfaces, and through the dielectric film. Temperature is the key factor that energetic carriers can jump across the barrier easily. If the carrier conduct in this mechanism, the plot of $\ln |$

J/T^2 | versus $1/T$ in a specific voltage is a straight line, and the slop can be used to determine the permittivity of the insulator. The formula of Schottky emission is expressed as below:

$$J = A^* T^2 \exp \left[\frac{-q \left(\phi_b - \sqrt{qV / 4\pi\epsilon_r \epsilon_0 d} \right)}{kT} \right]$$

where A^* denotes Richardson constant, Φ_b is the Schottky barrier height, ϵ_0 is the permittivity of free space, ϵ_r is the dynamic dielectric constant, V is the external applied voltage and d is the insulator thickness.

1.3.2 Frenkel-Poole emission

The Frenkel-Poole (F-P) emission is caused by field-enhanced carrier hopping by defect states in the dielectric material, and the barrier lowering is twice as large as that in Schottky emission mechanism. If the carrier conduct in this mechanism, the plot of $\ln | J |$ versus $1/T$ in a specific voltage and $\ln | J/V |$ versus $V^{1/2}$ at a specific temperature are straight lines. The formula of F-P emission is expressed as below:

$$J = BV \exp \left[\frac{-q \left(\phi_t - \sqrt{qV / 4\pi\epsilon_r \epsilon_0 d} \right)}{kT} \right]$$

Where B denotes a material-related constant, Φ_t is the trap level, ϵ_0 is the permittivity of free space, ϵ_r is the dynamic dielectric constant, V is the

external applied voltage and d is the insulator thickness.

1.3.3 Tunnel or field emission

The tunnel or field emission is caused by carriers through the barrier. Voltage is the key factor that carrier can conduct through the barrier easily. If carrier conduct in this mechanism, the plot of $\ln | J/V^2 |$ versus $1/V$ is a straight line.

1.3.4 Space-charge-limited current

The theory of space-charge-limited current (SCLC) was first given by Mott and Gurney (1940) and has been extended by many authors. This mechanism is attributed to defects in the dielectric. Trap states is the key factor that carrier can conduct in different degrees. The formula of SCLC is expressed as below:

$$J = \frac{9}{8} \mu \epsilon_r \epsilon_0 \frac{V^2}{L^3} \theta_0$$

Where μ is the free carrier mobility, ϵ_r is the dielectric constant of the material, V is the external applied voltage, L is the insulator thickness, and θ is the ratio of free electrons to trapped electrons.

1.3.5 Ohmic conduction

The Ohmic conduction is caused by thermionic carriers. It happened when the injected carrier is far less than the thermionic carriers. Temperature is another effect in this mechanism. The plot of $\ln | J |$

versus $\ln |V|$ at fixed temperature and $\ln |J|$ versus $1/T$ in a specific voltage are straight lines. The formula of Ohmic conduction is expressed as below:

$$J = aV \exp\left(-\frac{c}{T}\right)$$

Where a and c denote constants, V is the external voltage, and T is the absolute temperature.

1.4 Resistive switching mechanisms

1.4.1 Oxygen movement mechanism

In many transition metal oxides, oxygen ions defect are much more mobile than cations.

When low voltage is applied on the electrode, the line of I-V plot is straight according to ohmic principle. If larger voltage is applied, the line will not obey the ohmic conduction due to large change of oxygen concentration dramatically.

When larger bias is applied, oxygen ions drift toward the anode, causing the region near the anode become p-conductivity, and the region near the cathode become n-conductivity. The set of mass action equations leads to a strong depletion of the oxygen vacancy concentration in a somewhat larger anodic region. In this situation, the large region of n-conductivity is called “virtual cathode”. This “virtual cathode” moves towards the anode and will finally form a conductive path. When the virtual cathode approaches the anode, the resistance of the dielectric decreases dramatically, and the forming process is completed. Once the

electroforming is completed, the bipolar resistance switching (BRS) takes place between the virtual cathode and the anode when reverse external bias is applied.

This redox mechanism has recently been confirmed in detail [2][3][4].

The plot presented this mechanism is shown in Fig 1-3[2].

1.4.2 Filament model

So far, the resistive switching mechanism is believed because of the formation and rupture of the conducting filaments. This model has been proposed since 1970's. The most obvious evidences for the filament model are electron-beam-induced current model and C-AFM, as shown in Fig 1-4[8] and Fig 1-5[9].

When voltage sweep was applied on the anode, the carrier injected from the anode. The carriers diffuse into the oxide and grow toward the cathode, and many branches form, which may have a common base at the anode interface. When one of the branches gets to the anode, the resistance of the dielectric decreases dramatically, and the resistance switching to LRS is formed. The conducting path is so called "filament". Basically, the common base region of the filament is strong, but the branch of the filament is weak. The weakly formed branches of the filament can easily be thermally ruptured after subsequent I-V measurements, resulting in an HRS of the resistance switching.

This filament mechanism has recently been confirmed in detail [5]-[8].

1.4.3 Charge trapping and detrapping mode

This RS mechanism is caused by the charge transfer, trapping and detrapping in the insulator. It is widely explained for RS binary oxides and perovskite oxides.

Defects play an important role in this mechanism. When defect states are empty, they can capture the current electrons, leading to low electron concentration and HRS. After all the defect states are filled, the current electrons are free to drift through the oxide, leading to high electron concentration and LRS. Hence, the resistance change is dominated by the bulk defect states.

This charge trapping and detrapping model has recently been confirmed in detail [9].

The plot presented this mechanism is shown in Fig 1-6[9].

1.4.4 Phase change mechanism

The phase change mechanism exhibits two different phases, amorphous and polycrystalline, to store data information. In reset process, a high magnitude current pulse with short tailing edge is applied on the programmable volume of the phase change material. The temperature of the material exceeds the melting point which eliminates the polycrystalline order in the volume. When the reset pulse is terminated, the device quenches to “freeze in” the disordered structural state. This quench time about several nanoseconds is determined by thermal environment of the device and the fall time of the reset pulse. In set process, a moderate magnitude current pulse with sufficient duration is applied to maintain the device temperature for crystal growth.

This phase change mechanism has recently been confirmed in detail [10]-[13].

The plot presented this mechanism is shown in Fig 1-7[13].

1.4.5 Electrochemical metallization mechanism

This mechanism relies on an electrochemically active electrode metal such as Ag and Cu. The drift of the highly mobile cations result in the metallic dendrites which form highly conductive bridges and the system switches to LRS. By applying the reverse bias, the conducting bridge electrochemical dissolve, and the system switches to HRS.

This electrochemical metallization mechanism has recently been confirmed in detail [14] [15].

The plot presented this mechanism is shown in Fig1-8[15].

1.4.6 Schottky barrier modulation mechanism

Schottky barriers formed between oxide and metal electrodes and are different from various materials. For p-type semiconductor, metal with lower work function has higher schottky barriers for holes. For n-type semiconductor, metal with high work function has higher schottky barriers for electrons.

For schottky barrier mechanism, the interface between the oxide and metal plays an important role for resistive switching. When the external bias applied on the metal, electrons were injected into the oxide, and a large amount of electrons are accumulated into the interface states. The net charges in the interface states resulted in a modulation of the schottky barrier high, because the band bending was affected by the net

charges, leading to HRS or LRS.

This Schottky barrier modulation mechanism has recently been confirmed in detail [16][17][18][19].

The plot presented this mechanism is shown in Fig1-9[17].



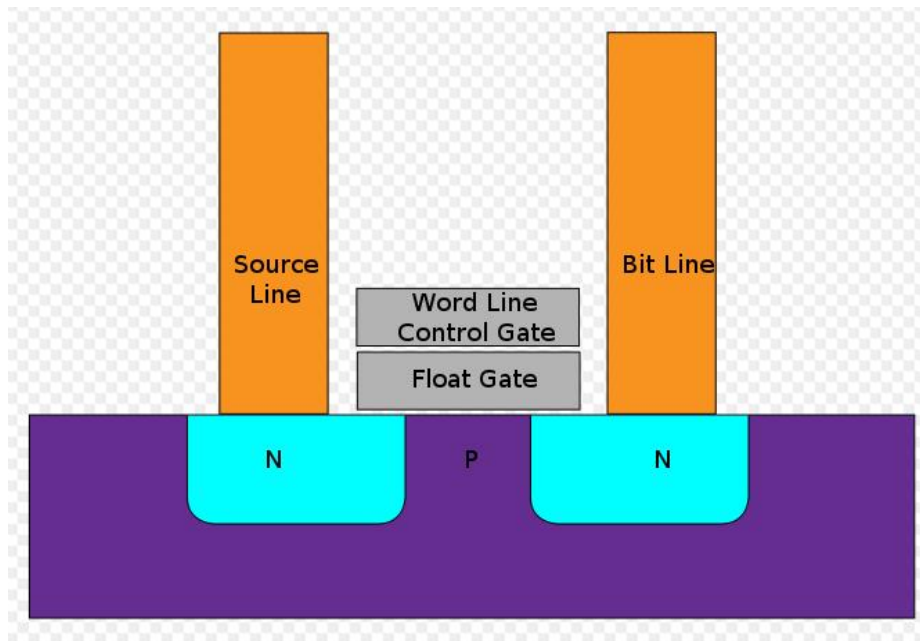


Fig. 1- 1 Flash memory cell structure

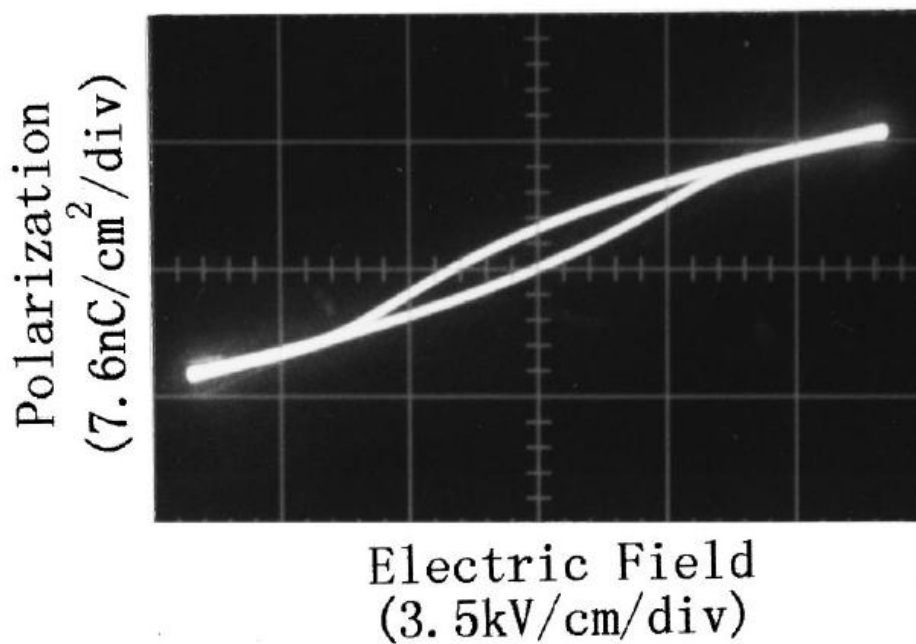
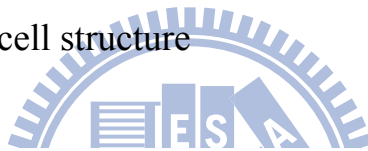


Fig. 1- 2 The polarization hysteresis curve of the ferroelectric material [1]

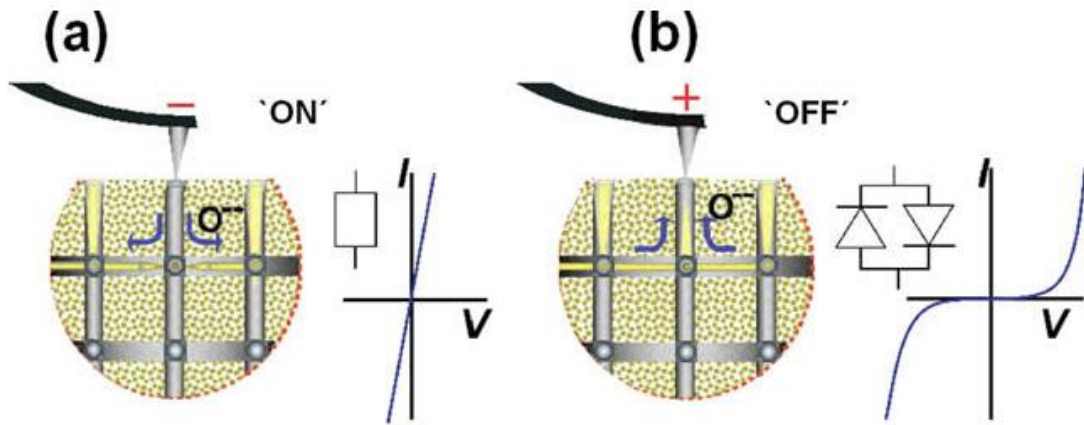


Fig. 1- 3 Valence change systems [2]

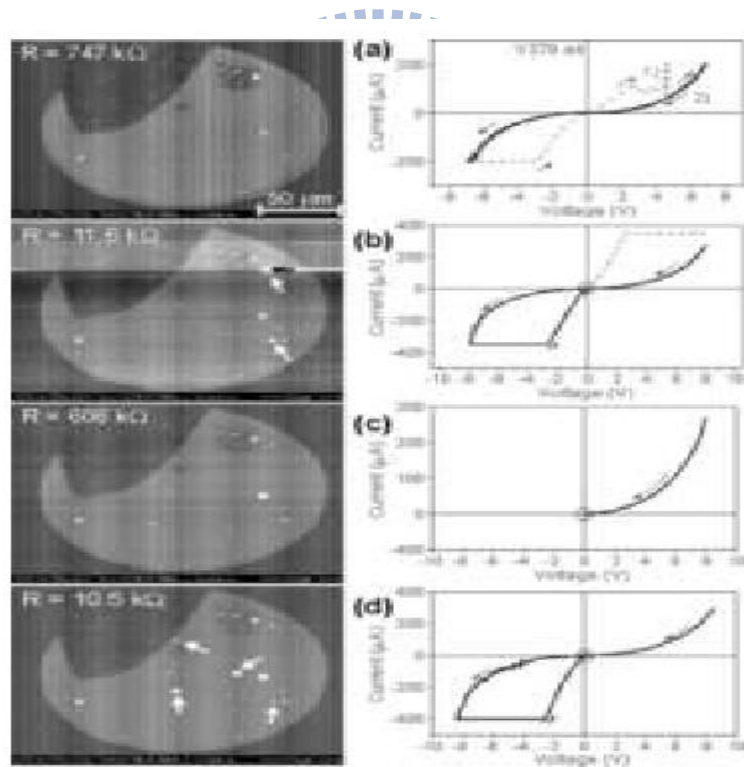


Fig. 1- 4 Evidences for the filament model by CAFM [8]

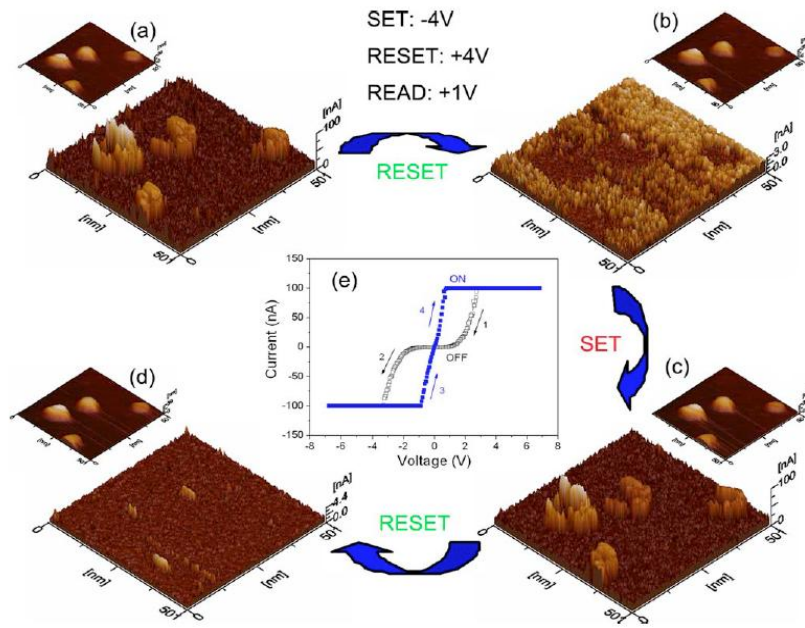


Fig. 1- 5 Evidences for the filament model by CAFM [9]

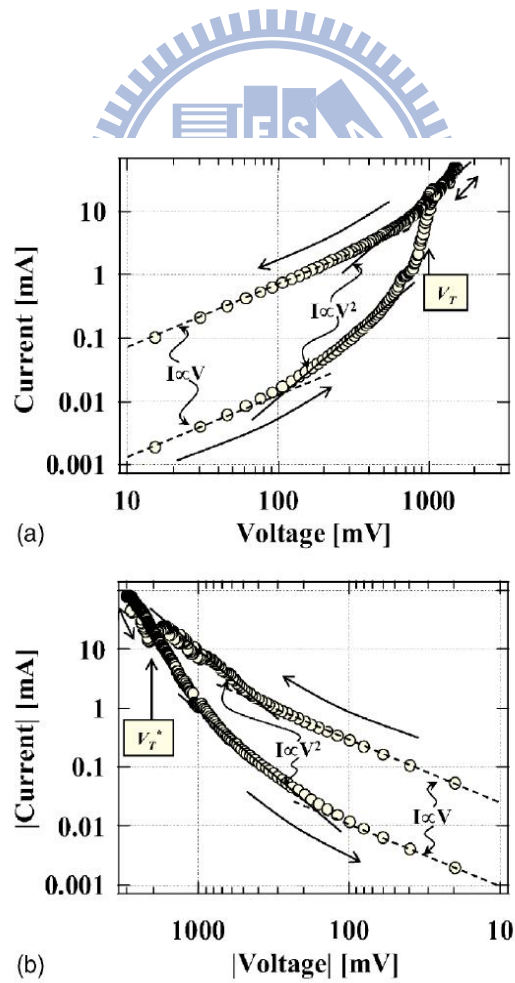


Fig. 1- 6 Schematic for charge trapping and detrapping I-V curve [9]

TECHNOLOGY AND DEVICE PERFORMANCE

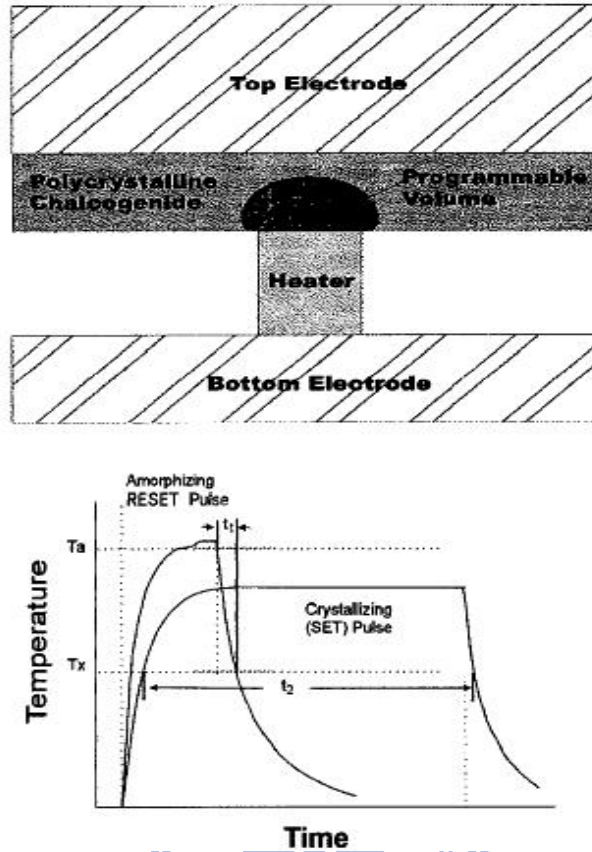


Fig. 1- 7 Schematic for phase change mechanism [13]

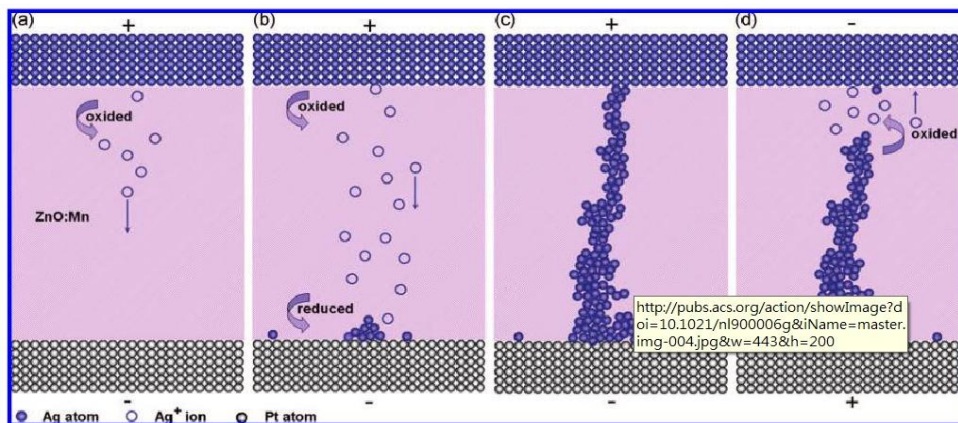


Fig. 1- 8 Schematic for electrochemical metallization mechanism [15]

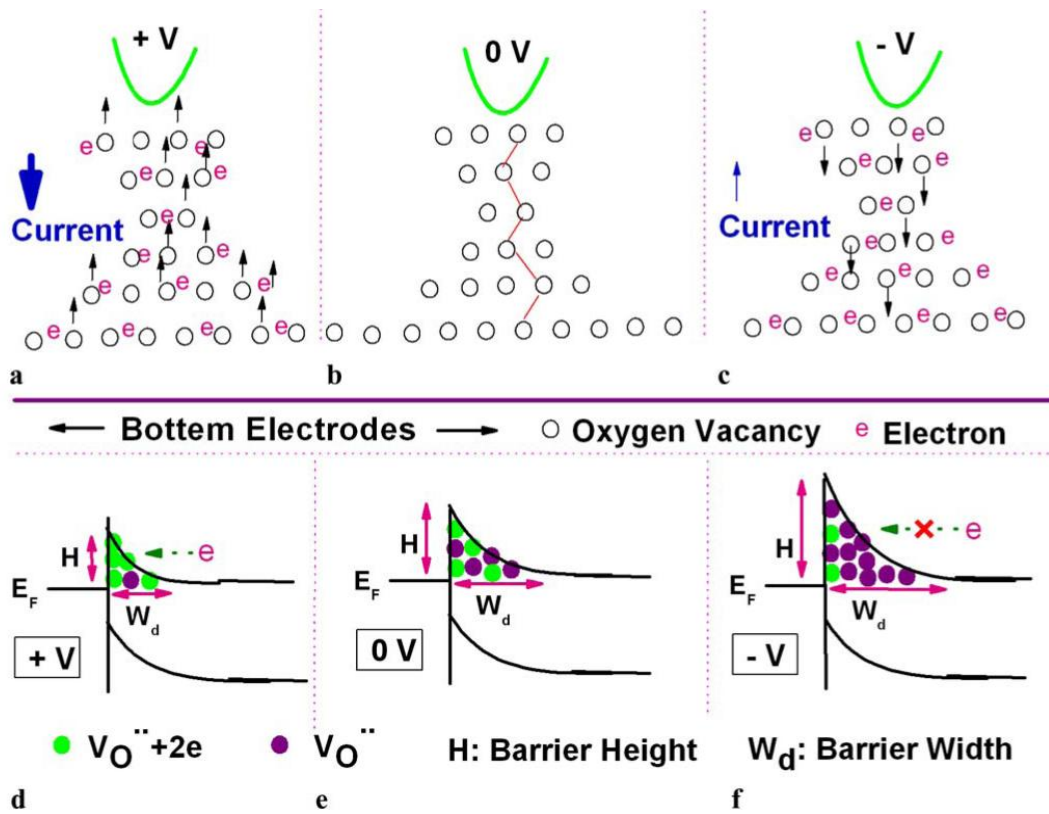


Fig. 1- 9 Schematic for Schottky barrier mechanism [17]



Chapter 2 Experimental Detail

2.1 DC magnetron sputtering system

Sputter system is widely used to deposit thin films for study because of its simple equipment structure, good uniformity for films, low cost, and capability for many kinds of films. There are some basic equipments for sputter structure including vacuum system, pressure monitor system, heating system, gas flow control system, and cooling system.

The magnetron sputtering system plot is shown in [Fig 2-1](#).

2.1.1 Vacuum System

Vacuum system includes two basic equipments, such as mechanical pump and cryogenics pump. Before the deposition, the pressure in the chamber has to be vacuumed down to 5×10^{-6} torr by two steps. The first step down to 5×10^{-2} torr is by the mechanical pump. Before the second step down to 5×10^{-6} torr, the mechanical pump is turn off, and then the cryogenics pump works for lowering pressure.

2.1.2 Pressure monitor system

Two gauges are used to detect the pressure in the chamber, basic pressure detect and the ion gauge.

2.1.3 Heating system

The heating system contains the quartz lamps and the thermal couples. The quartz lamp is used to increase the substrate temperature, and the thermal couple is used to calibrate the temperature.

2.1.4 Gas flow control system

The gas flow control system is used to control the ratio among different gas ingredients. In this thesis, only Ar is used in the film deposition. The Ar gas is used for plasma generation.

2.1.5 Cooling system

To avoid the thermal damage of the sputter system, cooling system is necessary. All the systems related to the sputter structure are constructed to provide cooling water to maintain the proper working temperature.

2.2 Pulse Laser Deposition (PLD) system

In comparison with other deposition techniques, including chemical vapor deposition (CVD), magnetron sputtering, spray phrolysis, PLD has many advantages:

1. Only a few parameters, such as laser energy density and pulse repetition rate, need to be controlled during the process.
2. The stoichiometry of the target can be retained in the deposited films.
3. The surface of the film is very smooth.
4. Good quality film can be deposited at room temperature due to the high kinetic energies (>1 eV) of atoms and ionized species in the laser-produced plasma.

In spite of many advantages of PLD, there are some disadvantages:

1. Splashing or the particulates deposition on the films.

2. The narrow angular distribution of the ablated species, which is generated by the adiabatic expansion of laser, produced plasma plume and the pitting on the target surface.

These features limit the usefulness of PLD in producing large area uniform thin films, and PLD has not been fully deployed in industry.

The PLD deposition system plot is shown in [Fig 2-2](#).

2.2.1 Mechanisms of PLD

The principle of pulsed laser deposition, in contrast to the simplicity of the system set-up, is a very complex physical phenomenon. It involves all the physical processes of laser-material interaction during the impact of the high-power pulsed radiation on a solid target. It also includes the formation of the plasma plume with high energetic species, the subsequent transfer of the ablated material through the plasma plume onto the heated substrate surface and the final film growth process. Thus PLD generally can be divided into the following four stages:

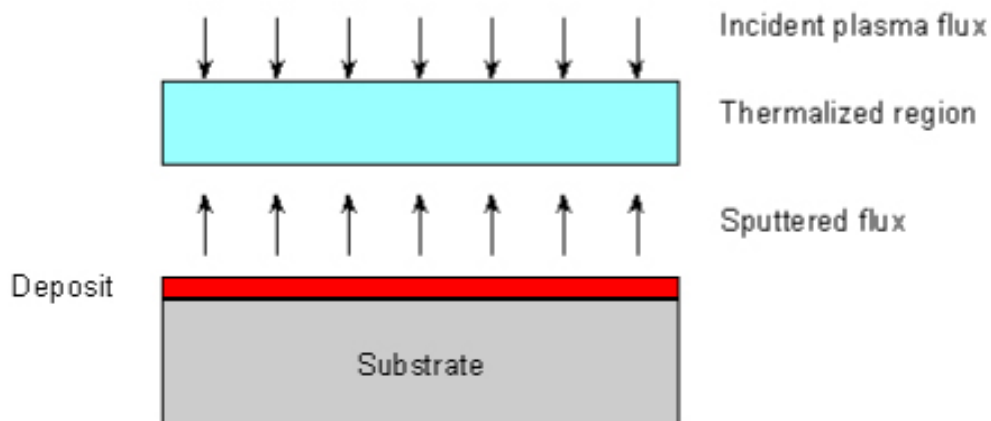
1. Laser radiation interaction with the target
2. Dynamic of the ablation materials
3. Decomposition of the ablation materials onto the substrate
4. Nucleation and growth of a thin film on the substrate surface

In the first stage, the laser beam is focused onto the surface of the target. At sufficiently high energy density and short pulse duration, all elements in the target surface are rapidly heated up to their evaporation temperature. Materials are dissociated from the target and ablated out

with stoichiometry as in the target. The instantaneous ablation rate is highly dependent on the fluences of the laser irradiating on the target. The ablation mechanisms involve many complex physical phenomena such as collisional, thermal and electronic excitation, exfoliation and hydrodynamics.

During the second stage the emitted materials tend to move towards the substrate according to the laws of gas-dynamic and show the forward peaking phenomenon [1]. R.K. Singh [2] reported that the spatial thickness varied as a function of $\cos^n \theta$, where $n \gg 1$. The laser spot size and the plasma temperature have significant effects on the deposited film uniformity. The target-to-substrate distance is another parameter that governs the angular spread of the ablated materials. Hanabusa [3] also found that a mask placed close to the substrate could reduce the spreading.

The third stage is important to determine the quality of thin film. The ejected high-energy species impinge onto the substrate surface and may induce various type of damage to the substrate. The mechanism of the interaction is illustrated in the following figure. These energetic species sputter some of the surface atoms and a collision region is established between the incident flow and the sputtered atoms. Film grows immediately after this thermalized region (collision region) is formed. The region serves as a source for condensation of particles. When the condensation rate is higher than the rate of particles supplied by the sputtering, thermal equilibrium condition can be reached quickly and film grows on the substrate surface at the expense of the direct flow of the ablation particles.



Schematic diagram of plasma-substrate interaction

Nucleation-and-growth of crystalline films depends on many factors such as the density, energy, degree of ionization, and the type of the condensing material, as well as the temperature and the physical-chemical properties of the substrate. The two main thermodynamic parameters for the growth mechanism are the substrate temperature T and the supersaturation Δm . They can be related by the following equation:

$$\Delta m = kT \ln(R / R_e)$$

where k is the Boltzmann constant, R is the actual deposition rate, and R_e is the equilibrium value at temperature T .

The nucleation process depends on the interfacial energies between the three phases present – substrate, the condensing material and the vapour. The minimum-energy shape of a nucleus is like a cap. The critical size of the nucleus depends on the driving force, i.e. the deposition rate and the substrate temperature. For the large nuclei, a characteristic of small supersaturation, they create isolate patches (islands) of the film on

the substrates, which subsequently grow and coalesce together. As the supersaturation increases, the critical nucleus shrinks until its height reaches an atomic diameter and its shape is that of a two-dimensional layer. For large supersaturation, the layer-by-layer nucleation will happen for incompletely wetted foreign substrates.

2.3 Fabrication of Resistive Switching Memory Device

The structures of the samples are based on ITO/LaAlO₃/ITO MIM devices, but a few differences would be made to do study, including Pd top electrode, and different oxygen process pressures. The fabrication processes would be stated respectively.

2.3.2 Bottom Electrode

We used the commercial ITO/glass as the bottom electrode and substrate. Before we deposited oxide thin film, the ITO/glass has to be clean by the standard cleaning process. The cleaning procedures were as follows:

1. ITO/glass substrate was washed in de-ionized (DI) water and oscillated in an ultrasonic bath for 10 minutes to remove particles
2. ITO/glass substrate was washed with acetone liquor and oscillated in an ultrasonic bath for 10 minutes to remove the organic residues.
3. Repeat step 1.
4. ITO/glass substrate was washed with isopropyl alcohol liquor and oscillated in an ultrasonic bath for 10 minutes.
5. ITO/glass substrate was backed in heater at 120⁰C for 15 minutes.

2.3.3 LAO

The LaAlO_3 was deposited by PLD as the resistive switching layer. First, we prepared PLD systems for 15 minutes. Lambda physics of excimer laser was furnished by $\lambda=248$ nm, pulse duration of 25 ns, repetition rate of 3 Hz, and the laser energy of 500 mJ. We used various oxygen pressures of 7×10^{-3} , 1.4×10^{-2} , and 2.8×10^{-2} torr to deposit LAO thin films with thickness of 45 nm.

2.3.4 Top Electrode

After the fabrication of the resistance switching layer, the top electrode was prepared to form the structure of metal/resistive switching layer/metal. We used DC sputter system to deposited ITO as the top electrode. To prevent the interfacial layer between the top electrode and the LAO thin film from sputtering damage, we deposited the ITO in two DC powers. We deposited the ITO at **5 W in 90 minutes**, and then at **10W in 70 minutes**. Therefore, the device with MIM structure was completed. The area of the top electrode was defined by the shadow mask with 0.02 cm^2 . The process flow of the MIM structure is shown in **Fig 2-3**.

2.4 Material Analysis

In this study, we used different equipments to analyze and measure including X-ray diffraction, X-ray photoelectron spectroscopy, atomic force microscopy, scanning electron microscopy, and transmission electron microscopy.

2.3.1 X-ray Diffraction

X-ray diffraction is a useful method to determinate the arrangement of atoms in target. The key step in x-ray crystallography is the diffraction of X-rays scattering from the material, and the scattered X-ray photons are measured in the diffraction measurement.

If the atoms are arranged in a periodic type, the diffracted waves will consist of sharp interference maxima with the same symmetry as in the distribution of atoms, and the peak is related to the atomic distance.

Thin film diffraction method is a very important process development.

2.3.2 X-ray Photoelectron Spectroscopy

When the light illuminates the matter, the inner electrons are going to be excited and ionized. The ionized electrons, which close to the surface of the matter have ability to escape into vacuum, named photoelectron, and the phenomenon is called photoelectric effect. Due to the different components and chemical states of the mater, photoelectrons have characteristic kinetic energy, which can be used to identify the composed elements and the chemical states of surface atoms. Then the excitation source is soft x-ray, the photoemission spectroscopy is termed by X-ray photoelectron spectroscopy, which is core level excitation.

2.3.3 Atomic Force Microscopy

Atomic force microscopy is a useful method to detect the surface morphology of the thin film. The average roughness and the root mean

square roughness are automatically recorded and calculated by the software. The schematic diagram of the AFM is shown in [Fig 2-4](#).

2.3.4 Scanning Electron Microscopy

Scanning electron microscopy is a useful method to see the surface morphology and the cross section image of the structure. The accelerated electron beam emitted from the cold-cathode electron gun collides with the target, and the secondary electrons from the surface of the target are detected and rendered into a bright SEM image. The schematic diagram of the SEM system is shown in [Fig 2-5](#).

2.3.5 Focus ion beam (FIB)

FIB is used to shape the sample to meet the request of the TEM measurement. The system is different from the SEM system, because FIB systems use a finely focused beam of ions (usually gallium) rather than the beam of electrons.

The gallium (Ga^+) primary ion beam hits the sample surface and sputters a small amount of the material, which leaves the surface as either secondary ions (i^+ or i^-) or neutral atoms (n^0). The primary beam also produces secondary electrons (e^-). As the primary beam raster on the sample surface, the signal from the sputtered ions or secondary electrons is collected to form an image.

2.3.6 Transmission Electron Microscopy (TEM)

TEM is a useful measurement to investigate the local region of the device. Accelerated electrons are transmitted and focused on the device

by the condenser lenses. It is necessary for the device to be very thinner, so the electrons can be transparent through the device. The transmitted and forward scattered electrons form a diffraction pattern in the back focus plane and a magnified bright image in the main screen.

2.5 Electrical Analysis

The electrical analysis is measured by Agilent 4156C system controlled by a desktop computer with the Agilent VEE software. During the electrical analyses, the voltage is applied on the top electrode, and then we record the I-V data. We also use the equipment to measure the data retention time and endurance.

2.4.1 Current-Voltage Measurement

The I-V characteristics of the different conditions are performed by Agilent 4156C. Conducting current is detected by applying a sweep voltage in specific range. The conducting mechanisms are different from various materials. From the I-V curve, we can judge the conducting mechanisms, and the on state with the low resistance or off state with the high resistance can be observed easily.

2.4.2 Data Retention Time Measurement

Data retention is an important performance for nonvolatile memory. It is a period of time for the stored information that can be kept without the power supply. For an ideal memory, data retention time is requested to 10 years. The data retention time is measured at room temperature or

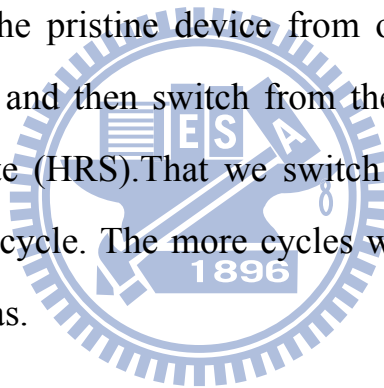
higher temperature for thermal acceleration test.

First, we switch the device to specific state, and then small voltage is applied to read the current to calculate the resistance after a specific period. The more time the data stored in the better data retention the device has.

2.4.3 Endurance Measurement

Endurance is an important performance for the memory. The good endurance performance means that the memory can be program and erase for many times.

First, we switch the pristine device from original state to the low resistance state (LRS), and then switch from the low resistance state to the high resistance state (HRS). That we switch from HRS to LRS and then LRS to HRS is 1 cycle. The more cycles we can operate the better endurance the device has.



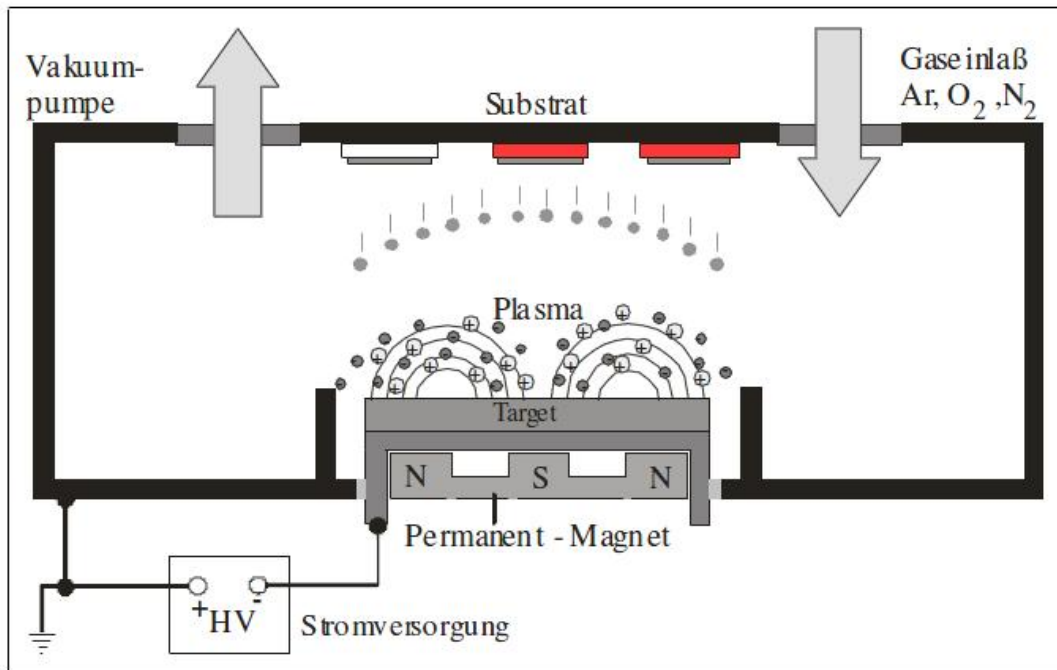


Fig. 2- 1 Magnetron sputtering system

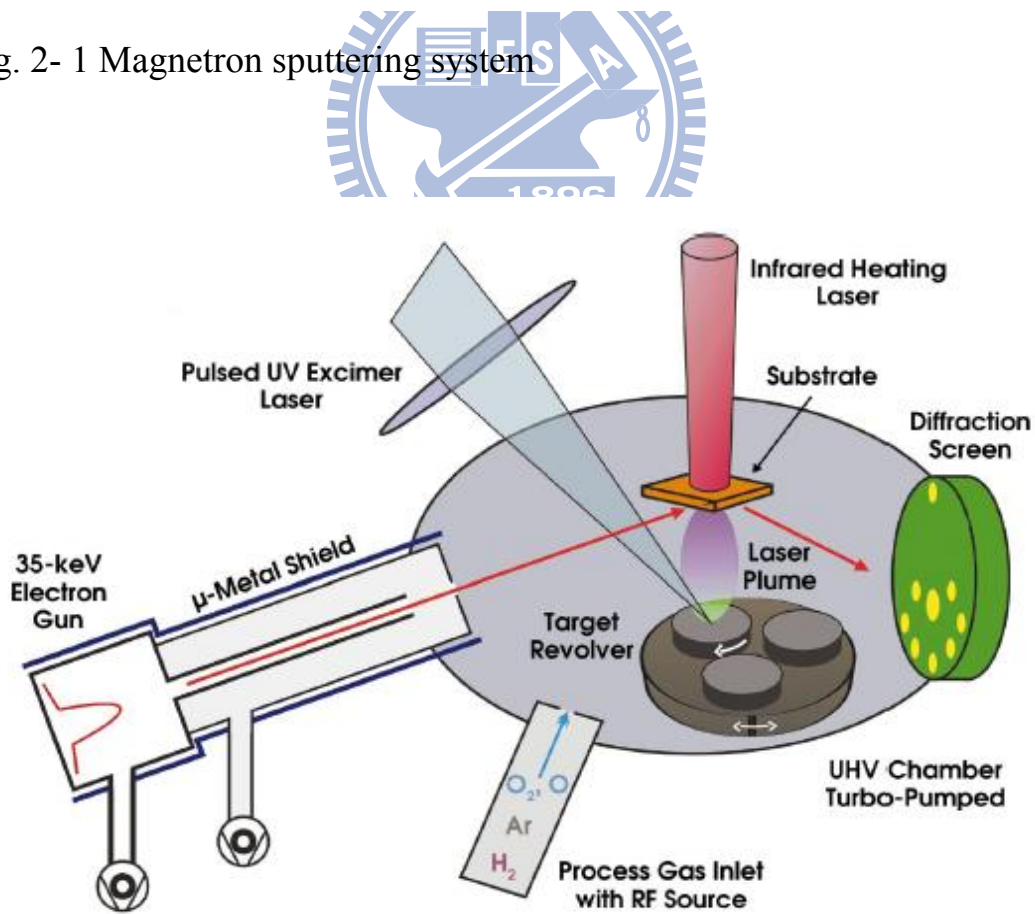


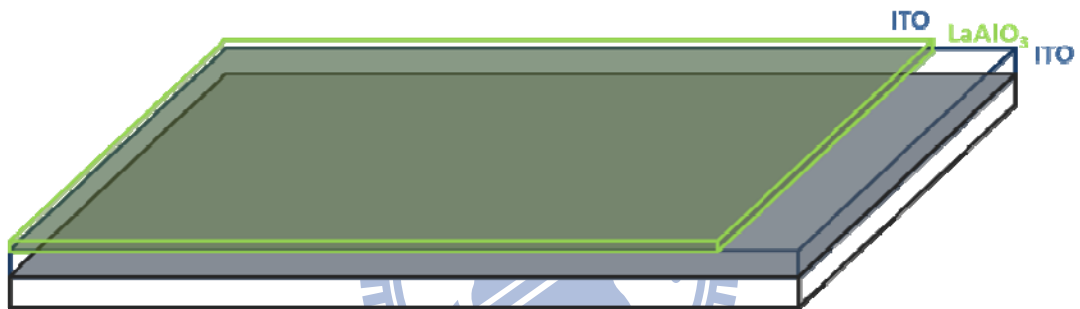
Fig. 2- 2 PLD deposition system

Step1:



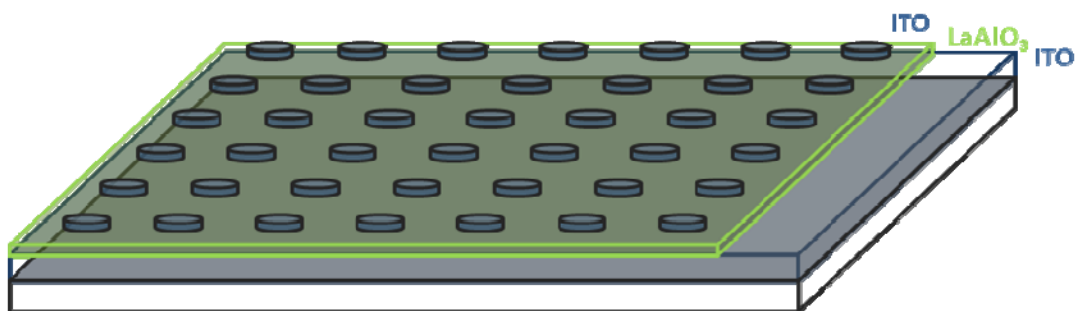
Commercial glass substrate and ITO electrode initial

Step2:



LaAlO₃ deposited by pulsed laser deposition

Step3:



ITO electrode deposited by DC sputter.

Fig. 2- 3 Process flow of the MIM structure

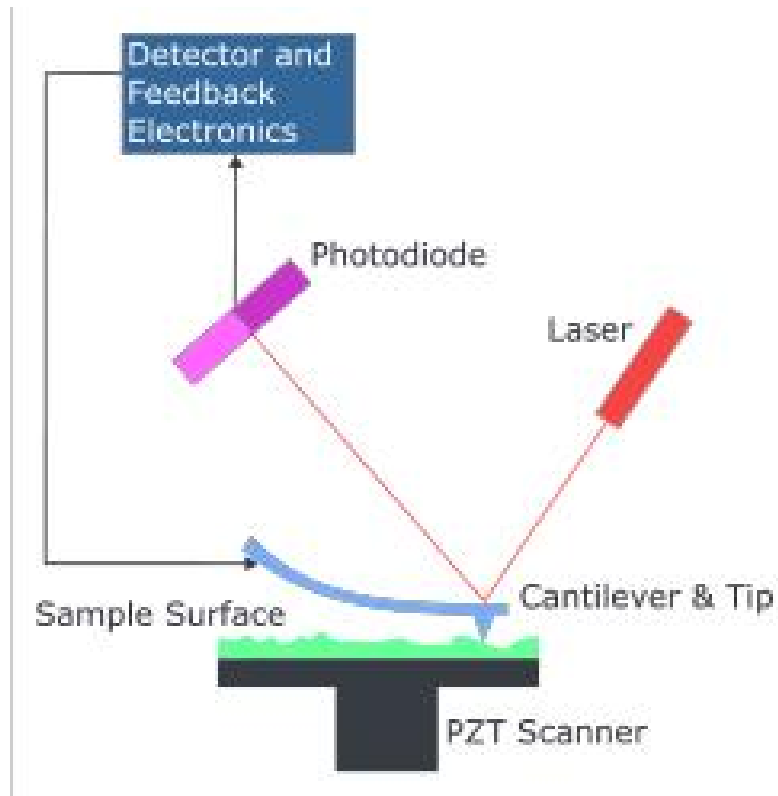


Fig. 2- 4 Atomic Force Microscopy

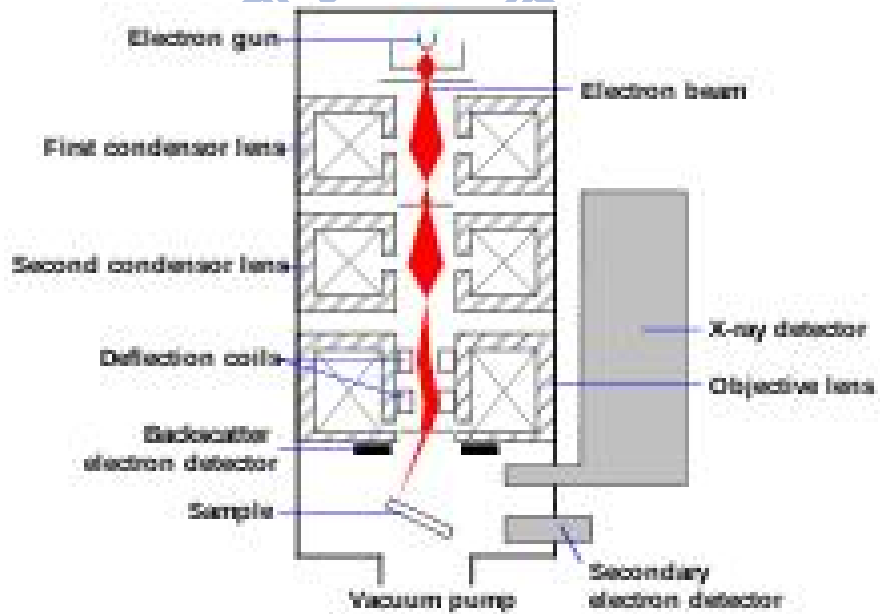
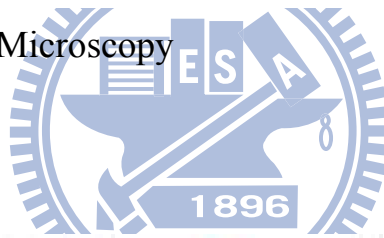


Fig. 2- 5 Scanning electron microscopy system

Chapter 3

Result and Discussion of Investigation of LaAlO₃ thin film with various oxygen pressures

3.1 Introduction

Among the many potential high-k materials, LaAlO₃ has recently attracted much attention because of its many advantages included its higher K, lack of reactivity with Si, larger band offsets with Si. It is known that oxide film deposited by the pulsed laser deposition (PLD) often has oxygen vacancies which play an important role in the electrical performance of the film [20][21]. According to the paper [22][23][24], oxygen vacancies play an important role in the leakage current.

3.2 Electrical characterization

The electrical properties of the LaAlO films were investigated by current-voltage (I-V) of the ITO/LAO/ITO metal-insulation-oxide metal (MIM) capacitor structures.

Electrical properties of LAO films were deposited in different oxygen pressure and characterized by leakage current measurements, Agilent 4156C system. The ITO/LAO/ITO structures were deposited on the commercial glass with different oxygen pressure of 7×10^{-3} , 1.4×10^{-2} and 2.8×10^{-2} torr, respectively. We used MIM structure to test leakage current.

Fig 3-1 shows the leakage current density of the LAO MIM sample at 1MV/cm. As show in **Fig 3-1**, the leakage current density of LAO thin films decreases with the decreasing of the oxygen pressure. Based on the structure analysis of the films mentioned herein, it could be concluded that the leakage current decreased because of the reduction of the oxygen vacancies [].

Fig 3-1 shows that the different polarity of the E-Field exhibits different magnitude leakage current. **Fig 3-2, Fig 3-3 and Fig 3-4** show the Ohmic conduction fitting of the samples with various oxygen pressures of 7×10^{-3} , 1.4×10^{-2} and 2.8×10^{-2} torr. **Fig 3-5, Fig 3-6 and Fig 3-7** show the Schottky conduction fitting of the samples with various oxygen pressures of 7×10^{-3} , 1.4×10^{-2} and 2.8×10^{-2} torr. **Fig 3-8** shows the breakdown negative voltages with various oxygen pressures. It shows that the sample with larger oxygen pressure stand larger voltage to breakdown. **Fig 3-9** shows the breakdown positive voltage with various oxygen pressures. It also shows that the sample with larger oxygen pressure stand larger voltage to breakdown.

Fig 3-10, Fig 3-11 and Fig 3-12 show that the breakdown voltages of the samples with oxygen pressure in various temperatures. We can find out that the sample with larger phenomenon temperature exhibits lower breakdown voltage. **Fig 3-13, Fig 3-14 and Fig 3-15** show that the power to breakdown voltage of the samples in various temperatures. When the temperature is increased, the power to breakdown decreases. This is result from the extra power supplied from the phenomenon.

3.3 Physical Characterization

3.3.1 Atomic force microscope (AFM) and surface roughness analysis

Table 3-1 shows the comparison of the surface roughness of the LAO thin films with different oxygen pressure. Fig 3-16, Fig 3-17, and Fig 3-18 show that AFM plot with various oxygen pressure. This may be related to the quality of PLD thin film deposition effects [25] [26].

3.3.2 Scanning Electron Microscopy (SEM) analysis

Fig 3-19, Fig 3-20, and Fig 3-21 show that the surface SEM of the three samples.

3.3.3 X-ray diffraction (XRD) analysis

Fig 3-22 shows the X-ray diffraction (XRD) analysis of the LAO thin films with different oxygen pressure.

3.3.4 X-ray photoelectron spectroscopy (XPS) analysis

Fig 3-23, Fig 3-24 and Fig 3-25 show that La 3d, Al 2p and O 1s portions of the XPS spectra of LAO thin films. The plots show that the binding energy increases with increasing of the oxygen pressure. However, the low oxygen pressure is favorable to produce large amount of oxygen vacancies [27], and large amount of vacancies result in high leakage current. This is a reliability issue to be concern.

3.3.5 Transmission Electron Microscopy (TEM) analysis

Fig 3-26, Fig 3-27 and Fig 3-28 show that the TEM analysis of the three samples. The sample with oxygen pressure of 2.8×10^{-2} torr shows crystallization in the oxide layer, and the sample with oxygen pressure of

7×10^{-3} torr shows amorphous oxide layer.

Table 3- 1

PO_2	7×10^{-3} torr	1.4×10^{-2} torr	2.8×10^{-2} torr
Roughness	1.741nm	1.729nm	1.527nm

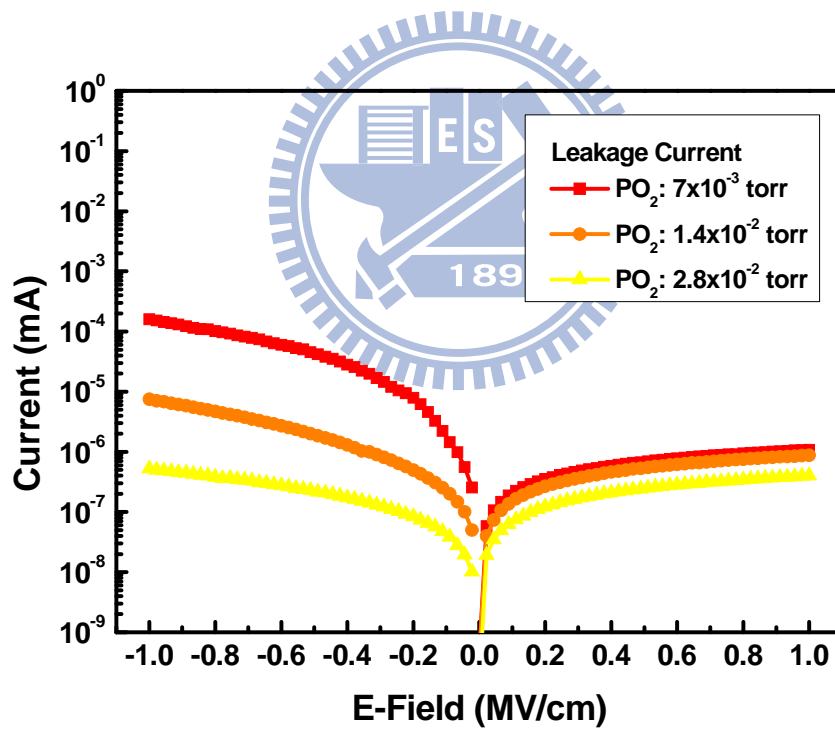


Fig. 3- 1 Leakage current of LAO films deposited under various oxygen pressures

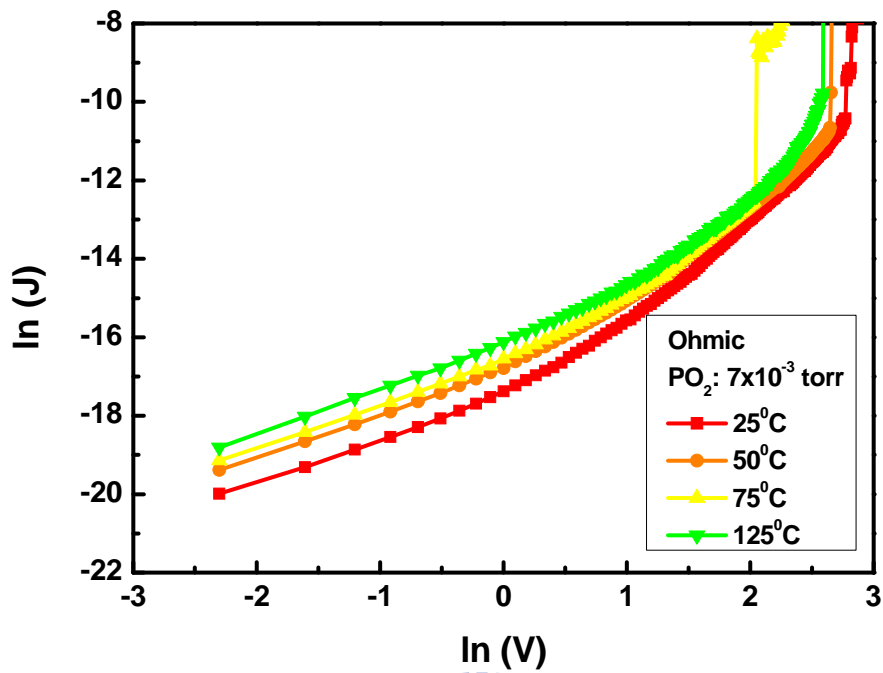


Fig. 3- 2 Ohmic conduction fitting of the sample in oxygen pressure of the 7×10^{-3} torr

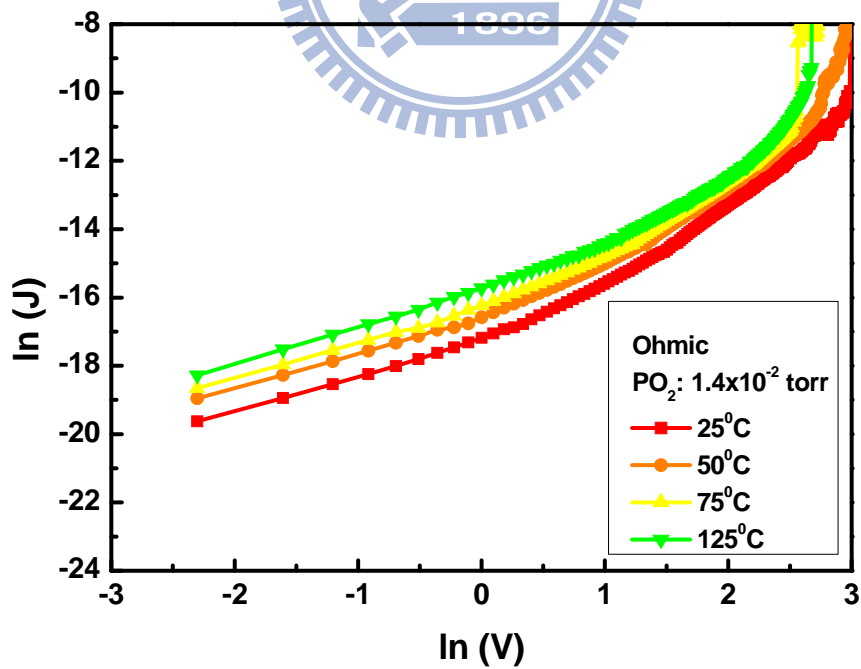


Fig. 3- 3 Ohmic conduction fitting of the sample in oxygen pressure of the 1.4×10^{-2} torr

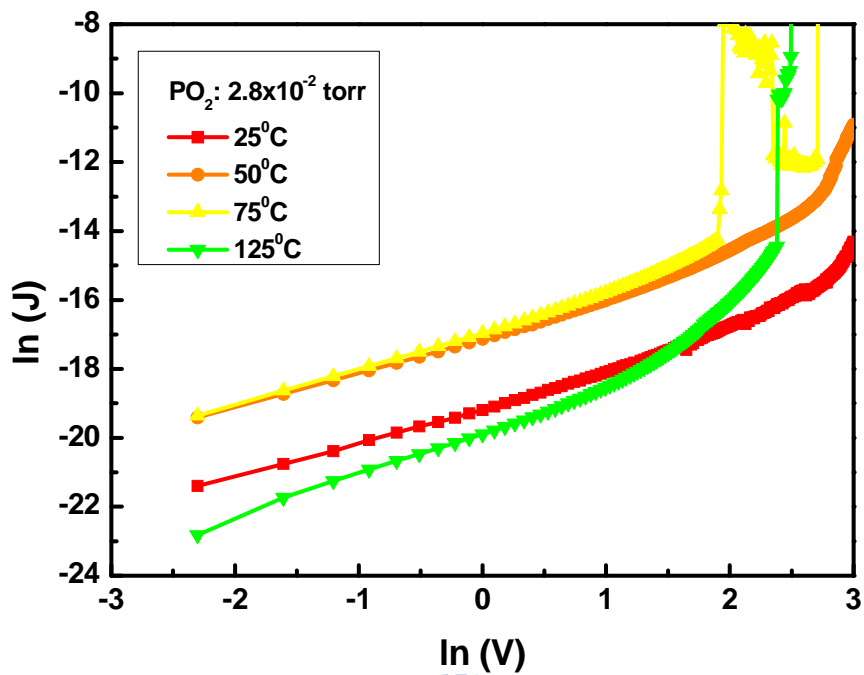


Fig. 3- 4 Ohmic conduction fitting of the sample in oxygen pressure of the 2.8×10^{-2} torr

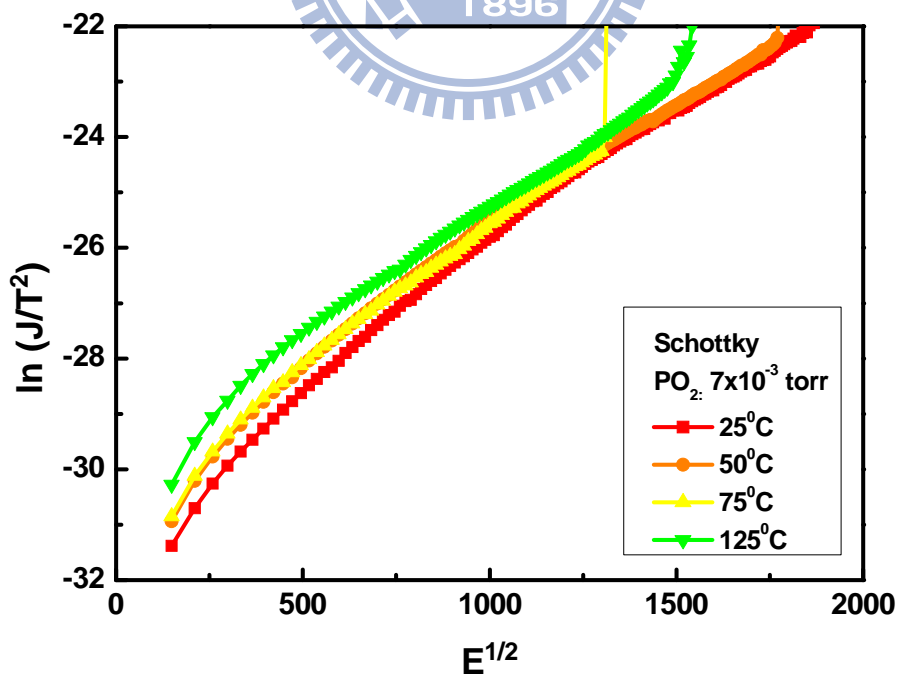


Fig. 3- 5 Schottky conduction fitting of the sample in oxygen pressure of the 7×10^{-3} torr

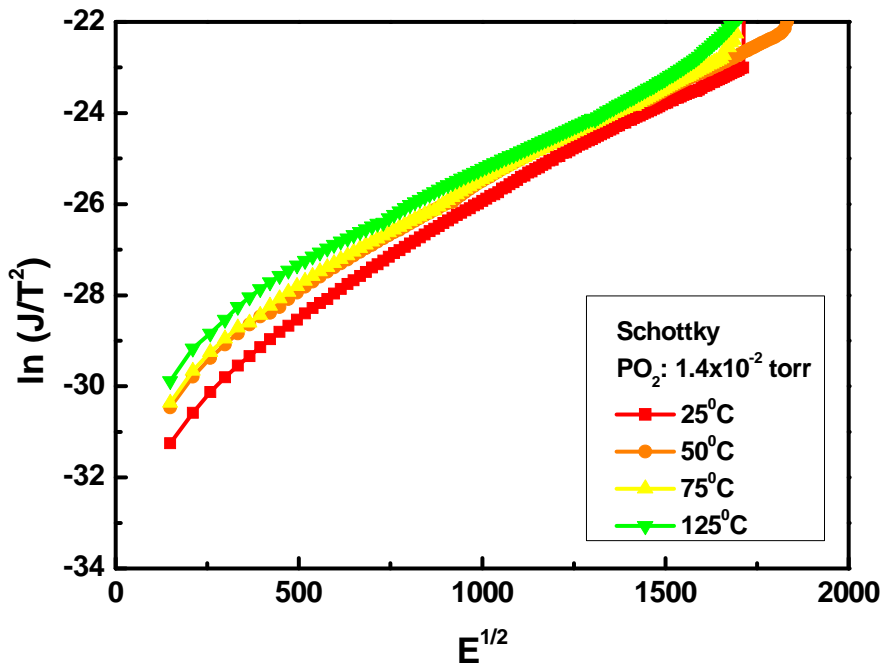


Fig. 3- 6 Schottky conduction fitting of the sample in oxygen pressure of the 1.4×10^{-2} torr

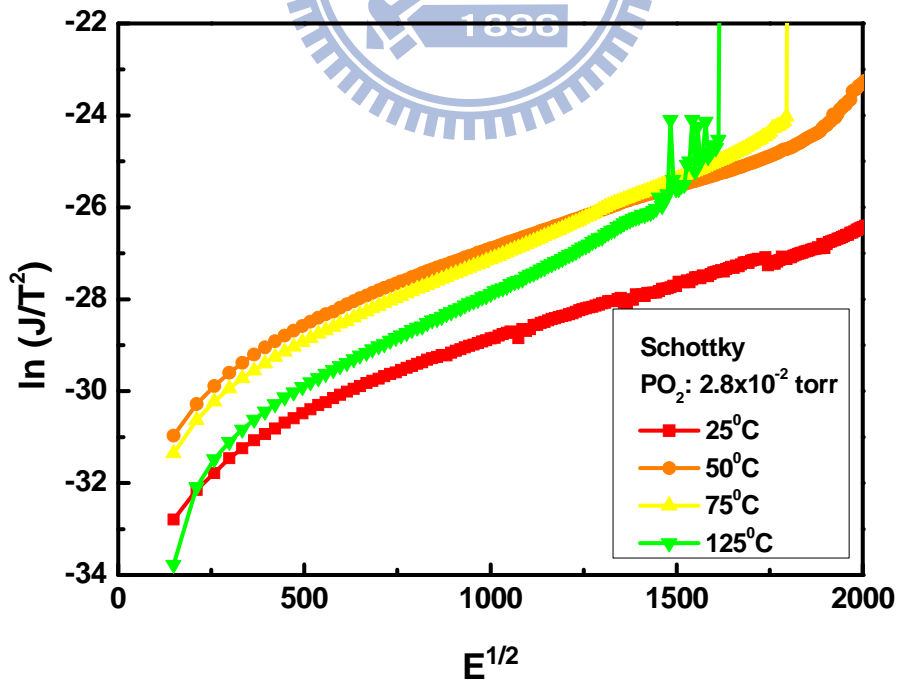


Fig. 3- 7 Schottky conduction fitting of the sample in oxygen pressure of the 2.8×10^{-2} torr

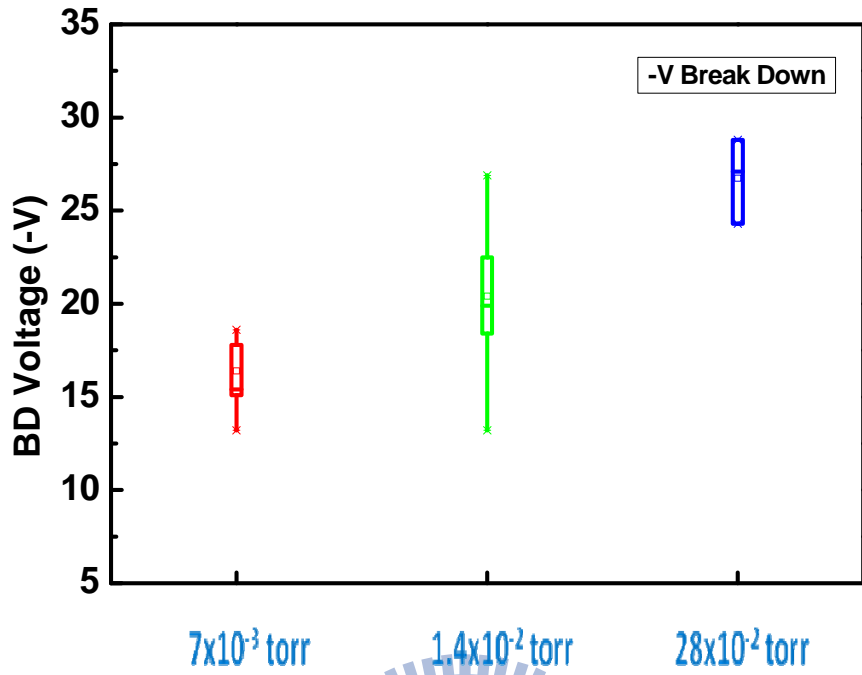


Fig. 3- 8 Breakdown negative voltage with three samples with various oxygen pressures

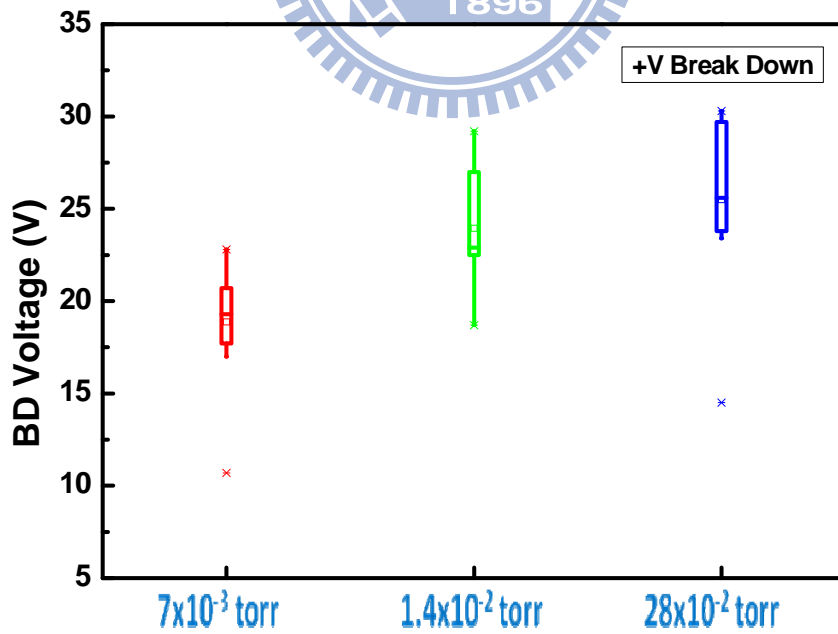


Fig. 3- 9 Breakdown positive voltage with three samples with various oxygen pressures

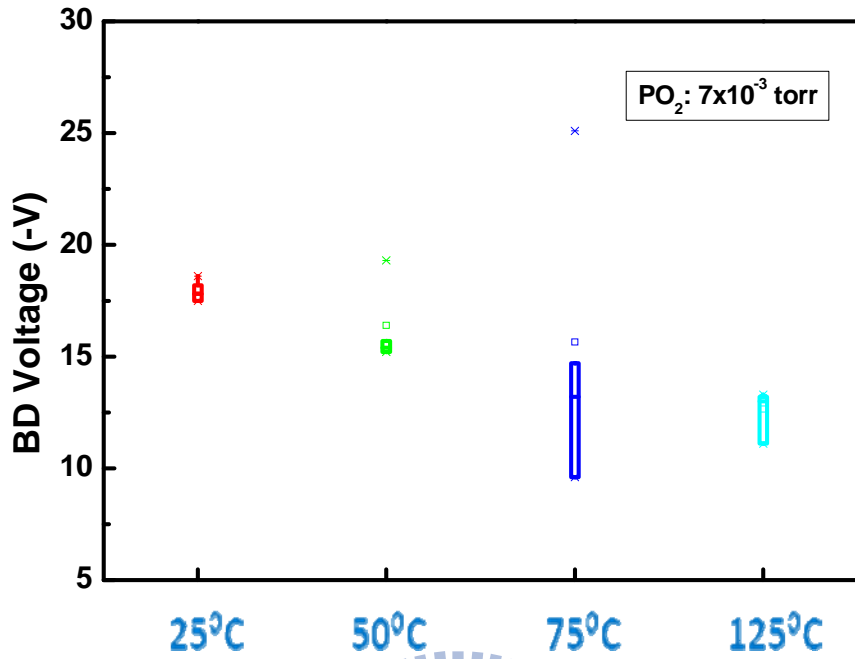


Fig. 3- 10 Breakdown voltage of the sample with oxygen pressure of 7×10^{-3} torr in various temperatures

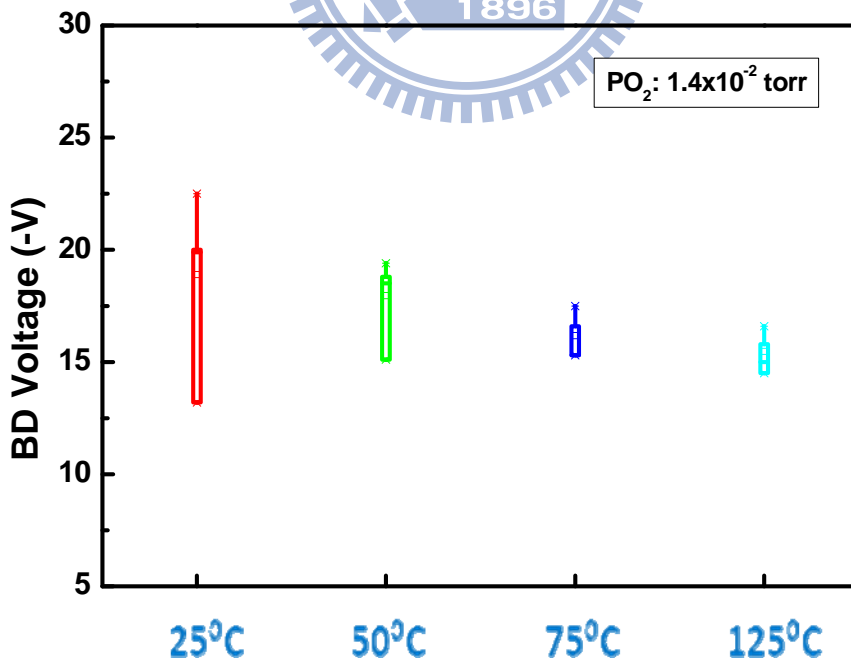


Fig. 3- 11 Breakdown voltage of the sample with oxygen pressure of 1.4×10^{-2} torr in various temperatures

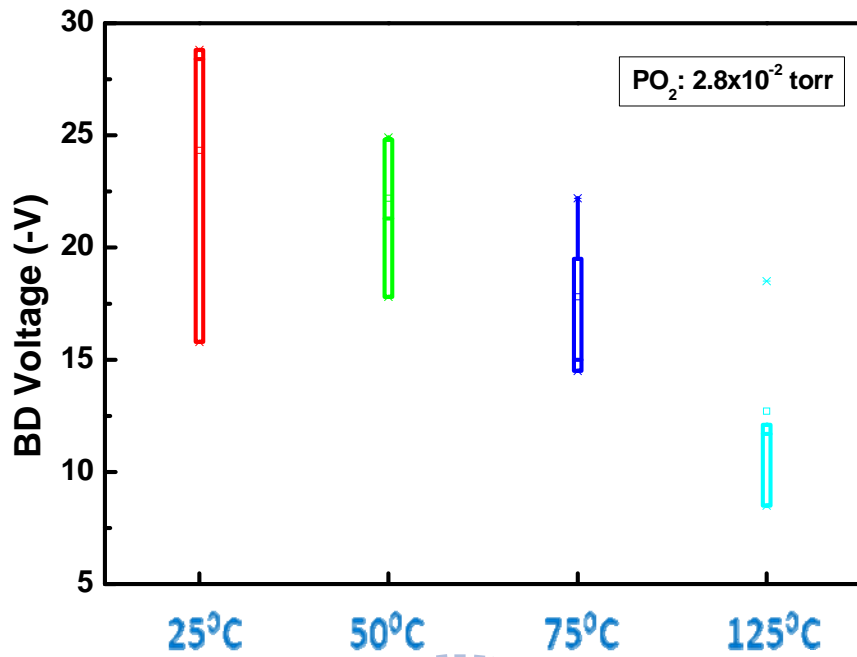


Fig. 3- 12 Breakdown voltage of the sample with oxygen pressure of 2.8×10^{-2} torr in various temperature

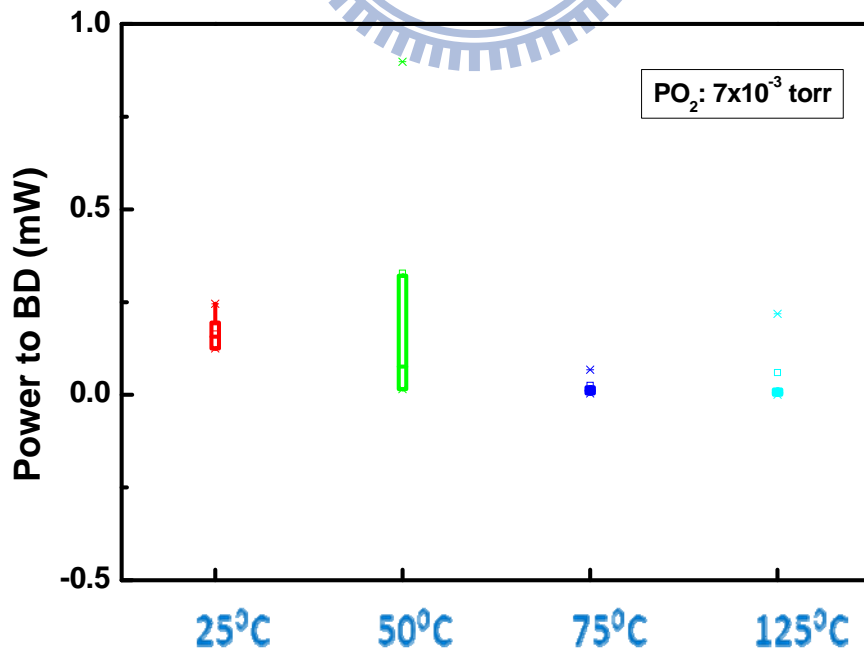


Fig. 3- 13 Power to breakdown voltage of the sample with oxygen

pressure of 7×10^{-3} torr in various temperatures

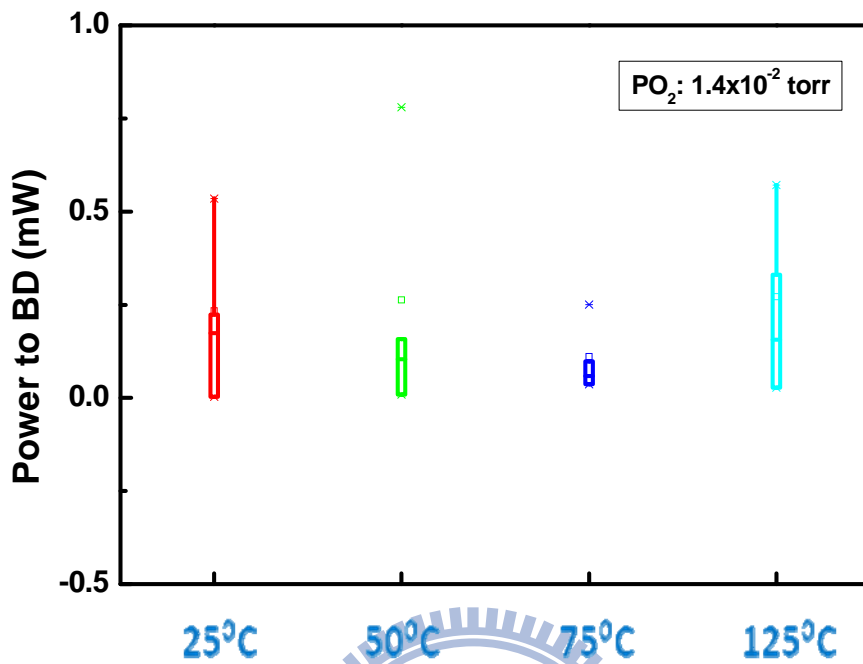


Fig. 3- 14 Power to breakdown voltage of the sample with oxygen pressure of 1.4×10^{-2} torr in various temperatures

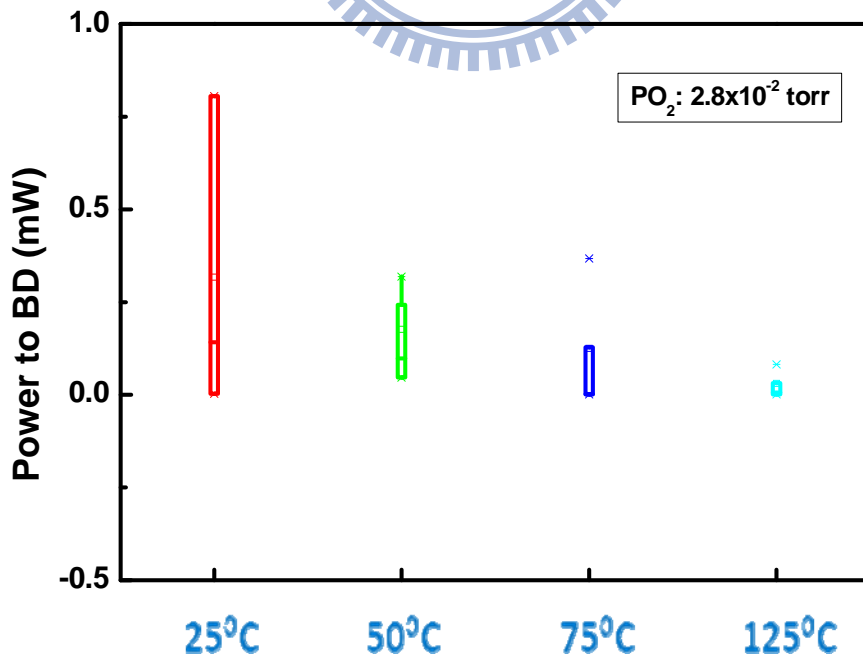


Fig. 3- 15 Power to breakdown voltage of the sample with oxygen

pressure of 2.8×10^{-2} torr in various temperatures

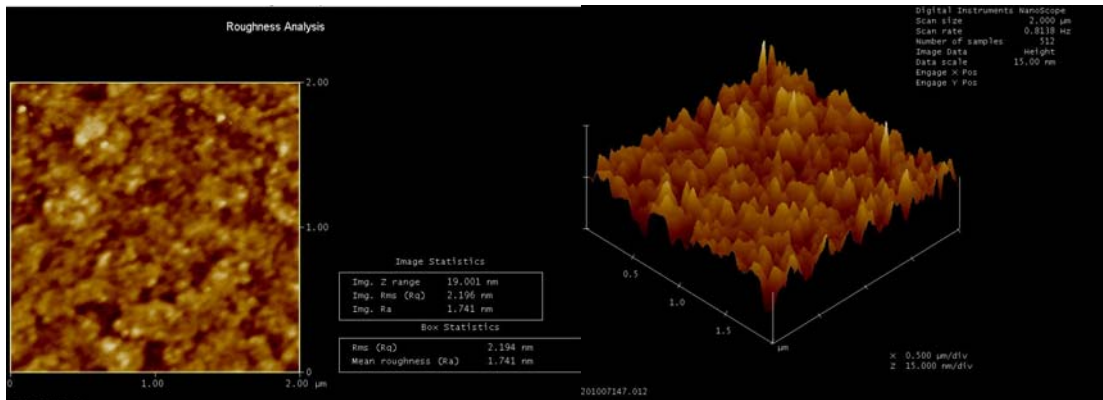


Fig. 3- 16 AFM of the sample with oxygen pressure of 7×10^{-3} torr

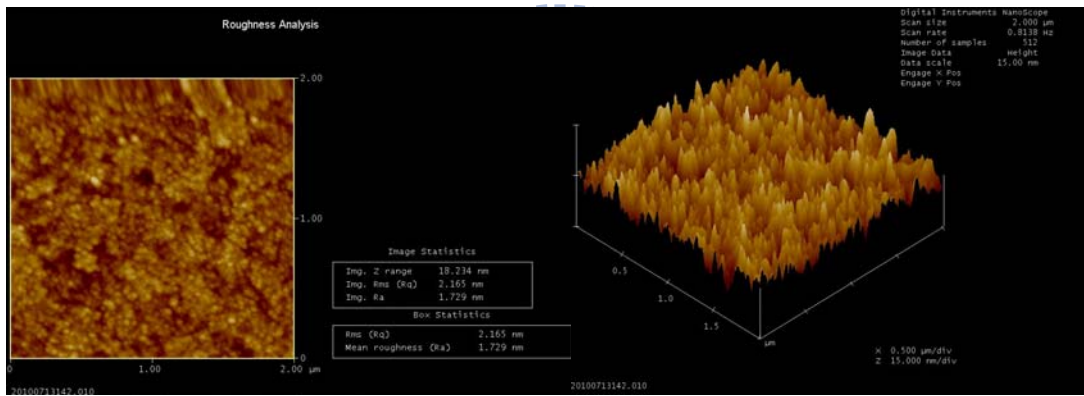


Fig. 3- 17 AFM of the sample with oxygen pressure of 1.4×10^{-2} torr

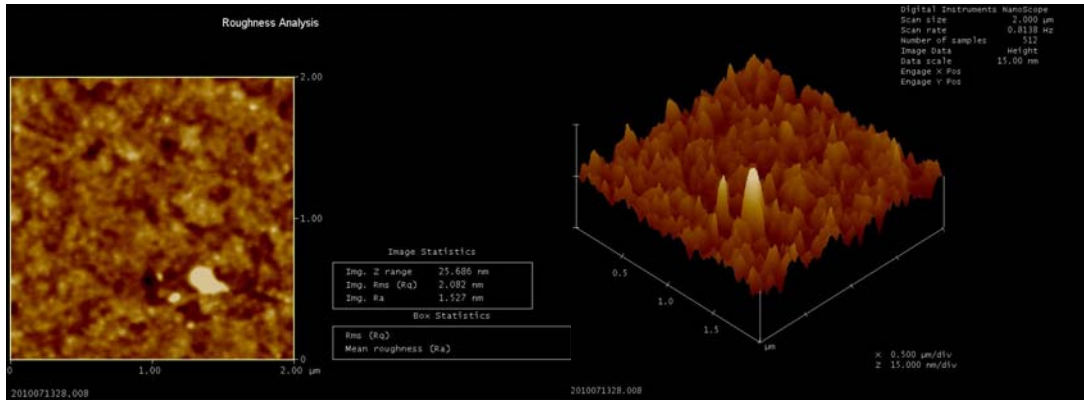


Fig. 3- 18 AFM of the sample with oxygen pressure of 2.8×10^{-2} torr

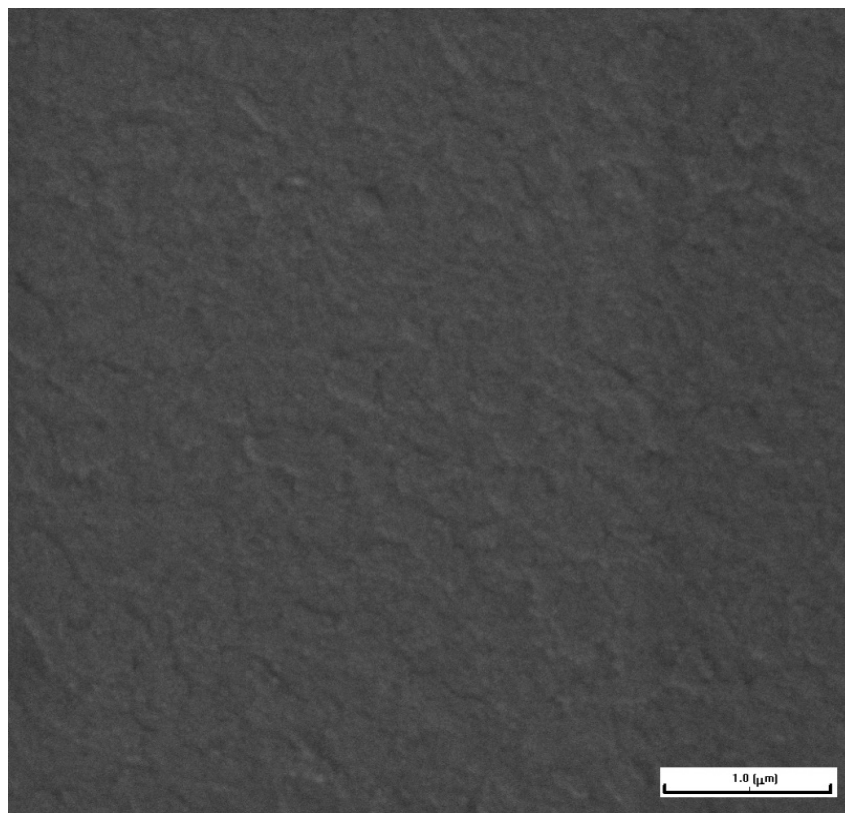


Fig. 3- 19 SEM of the sample with oxygen pressure of 7×10^{-3} torr

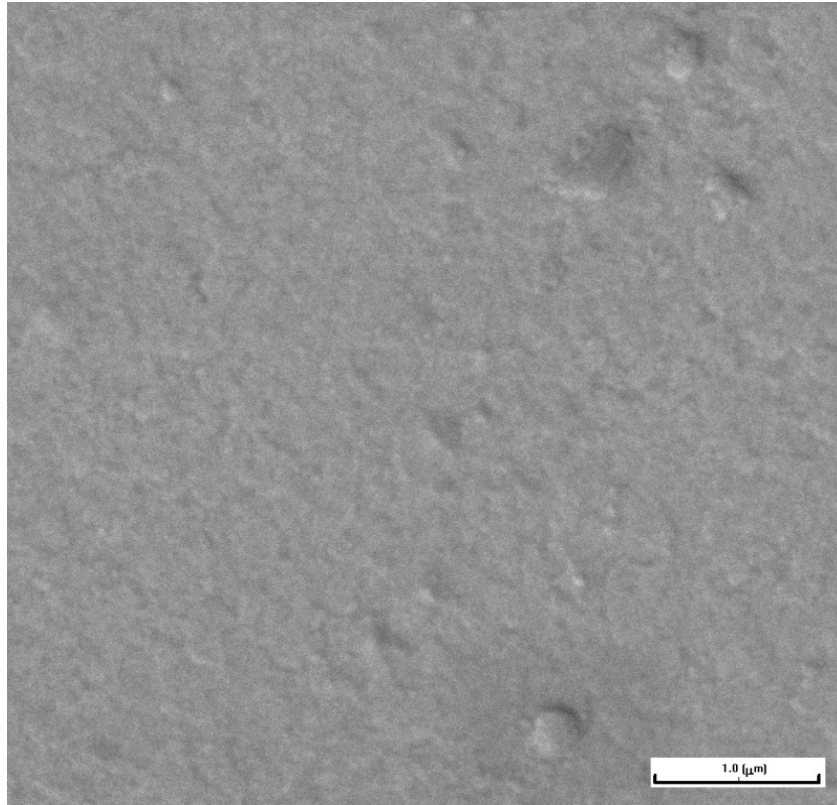


Fig. 3- 20 SEM of the sample with oxygen pressure of 1.4×10^{-2} torr

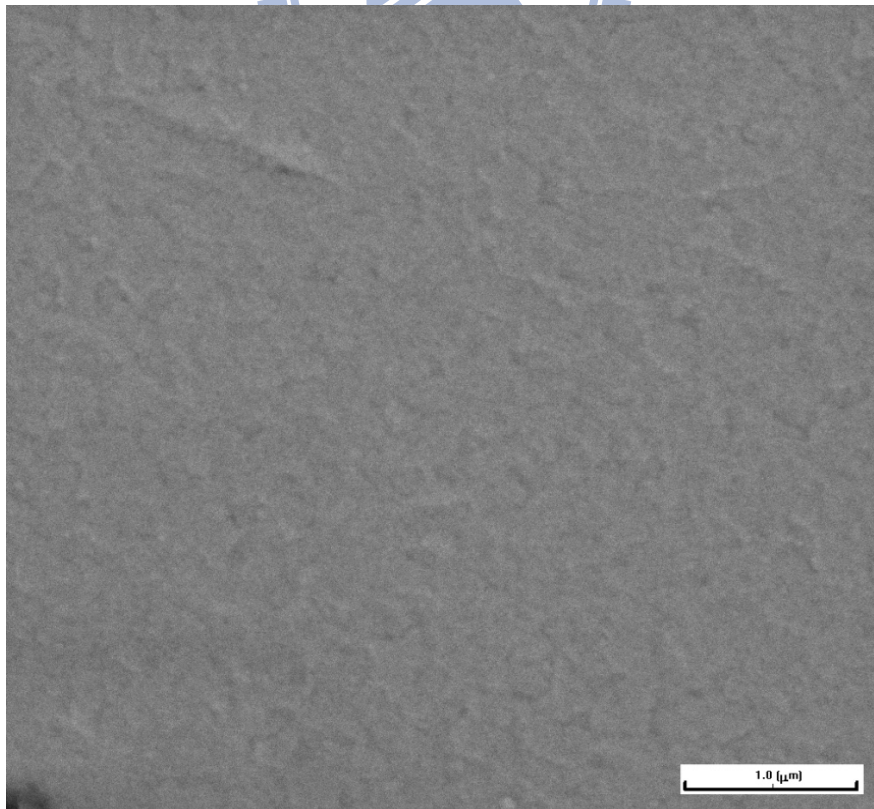


Fig. 3- 21 SEM of the sample with oxygen pressure of 2.8×10^{-2} torr

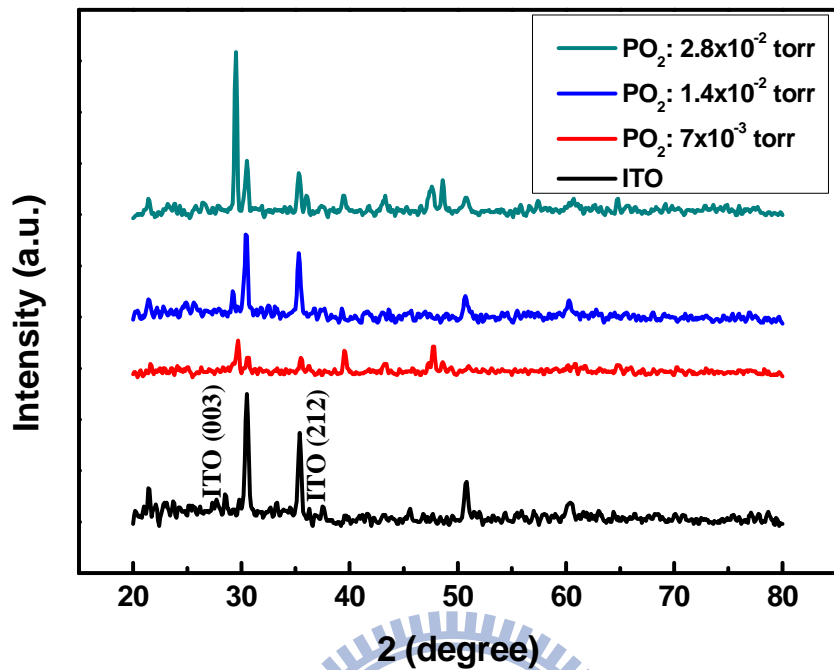


Fig. 3- 22 XRD of the samples with different oxygen pressure

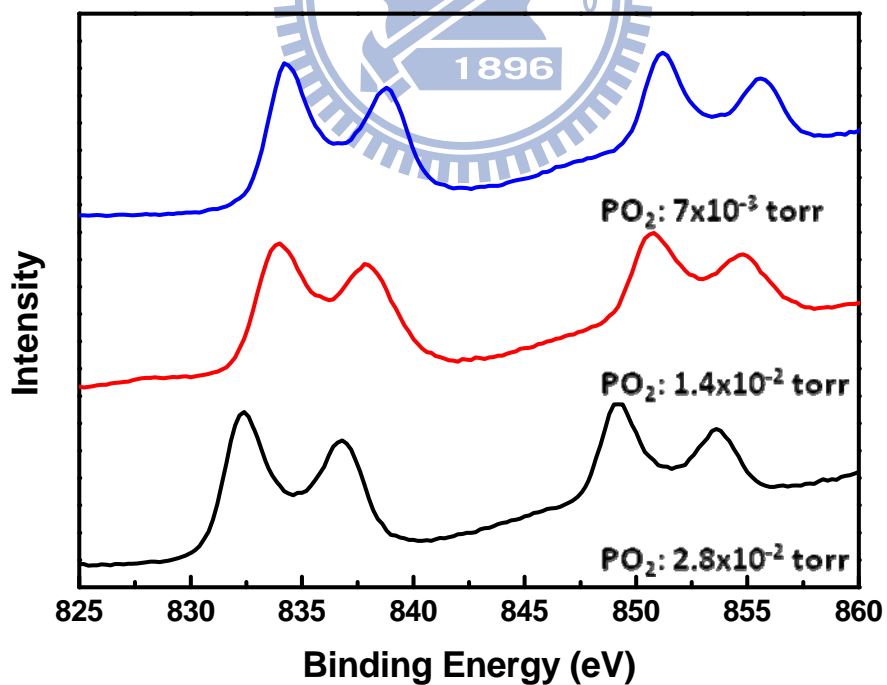


Fig. 3- 23 XPS result of La 3d peak with different oxygen pressure

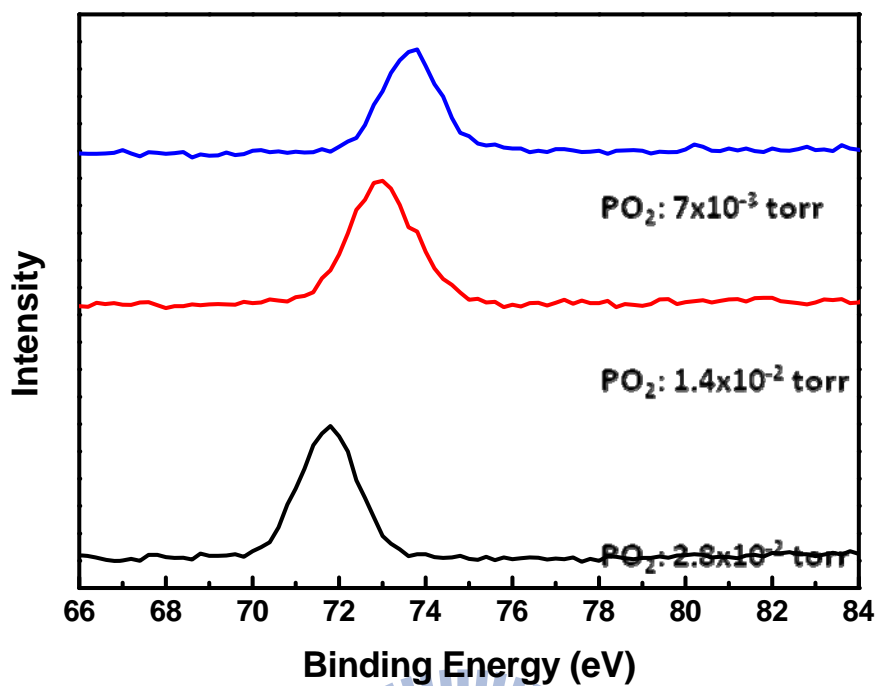


Fig. 3- 24 XPS result of Al 2p peak with different oxygen pressure

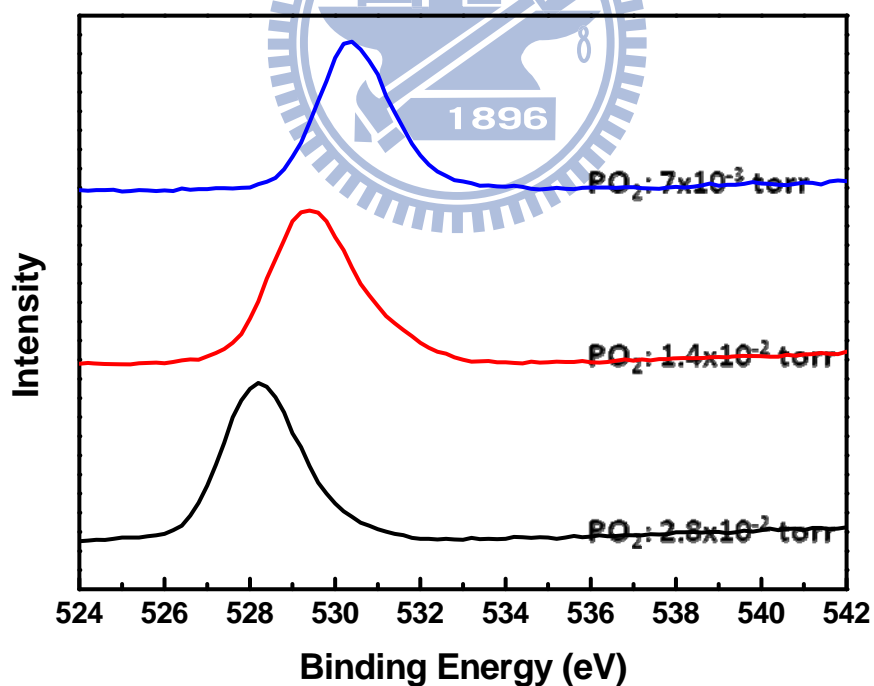


Fig. 3- 25 XPS result of O 1s peak with different oxygen pressure

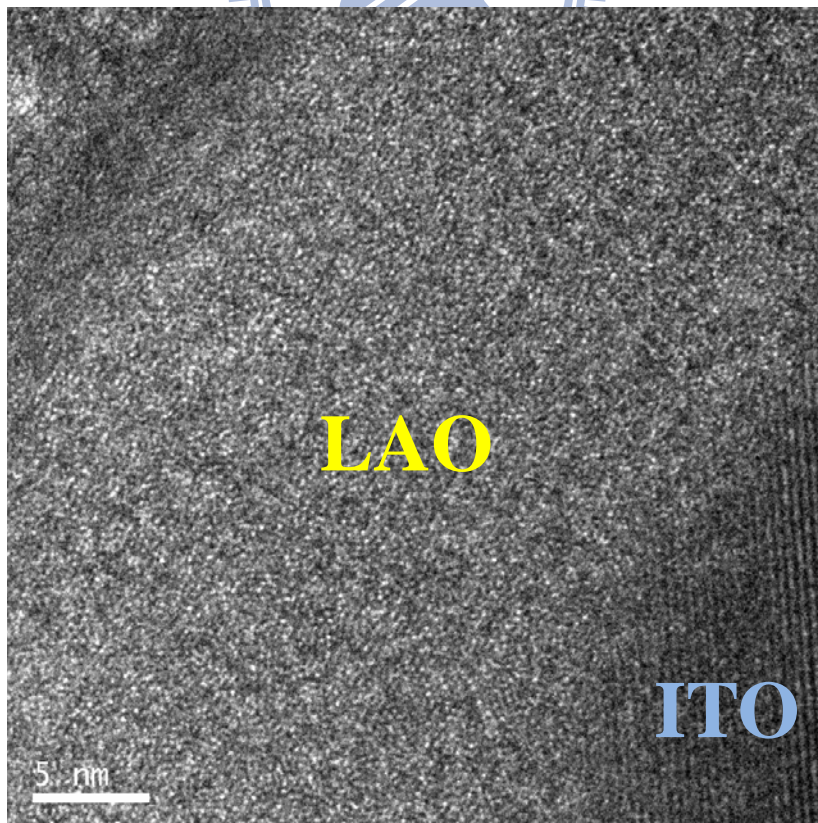
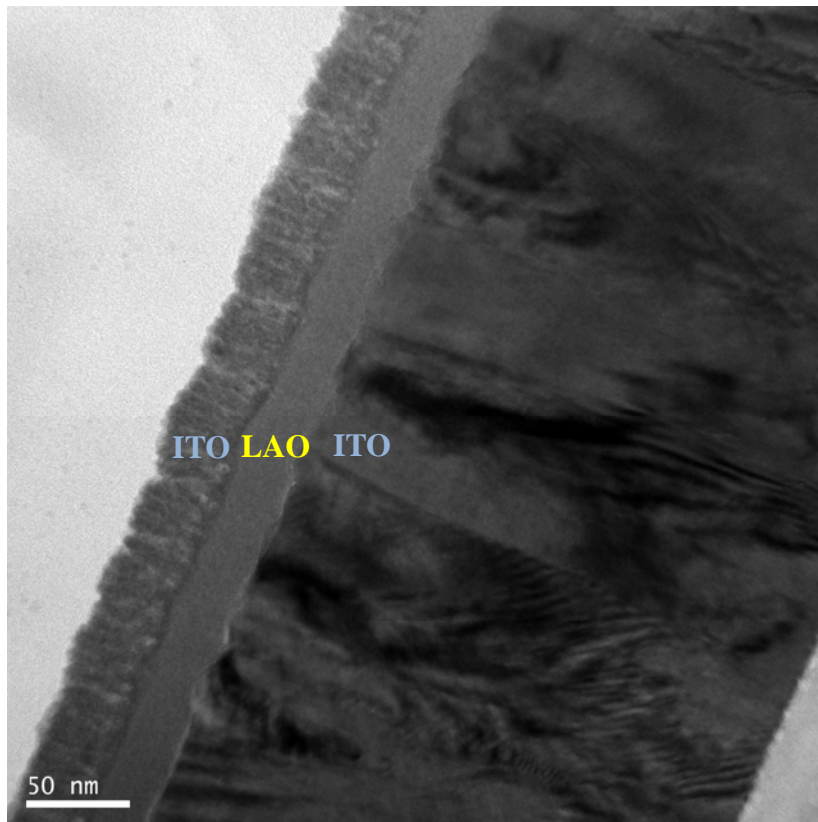


Fig. 3- 26 TEM of the sample with oxygen pressure of 7×10^{-3} torr

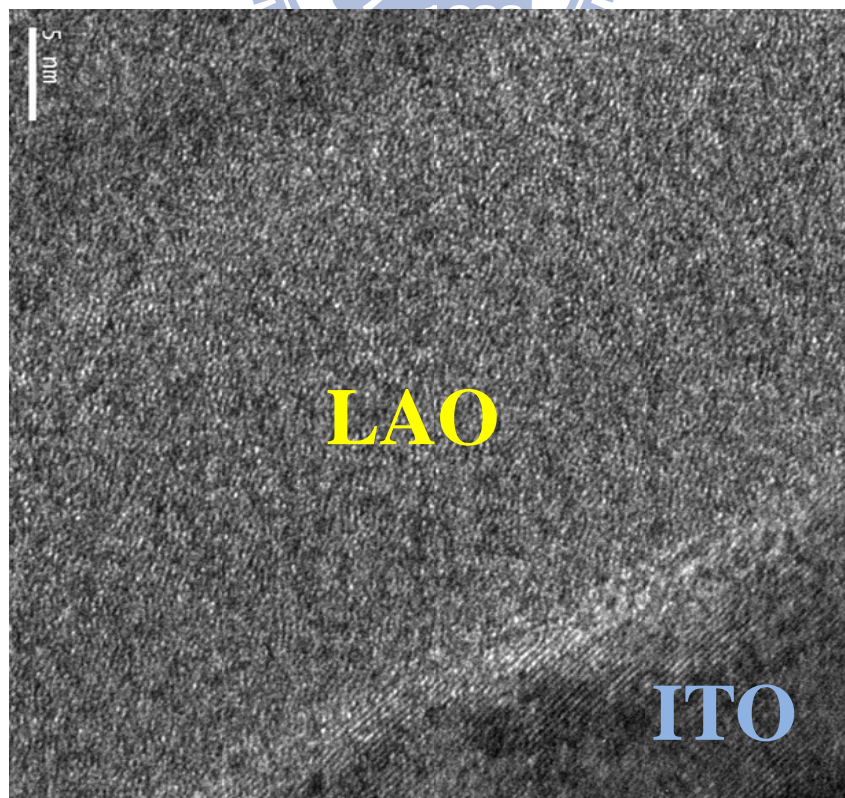
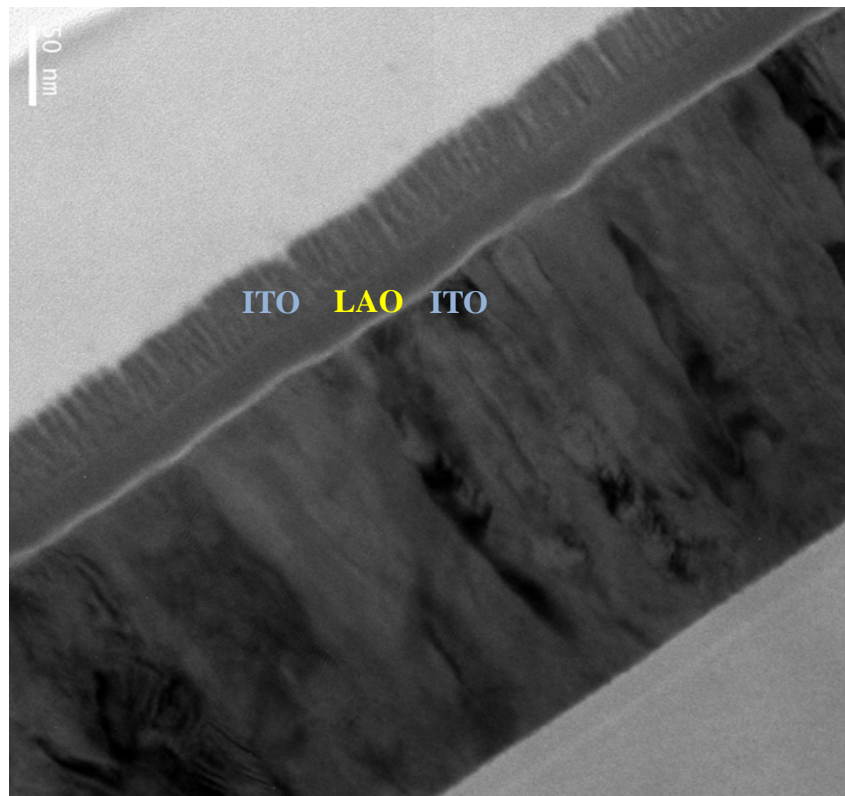


Fig. 3- 27 TEM of the sample with oxygen pressure of 1.4×10^{-2} torr

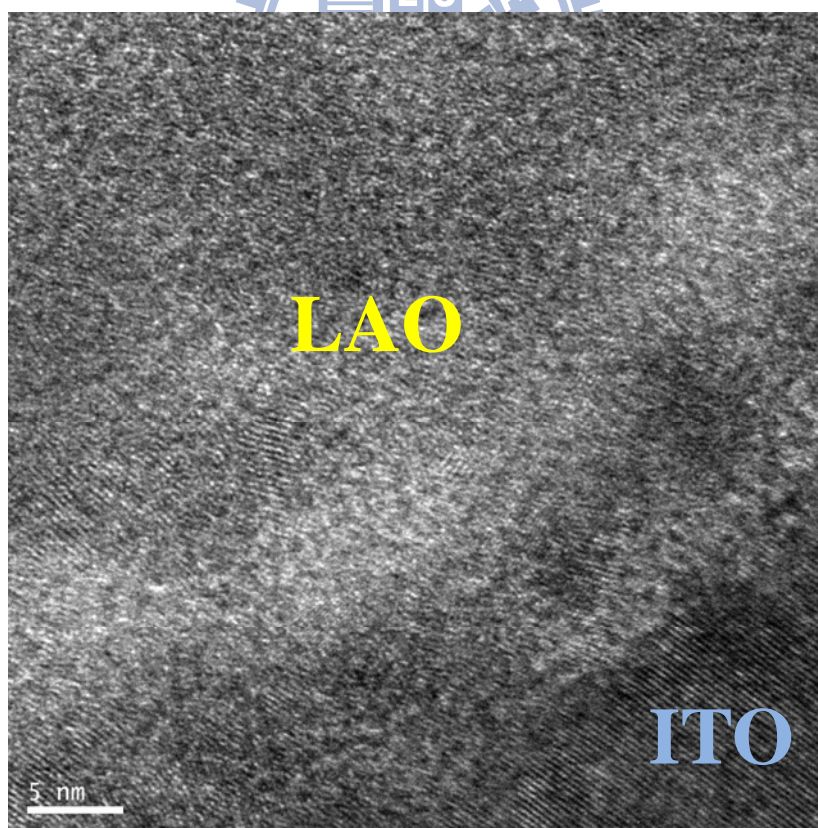
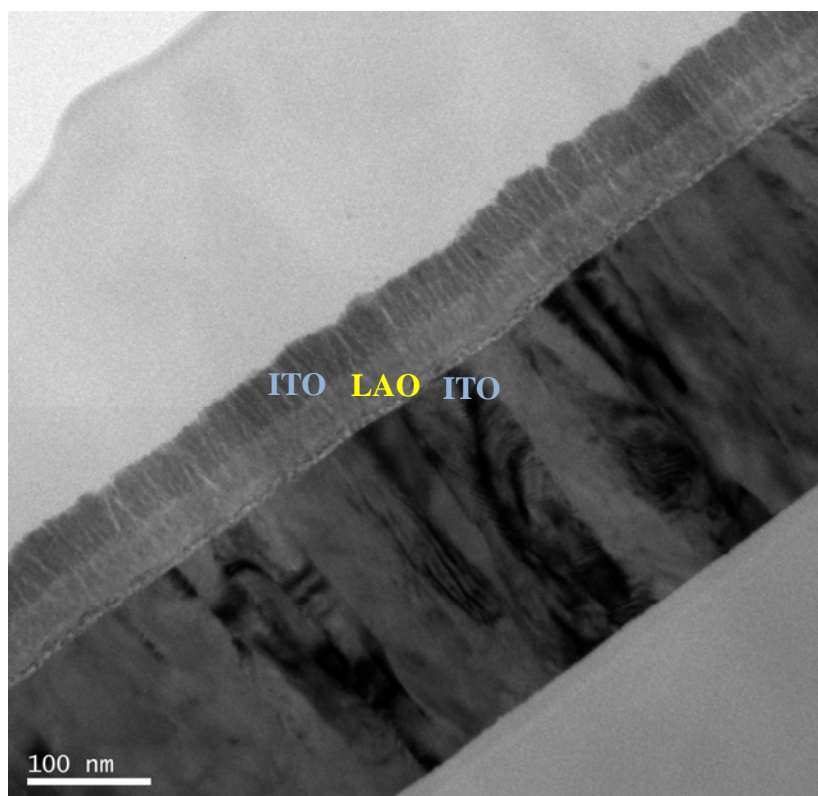


Fig. 3- 28 TEM of the sample with oxygen pressure of 2.8×10^{-2} torr

Chapter 4

Results and Discussion of the LaAlO_3 as a resistive switching layer in RRAM

4.1 Specified some resistive switching parameters

First, we have to define some switching parameters in our experiment. When a small external voltage is applied on the MIM structure, small current can be detected. The small current is called “leakage current”. The larger external voltage is applied, the larger current flow through the insulator and there will be possible a current increasing abrupt. This is call “forming” process, as shown in [Fig 4-1](#). The forming process is the common phenomenon in the metal oxide films which is similar to the dielectric breakdown, named it “soft breakdown”.

In general, resistive switching material exhibits two memory states: the low resistance state (LRS), also named high conducting state (ON-state) and the high resistance state (HRS), also named low conducting state (OFF-state), which can be altered by applying bias voltage, and utilizes the two different resistance values to storage digital data. The resistance value of high resistance state is defined as HRS (R_{off}). The resistance value of low resistance state is defined as LRS (R_{on}). ON process is defined as the transformation from LRS into HRS. Reverse process is defined as the Off process. During ON process, a sudden increase in current occurs at V_{SET} and limited at compliance current. During OFF process, a drop decrease in current occurs at V_{RESET} by dc sweep, as shown in [Fig 4-2](#).

The compliance current (I_{cc}) is an important parameter in RRAM switching operation.. If there is no I_{cc} in operation, large current will cause device “hard breakdown”. Proper I_{cc} value is necessary. Lower I_{cc} value cannot cause HRS to LRS, and larger I_{cc} may cause heat effect that make the device switch unstable, as shown in Fig 4-3. In the proper region, the larger I_{cc} value, the lower LRS.

4.2 comparison of switching properties between LAO thin films with different oxygen pressure

4.2.1 Various magnitude of the positive voltage sweep

Fig 4-4, Fig 4-5 and Fig 4-6 show that the relations between the positive voltage and the current in the LAO thin films with oxygen pressure of 7×10^{-3} , 1.4×10^{-2} and 2.8×10^{-2} torr. Fig 4-7, Fig 4-8 and Fig 4-9 show that the detail of the reset current from different magnitude of the positive voltage in LAO thin films with oxygen pressure of 7×10^{-3} , 1.4×10^{-2} and 2.8×10^{-2} torr. The larger positive voltage is applied, the smaller the reset current conducts through the thin film. We use very small voltage, 0.1 V, to read the resistance after positive voltage is applied. Fig 4-10, Fig 4-11 and Fig 4-12 show that the relations of the HRS and the different magnitude of the reset voltage in LAO thin film with oxygen pressure of 7×10^{-3} , 1.4×10^{-2} and 2.8×10^{-2} torr. We can find out that when we applied more positive voltage on the top electrode of the ITO/LAO/ITO structure, the resistance becomes larger. There are a relationship between the positive E-Field and the resistance.

4.2.2 Various magnitudes of the negative voltage sweep

Fig 4-13, Fig 4-14 and Fig 4-15 show that the relations between the negative voltage and the current in the LAO thin films with oxygen pressure of 7×10^{-3} , 1.4×10^{-2} and 2.8×10^{-2} torr. Fig 4-16, Fig 4-17 and Fig 4-18 show that the detail of the set current from different magnitude of the negative voltage in LAO thin films with oxygen pressure of 7×10^{-3} , 1.4×10^{-2} and 2.8×10^{-2} torr. The smaller negative voltage is applied on the top electrode of the ITO/LAO/ITO structure, the larger the set current conduct through the LAO thin film. We applied very small voltage to read the resistance after negative voltage is applied. Fig 4-19, Fig 4-20 and Fig 4-21 show that the relations of the LRS and the different magnitude of the negative voltage in LAO thin film with oxygen pressure of 7×10^{-3} , 1.4×10^{-2} and 2.8×10^{-2} torr. We can find out that when we applied smaller negative voltage on the structure, the set current becomes larger, and the resistance becomes smaller. There are a relationship between the negative E-Field and the resistance.

4.2.3 Various magnitude of the compliance current

Fig 4-22, Fig 4-23 and Fig 4-24 show that the relations between the compliance current and the conducting current in the LAO thin films with oxygen pressure of 7×10^{-3} , 1.4×10^{-2} and 2.8×10^{-2} torr. We can find out that the larger compliance current is restricted, the larger conducting current after set operation. This interesting phenomenon is result from the larger conducting path is formed because of the larger current conducting through the thin film.

4.2.4 Endurance

Fig 4-25, Fig 4-26 and Fig 4-27 show the endurance of the three samples with oxygen pressure of 7×10^{-3} , 1.4×10^{-2} and 2.8×10^{-2} torr. The sample with oxygen pressure of 7×10^{-3} torr exhibited the smallest operation cycles, but the sample with oxygen pressure of 2.8×10^{-2} torr exhibited the largest operation cycles. The sample with oxygen pressure of 2.8×10^{-2} torr also shows stable resistive switching.

4.4.5 Retention

Fig 4-28, Fig 4-29 and Fig 4-30 show the retention of the three samples with oxygen pressure of 7×10^{-3} , 1.4×10^{-2} and 2.8×10^{-2} torr. The data retention is at least over 10^4 seconds.

4.4.6 Vset/Vreset distribution

Fig 4-31, Fig 4-32 and Fig 4-33 show the Vset/Vreset of the sample with different oxygen pressure of 7×10^{-3} , 1.4×10^{-2} and 2.8×10^{-2} torr. The sample with oxygen pressure of 7×10^{-3} torr shows larger distribution of the Vset and Vreset, and the sample with oxygen pressure of 2.8×10^{-2} torr show small distribution of the Vset and Vreset.

4.4.7 The conduction behavior of the HRS and LRS

Fig 4-34 and Fig 4-35 show the semi-conduction behavior of the HRS, and the Fig 4-36 and 4-37 show the Ohmic conduction behavior of the LRS. According to the different behavior of the two resistance states result from the external bias, the various polarity of the external bias affects the movement of the oxygen in the oxide leading to the two

different resistance states.

4.3 Two pads test to detect the rupture position of the filament

Fig 4-38 shows a schematic diagram of a cross section of the sample structure for the I-V measurement of the ITO/LAO/ITO/LAO/ITO sample. Here, contact 1 and bottom contact 3 (or contact 2 and bottom contact 3) were used to determine the resistance state and operate resistive switching. **Fig 4-39** shows that the current increased dramatically at $\sim -40\text{V}$, and then decreased dramatically at $\sim 45\text{V}$. **Fig 4-40** shows that the resistances change of 1-2 and 1-3 configurations before and after the electroforming. It is believed that the resistance of the 1-2 configuration decrease because of the resistances change of the 1-3 and 2-3 configurations. The resistance of the 1-3 configuration increased dramatically because of the high power of the operation. It is coincide that the resistive switching occurs at the anode.

To prevent the operation from the abnormal electroforming, the forming operation is operated separately. To forming the 1-3 configuration, contact 1 was biased negatively with contact B grounded. To forming the 2-3 configuration, contact 2 was biased positively with contact B grounded. The pristine resistances of the 1-2 and 1-3 configurations are about $\sim 10^8$ ohm. After the subsequent reset and set processes, **Fig 4-41** show that the resistance of the 2-3 configuration changes as a function of the cycle. It is coincided that the resistive switching occurs at the anode.

4.4 Proposed resistive switching mechanisms for ITO/LAO/ITO structure

We proposed a resistive switching mechanism of the ITO/LAO/ITO structure by the oxygen migration model. Fig 4-42 to Fig 4-50 shows the resistive switching mechanism of the ITO/LAO/ITO structure. When the negative bias is applied on the top electrode, an E-Field is generated from the anode to the cathode. The E-Field makes the oxygen ions move from the cathode to the anode. When the larger voltage is applied on the device, the larger E-Field make the oxygen migrate apparently as show in Fig 4-45. The large E-Field leads to a significant increase of the oxygen vacancy concentration near the cathode, and a strong depletion of the oxygen vacancy concentration in a somewhat larger anodic region. The region near the cathode is an n-conductivity, and the region near the anode is a p-conductivity, as show in Fig 4-46. The n-conducting cathodic region is called “virtual cathode”, and it extend toward the anode. If the virtual cathode almost touches the anode, the resistance of the device decreases dramatically. This is called “electroforming”. If the positive bias is applied to the top electrode, the E-Field results in the oxygen migration from the anode to the cathode, and the oxygen recombined with the vacancy near the cathode. The current through oxide decreased dramatically, as show in Fig 4-48, and the off-state is finished. If the negative bias is applied to the top electrode, the E-Field results in the oxygen migration from the cathode to the anode, and the oxygen vacancies are attracted from the virtual electrode to the metal contact and

turning the contact into the on-state, as show in Fig 4-50. Apparently, the oxygen migration by the different polarity of the E-Field between the virtual and the contact constitutes the core process of the bipolar switching.



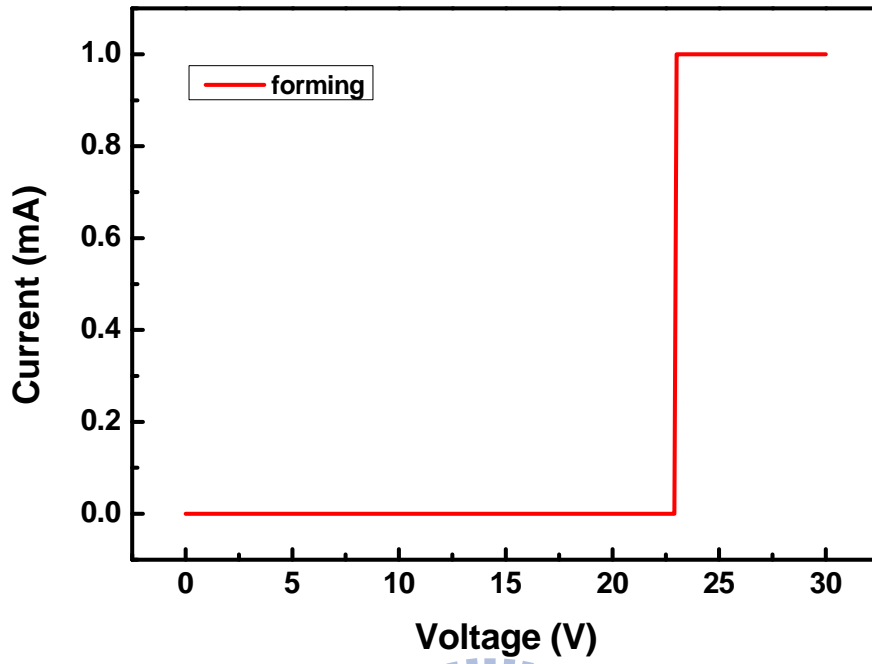


Fig. 4- 1 Forming process

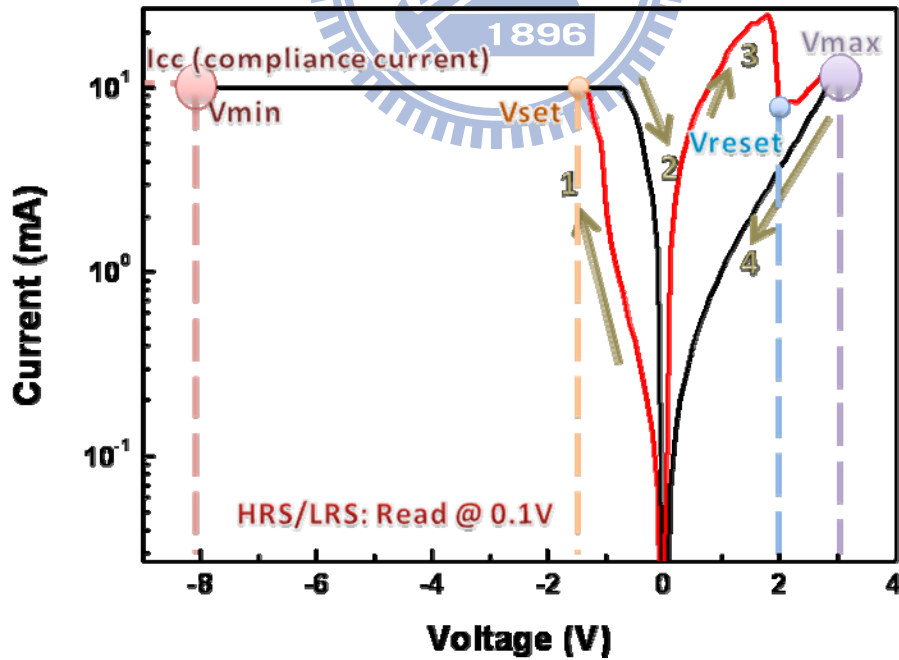


Fig. 4- 2 Operation process of the RRAM

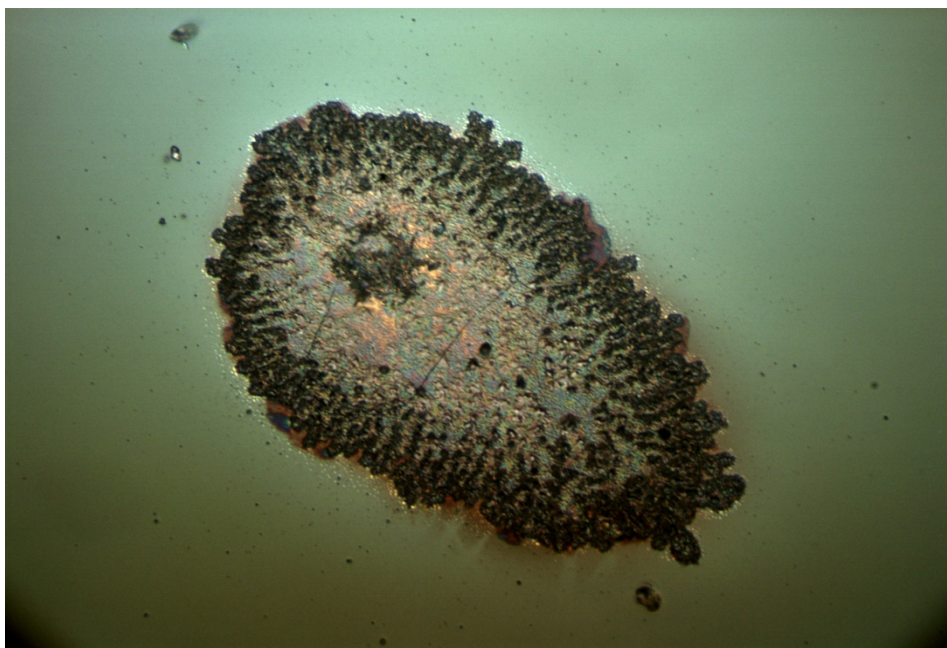


Fig. 4- 3 Heat effect

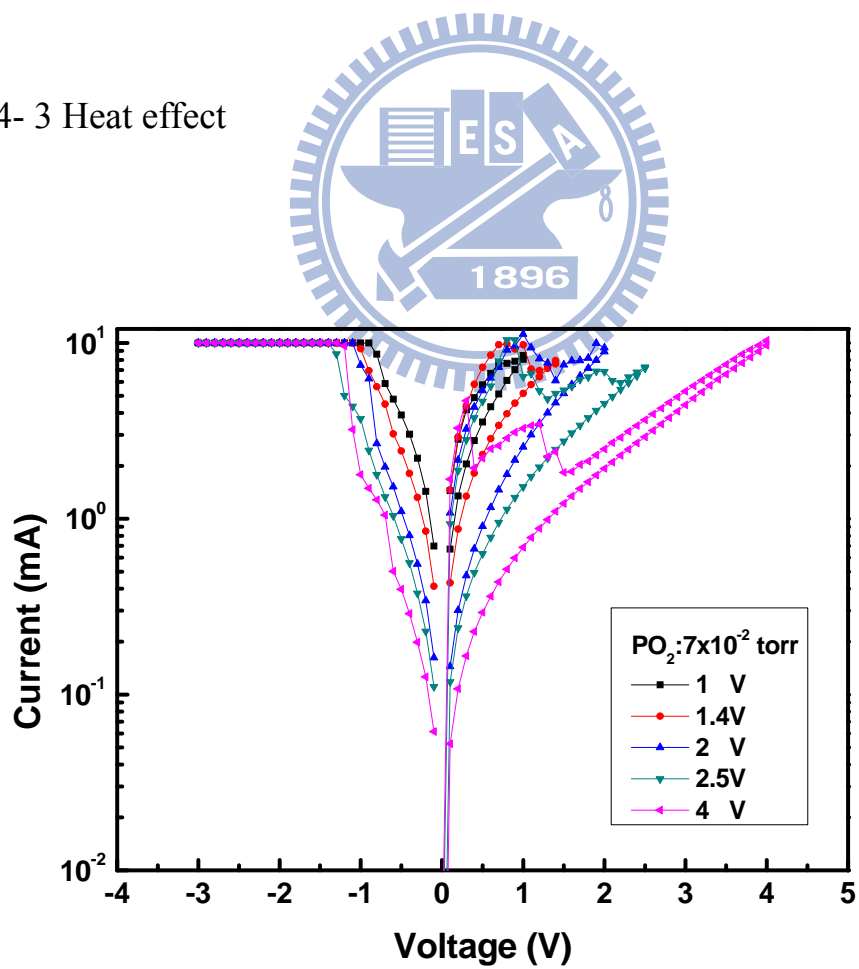


Fig. 4- 4 Relation between the reset voltage and the current in the LAO thin film with oxygen pressure of 7×10^{-3} torr

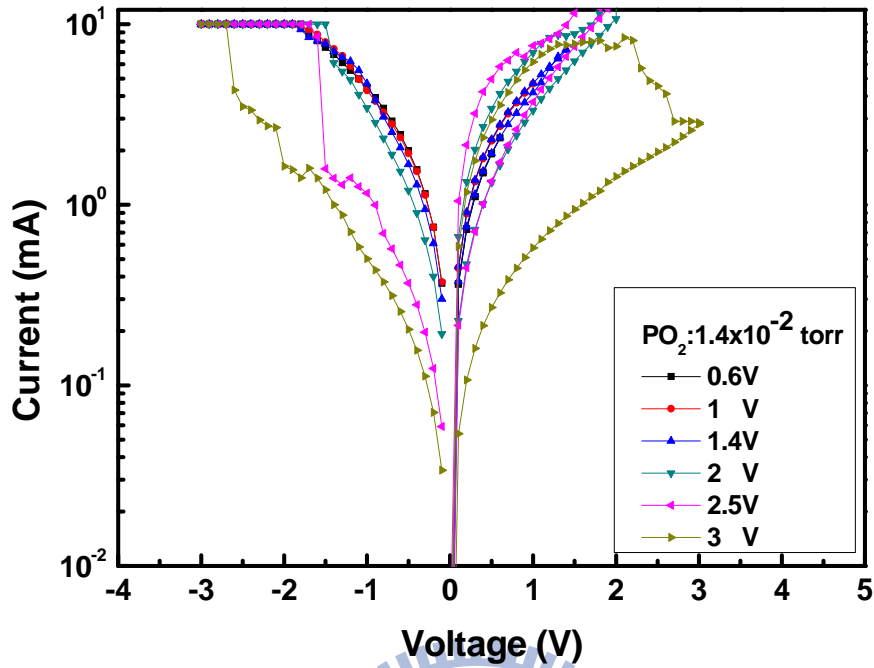


Fig. 4- 5 Relation between the reset voltage and the current in the LAO thin film with oxygen pressure of 1.4×10^{-2} torr

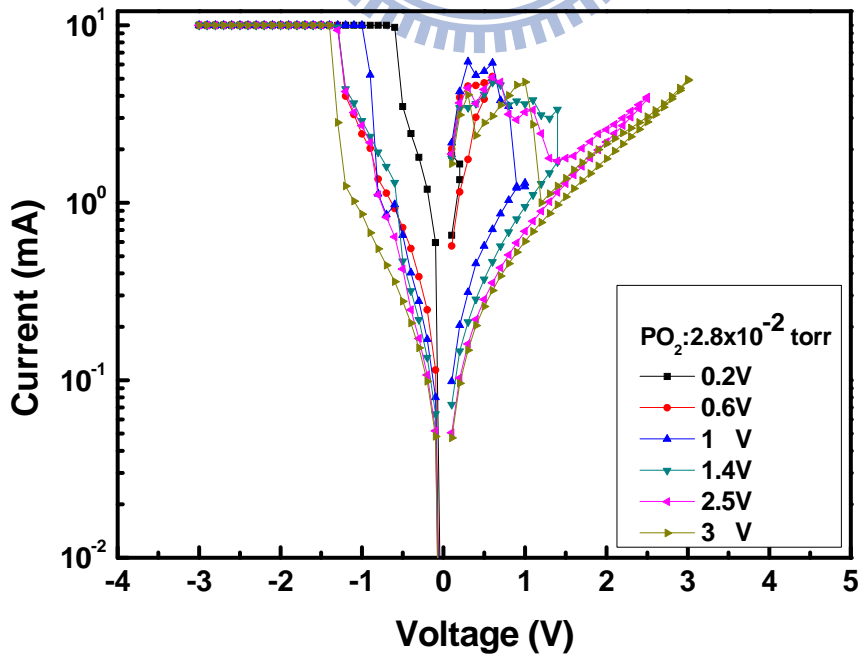


Fig. 4- 6 Relation between the reset voltage and the current in the LAO thin film with oxygen pressure of 2.8×10^{-2} torr

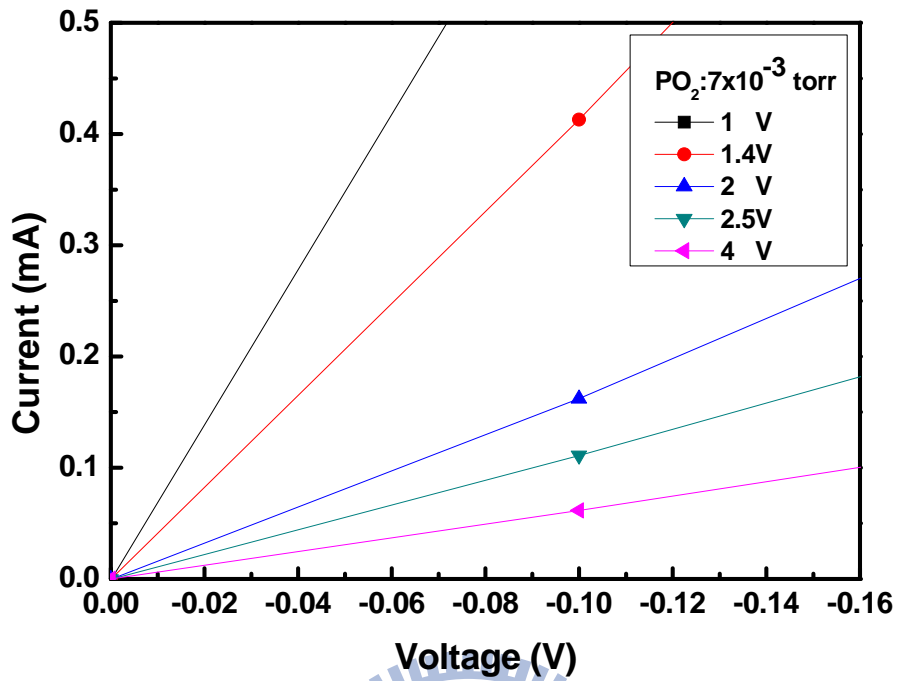


Fig. 4- 7 Detail of the reset current from different magnitude of the reset voltage in LAO thin film with oxygen pressure of 7×10^{-3} torr

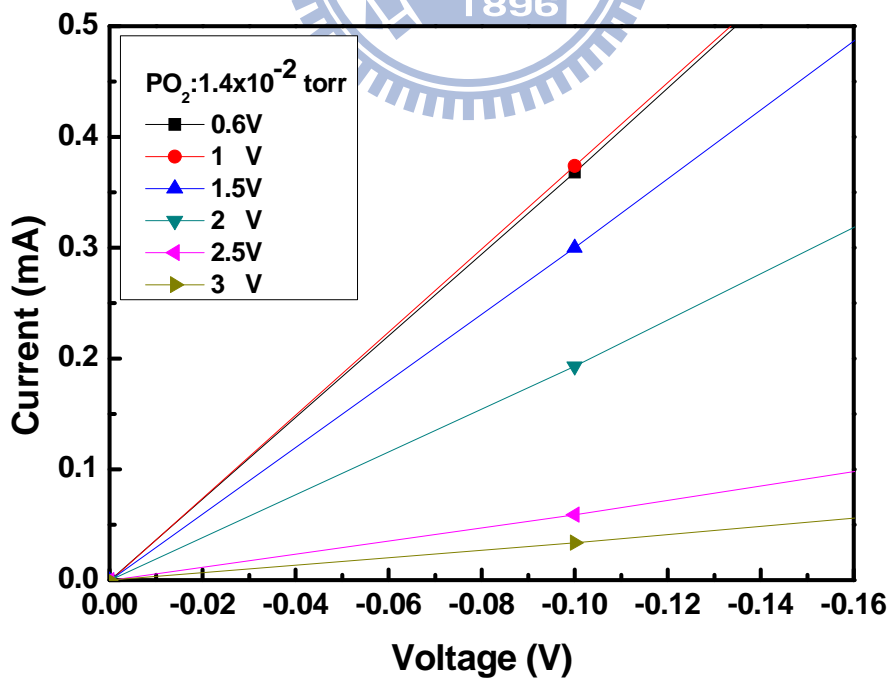


Fig. 4- 8 Detail of the reset current from different magnitude of the reset voltage in LAO thin film with oxygen pressure of 1.4×10^{-2} torr

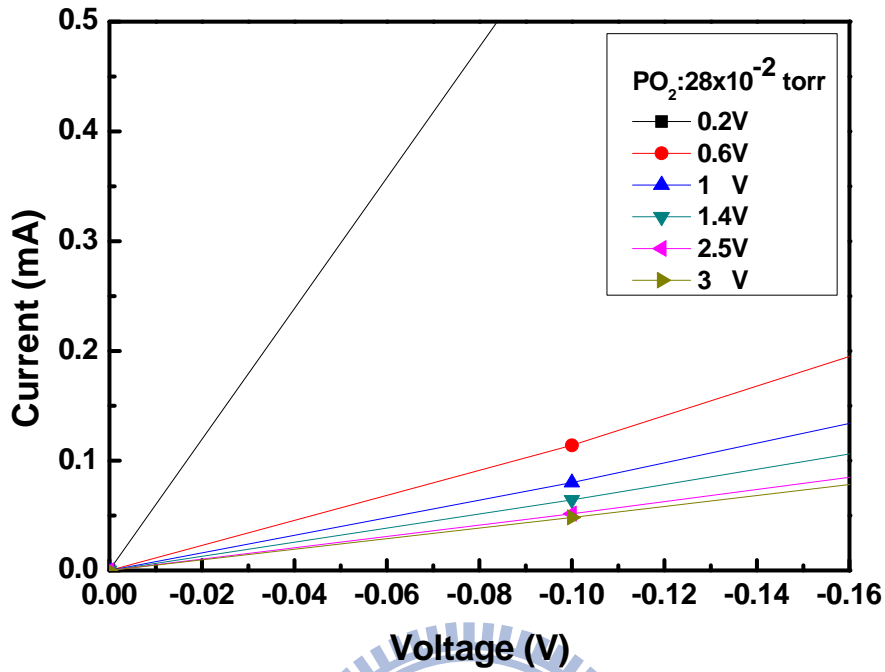


Fig. 4- 9 Detail of the reset current from different magnitude of the reset voltage in LAO thin film with oxygen pressure of 2.8×10^{-2} torr

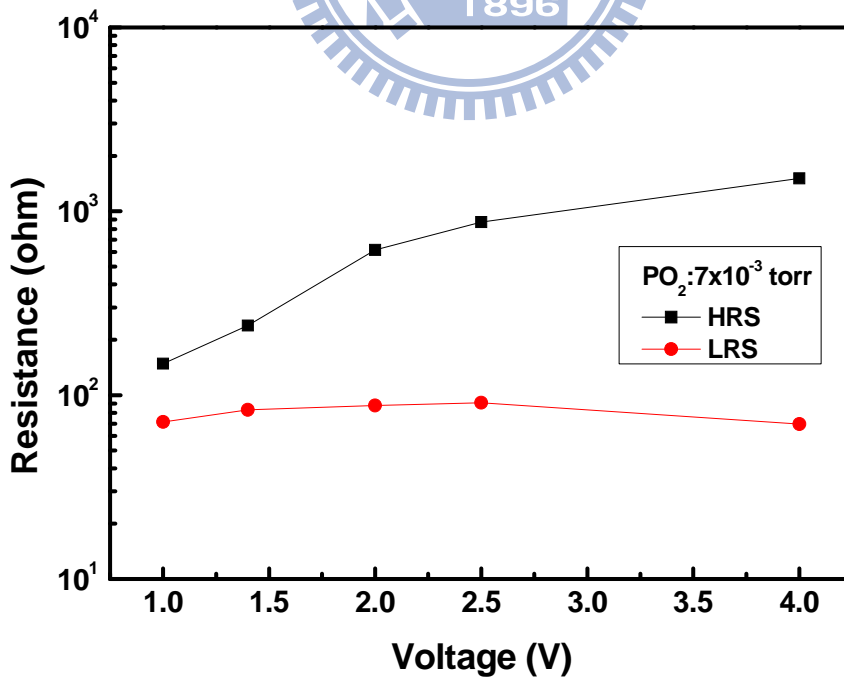


Fig. 4- 10 Relation of the HRS and the different magnitude of the reset voltage in LAO thin film with oxygen pressure of 7×10^{-3} torr

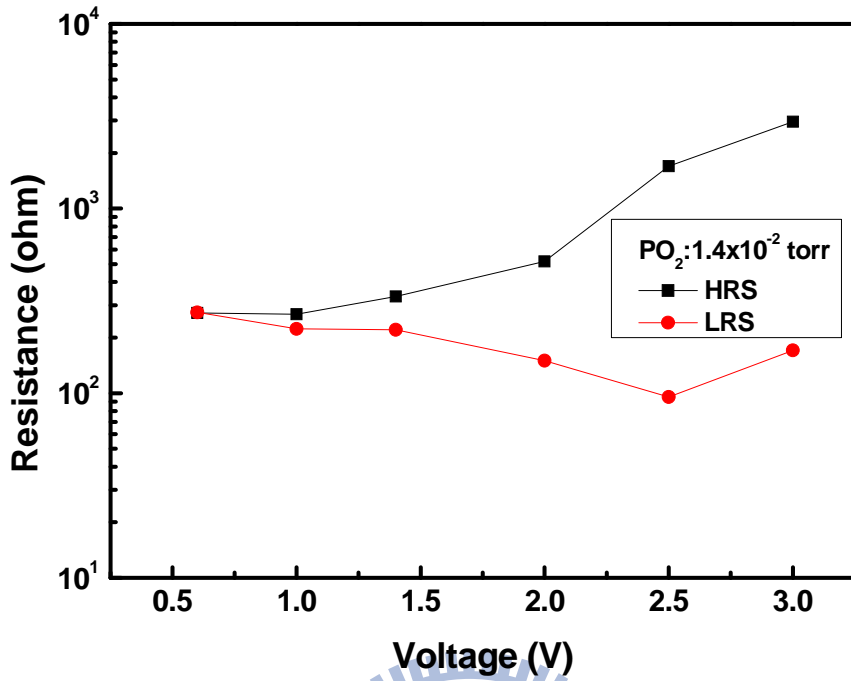


Fig. 4- 11 Relation of the HRS and the different magnitude of the reset voltage in LAO thin film with oxygen pressure of 1.4×10^{-2} torr

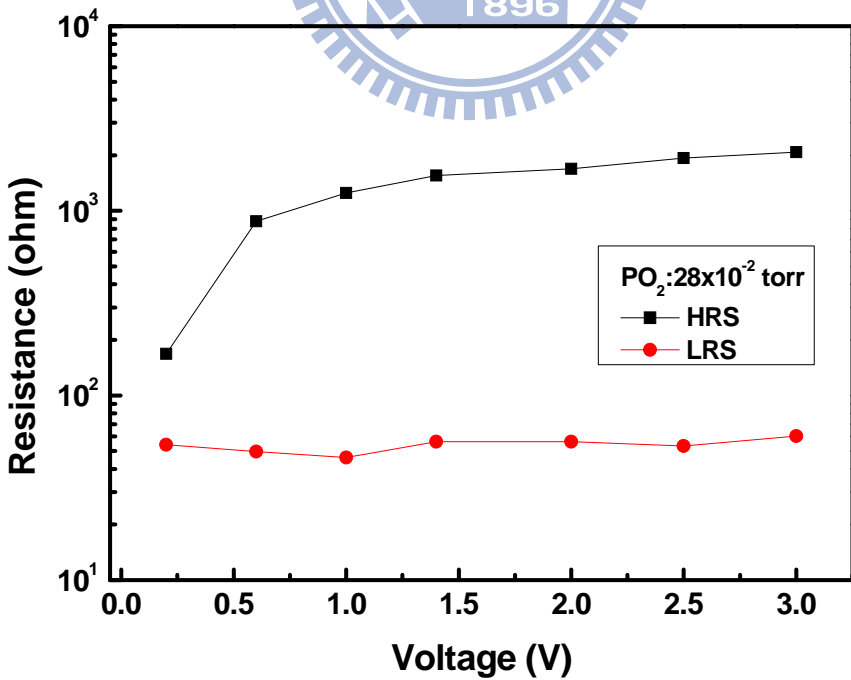


Fig. 4- 12 Relation of the HRS and the different magnitude of the reset voltage in LAO thin film with oxygen pressure of 2.8×10^{-2} torr

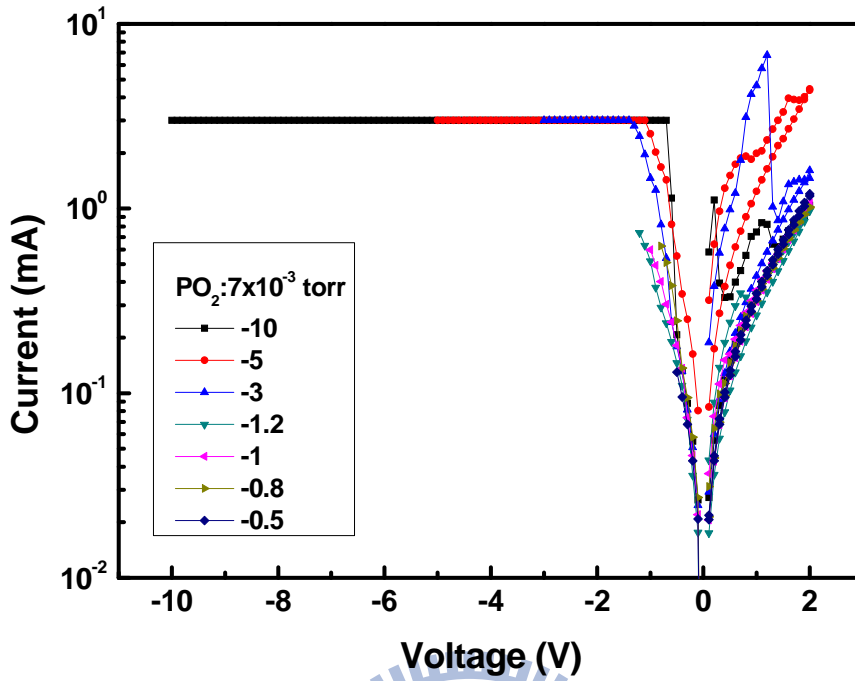


Fig. 4- 13 Relation between the negative voltage and the current in the LAO thin film with oxygen pressure of 7×10^{-3} torr

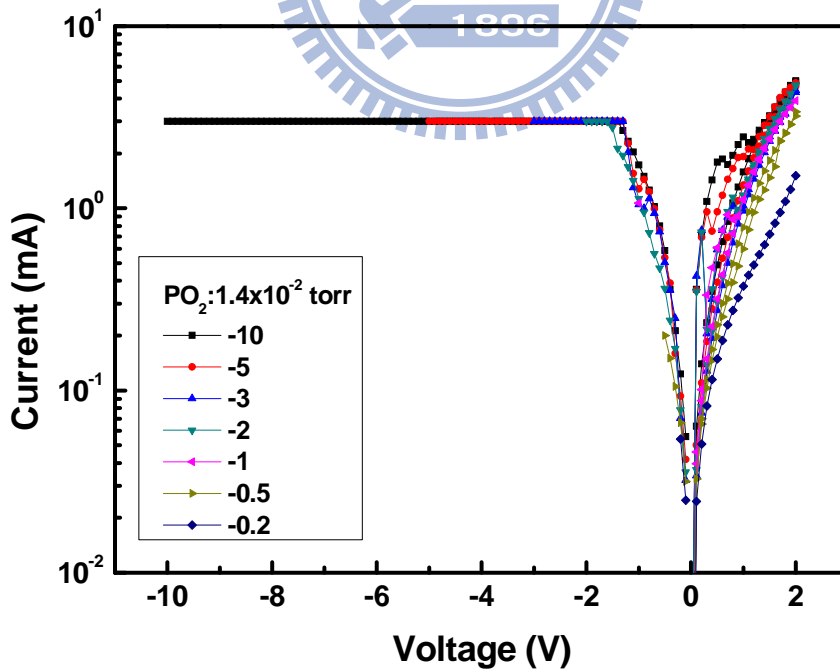


Fig. 4- 14 Relation between the negative voltage and the current in the LAO thin film with oxygen pressure of 1.4×10^{-2} torr

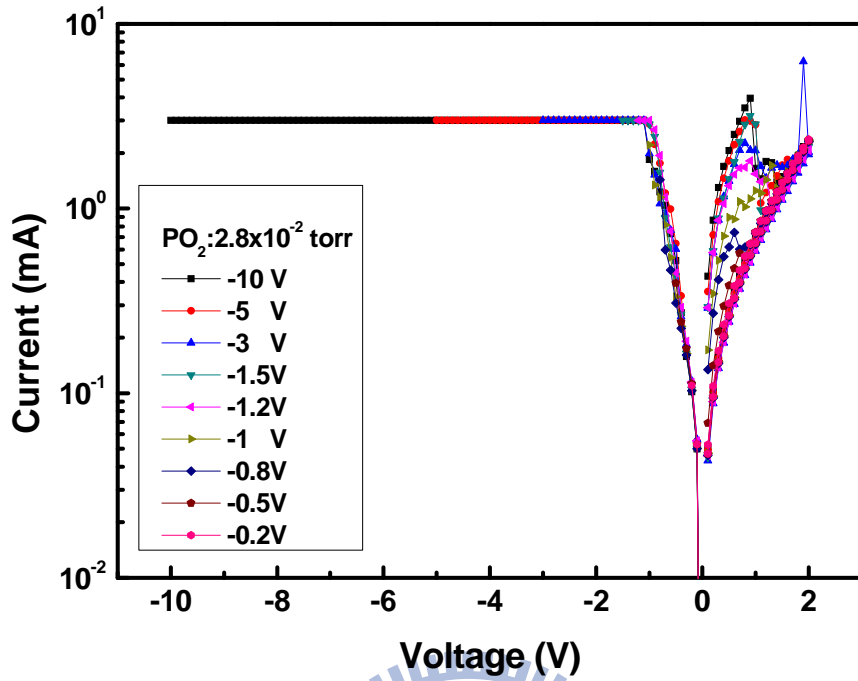


Fig. 4- 15 Relation between the negative voltage and the current in the LAO thin film with oxygen pressure of 2.8×10^{-2} torr

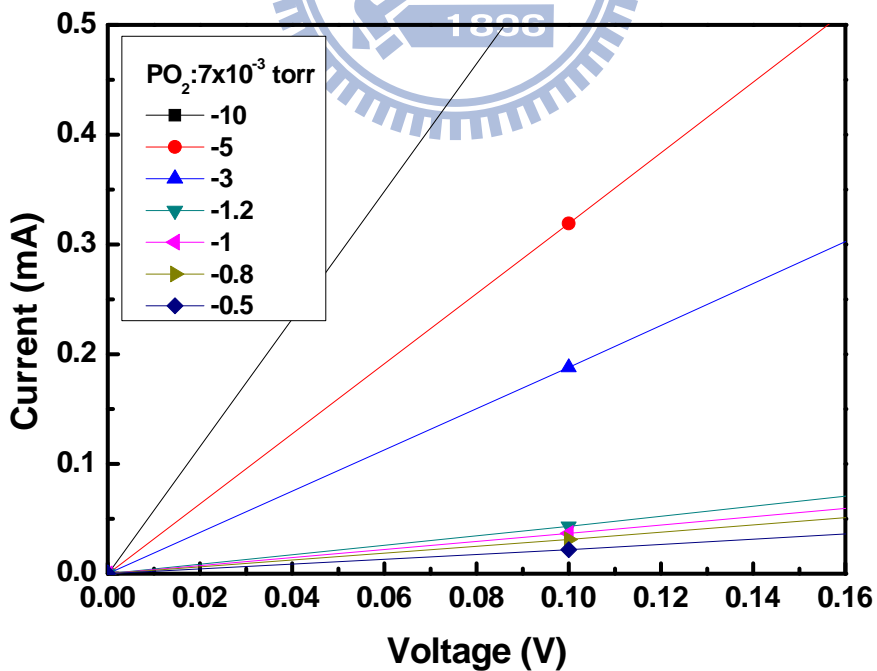


Fig. 4- 16 Detail of the set current from different magnitude of the negative voltage in LAO thin film with oxygen pressure of 7×10^{-3} torr

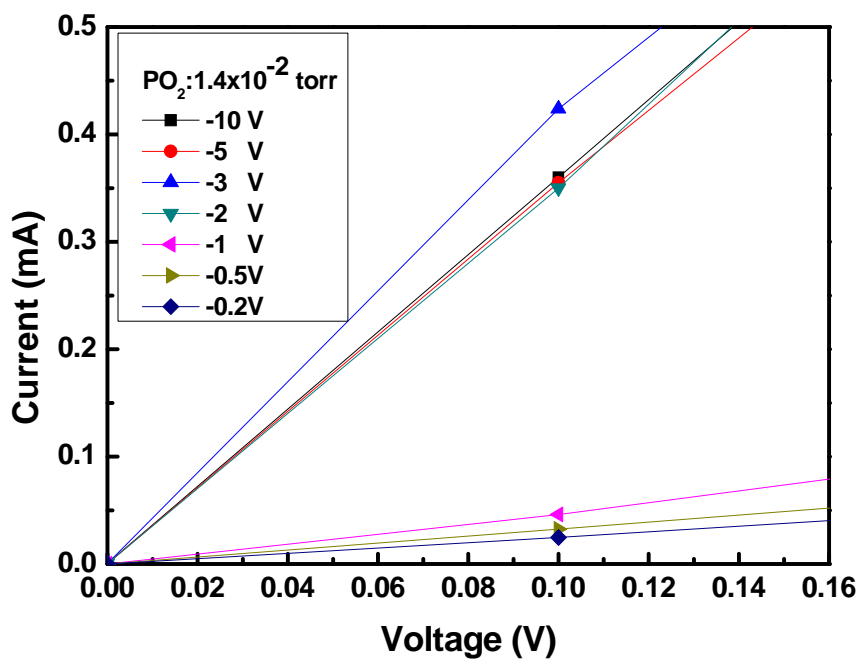


Fig. 4- 17 Detail of the set current from different magnitude of the negative voltage in LAO thin film with oxygen pressure of 1.4×10^{-2} torr

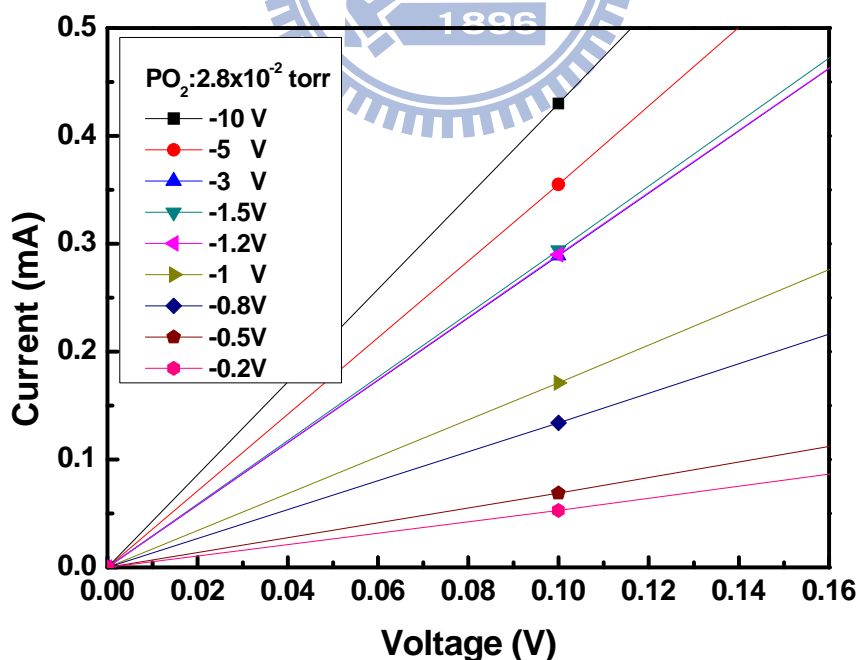


Fig. 4- 18 Detail of the set current from different magnitude of the negative voltage in LAO thin film with oxygen pressure of 2.8×10^{-2} torr

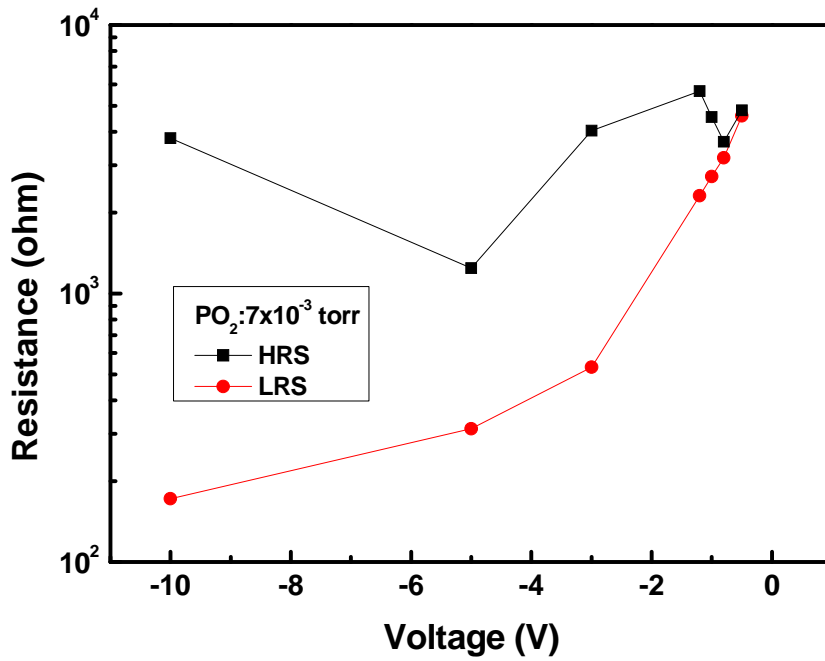


Fig. 4- 19 Relation of the LRS and the different magnitude of the negative voltage in LAO thin film with oxygen pressure of 7×10^{-3} torr

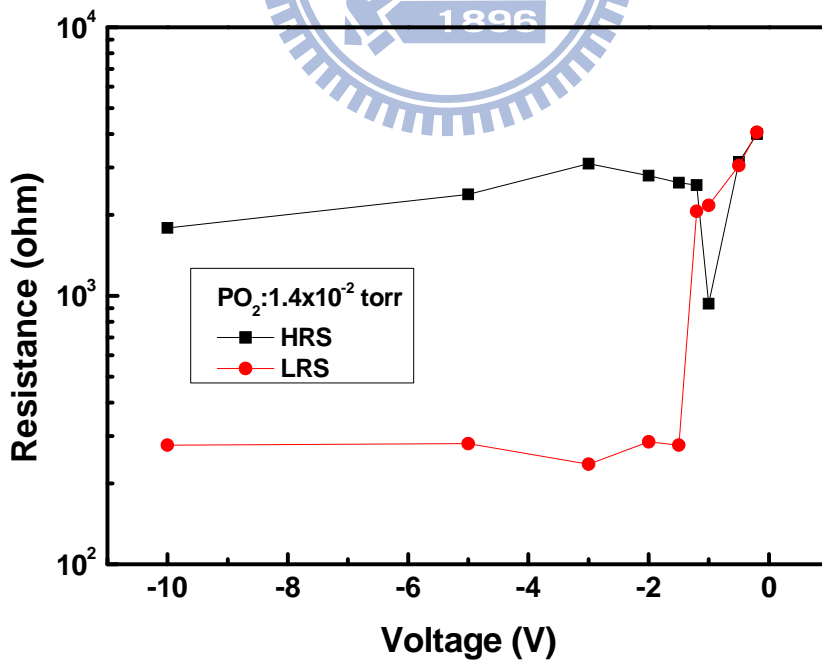


Fig. 4- 20 Relation of the LRS and the different magnitude of the negative voltage in LAO thin film with oxygen pressure of 1.4×10^{-2} torr

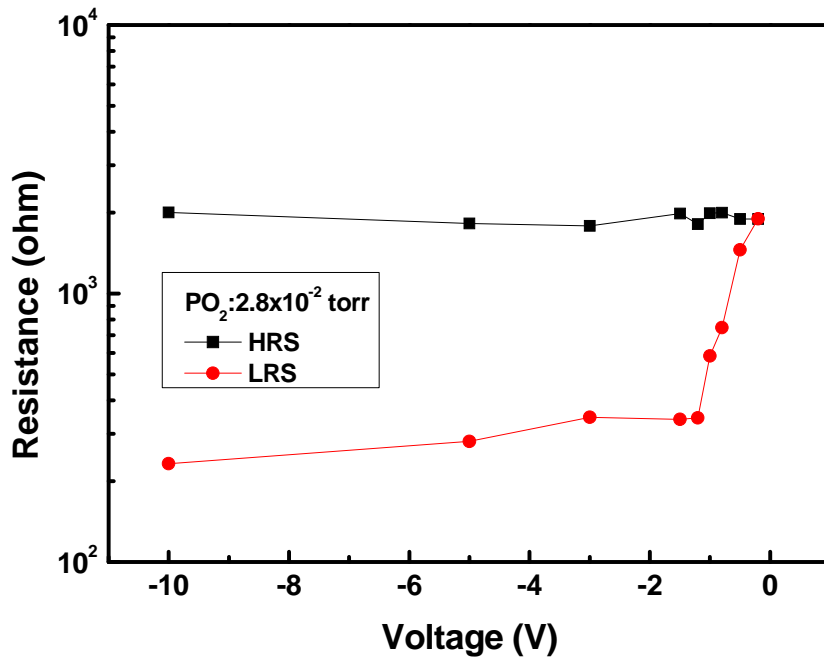


Fig. 4- 21 Relation of the LRS and the different magnitude of the negative voltage in LAO thin film with oxygen pressure of 2.8×10^{-2} torr

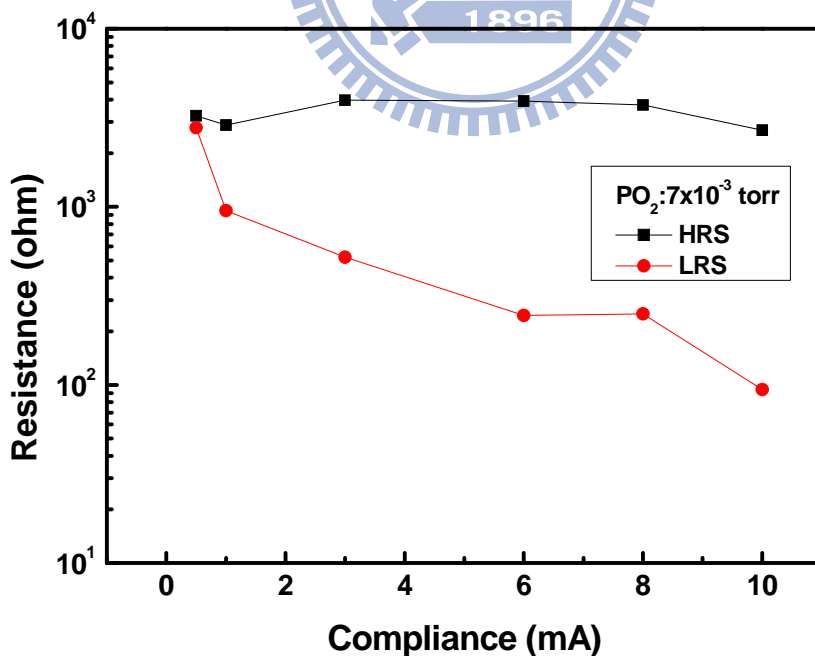


Fig. 4- 22 Relation of the LRS and the different magnitude of the compliance current in LAO thin film with oxygen pressure of 7×10^{-3} torr

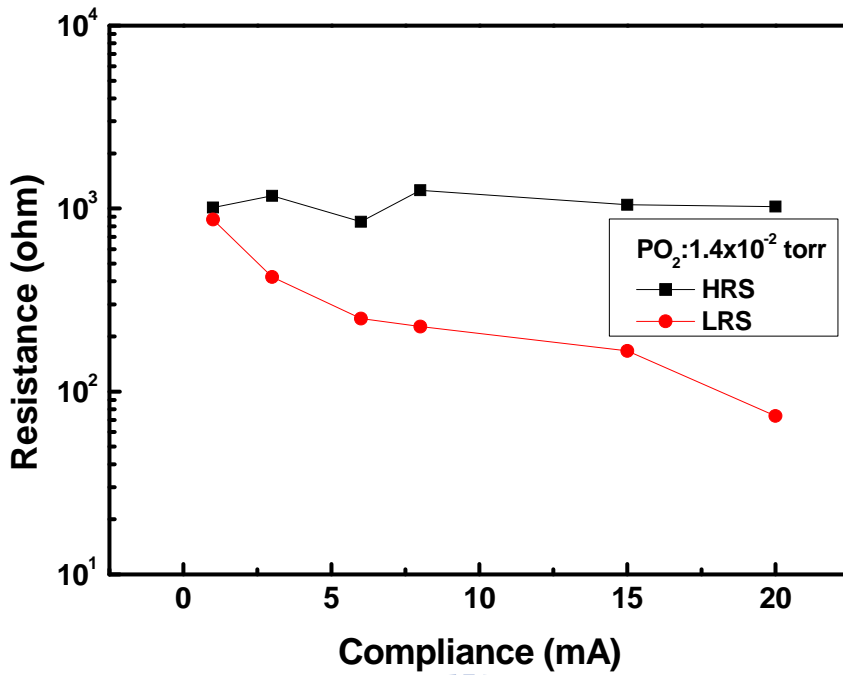


Fig. 4- 23 Relation of the LRS and the different magnitude of the compliance current in LAO film with oxygen pressure of 1.4×10^{-2} torr

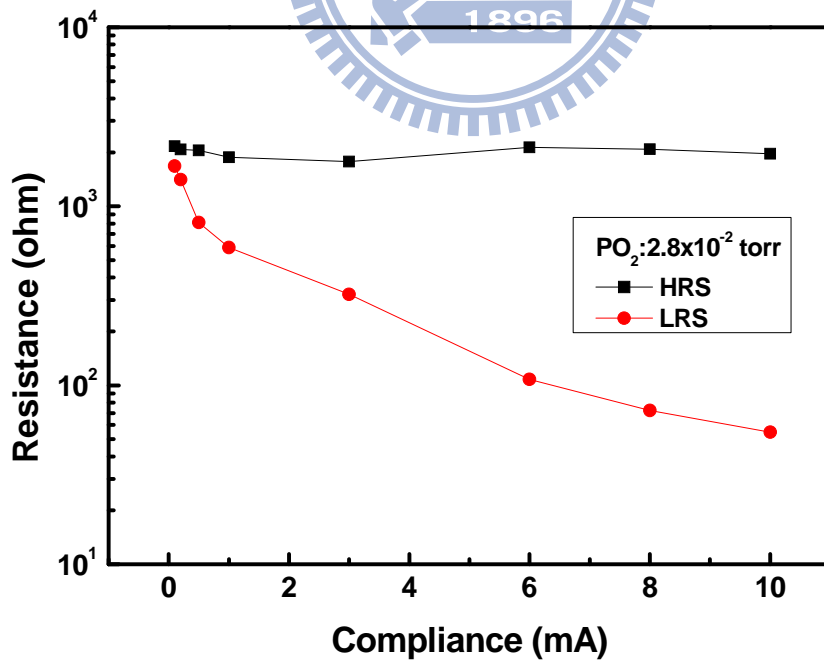


Fig. 4- 24 Relation of the LRS and the different magnitude of the compliance current in LAO film with oxygen pressure of 2.8×10^{-2} torr

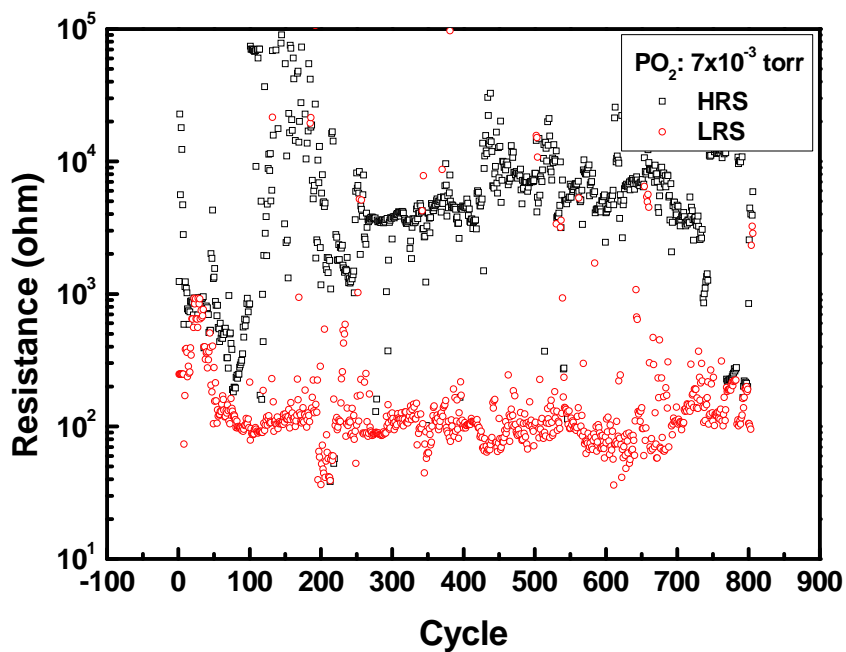


Fig. 4- 25 Endurance of the ITO/LAO/ITO sample with oxygen pressure of 7×10^{-3} torr

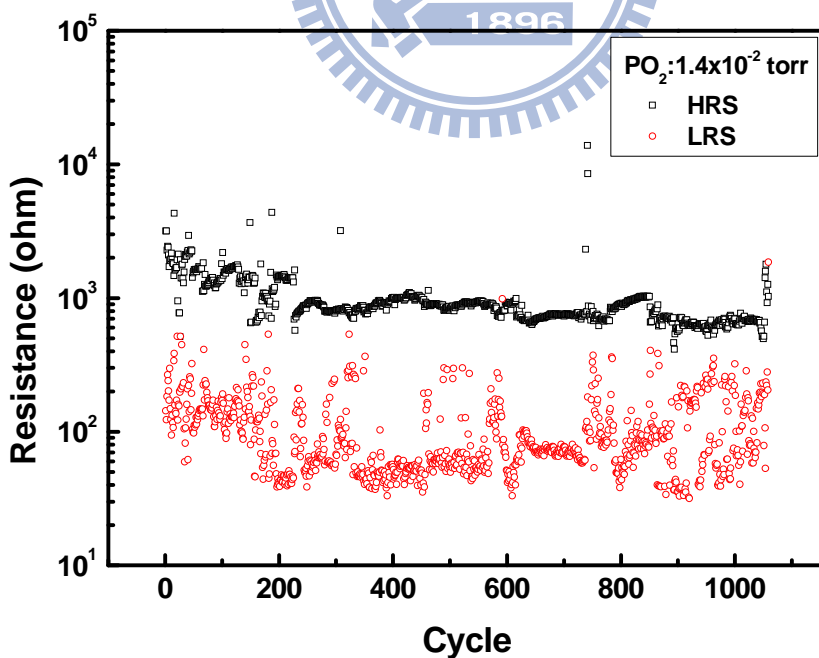


Fig. 4- 26 Endurance of the ITO/LAO/ITO sample with oxygen pressure of 1.4×10^{-2} torr

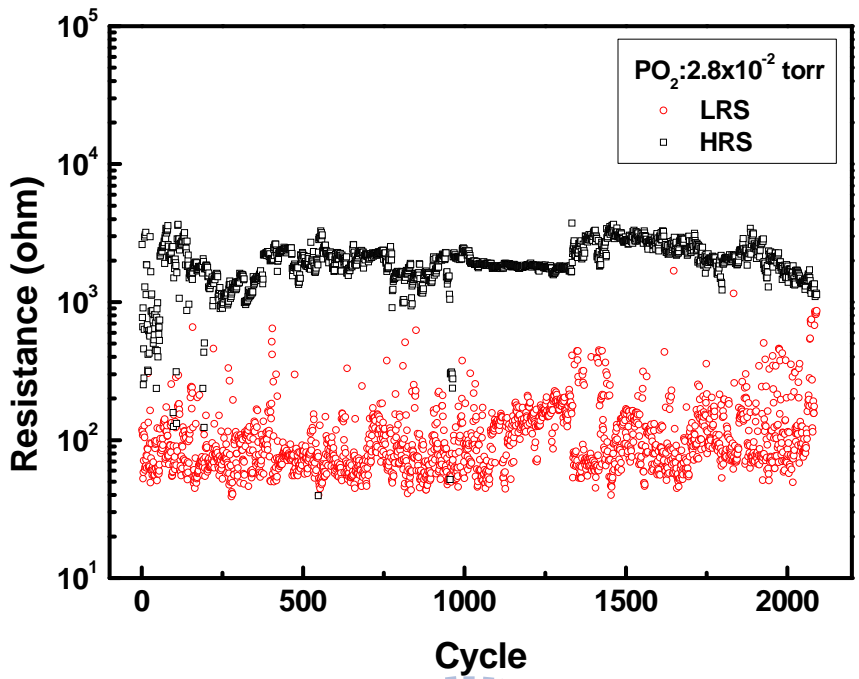


Fig. 4- 27 Endurance of the ITO/LAO/ITO sample with oxygen pressure of 2.8×10^{-2} torr

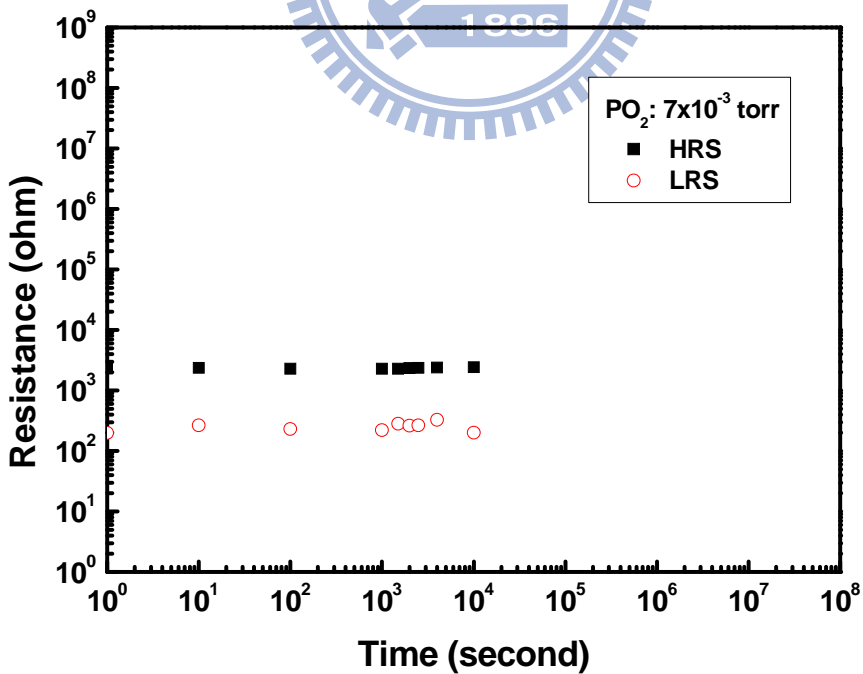


Fig. 4- 28 Retention of the ITO/LAO/ITO sample with oxygen pressure of 7×10^{-3} torr

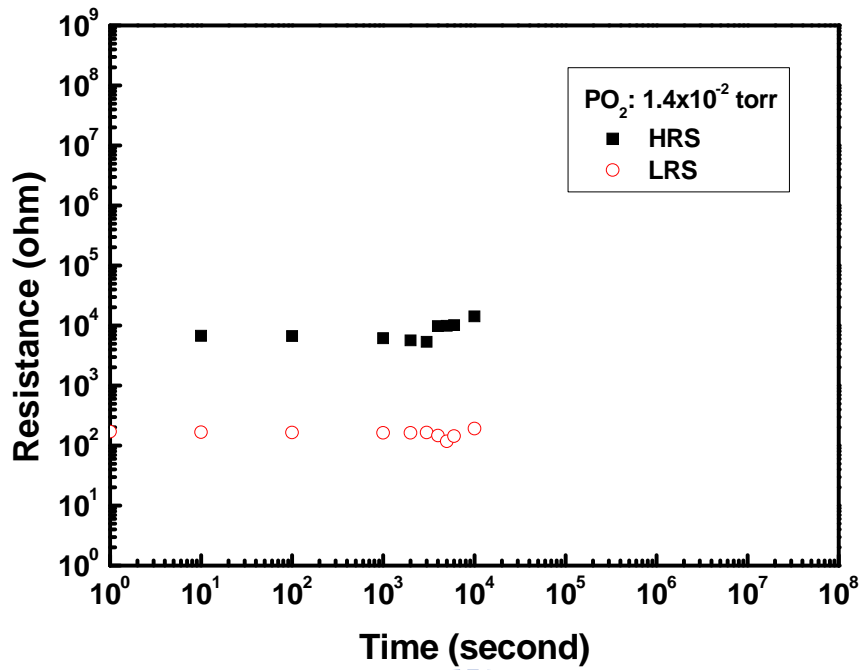


Fig. 4- 29 Retention of the ITO/LAO/ITO sample with oxygen pressure of 1.4×10^{-2} torr

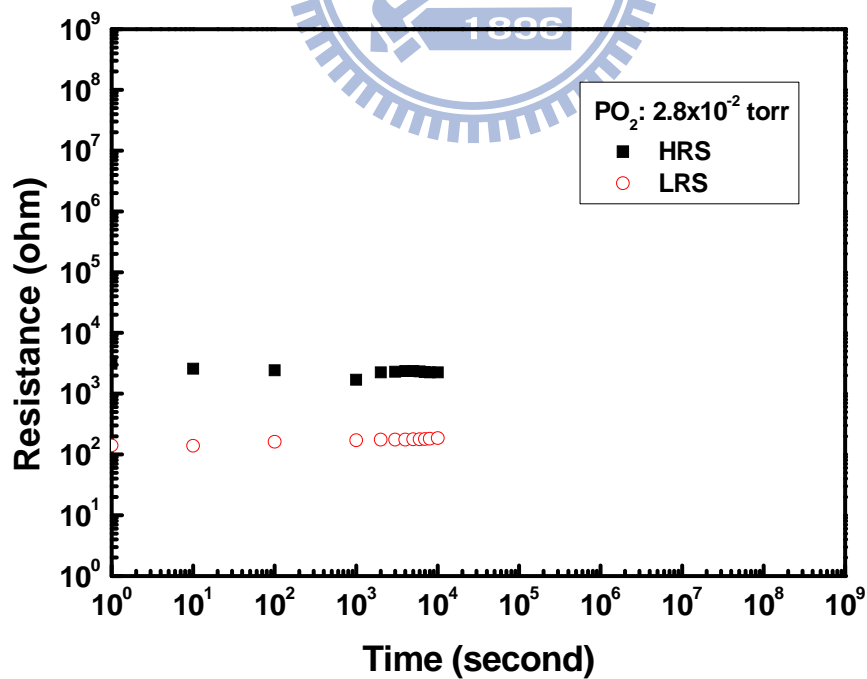


Fig. 4- 30 Retention of the ITO/LAO/ITO sample with oxygen pressure of 2.8×10^{-2} torr

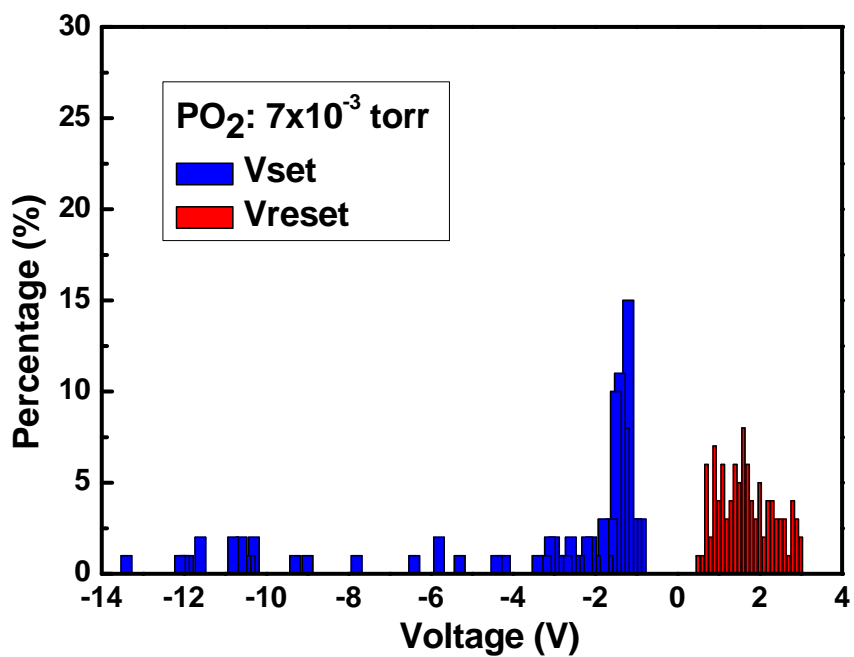


Fig. 4- 31 Vset/Vreset distribution of the sample with oxygen pressure of 7×10^{-3} torr

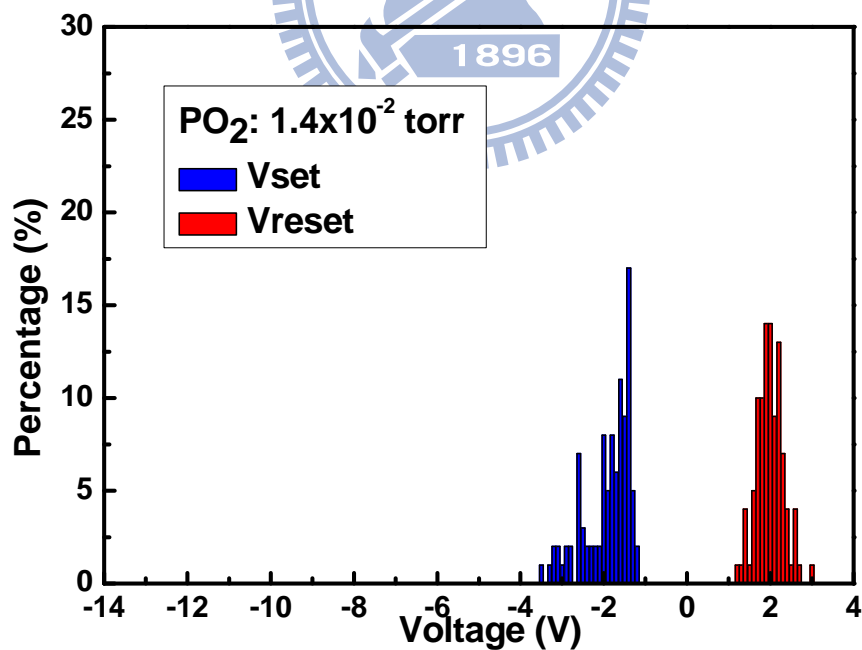


Fig. 4- 32 Vset/Vreset distribution of the sample with oxygen pressure of 1.4×10^{-2} torr

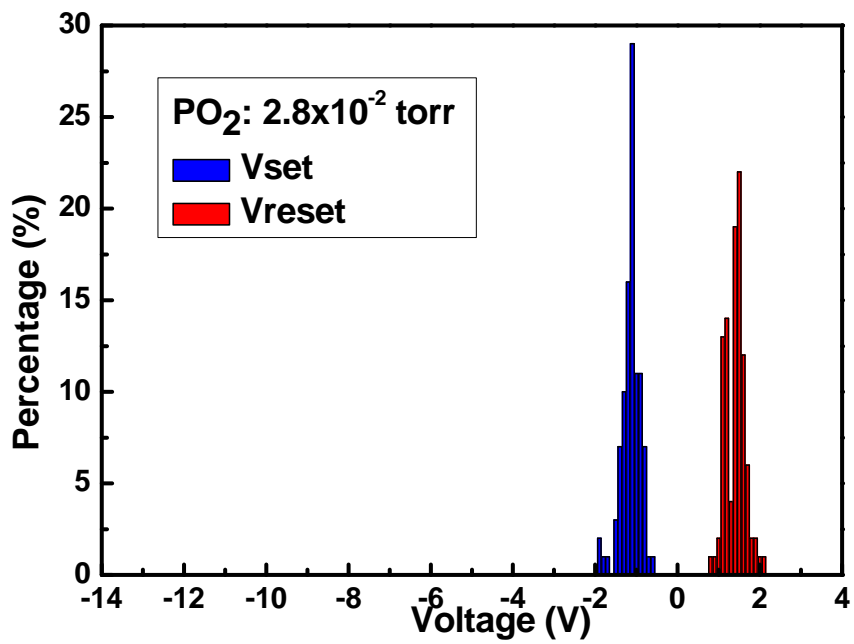


Fig. 4- 33 Vset/Vreset distribution of the sample with oxygen pressure of 2.8×10^{-2} torr

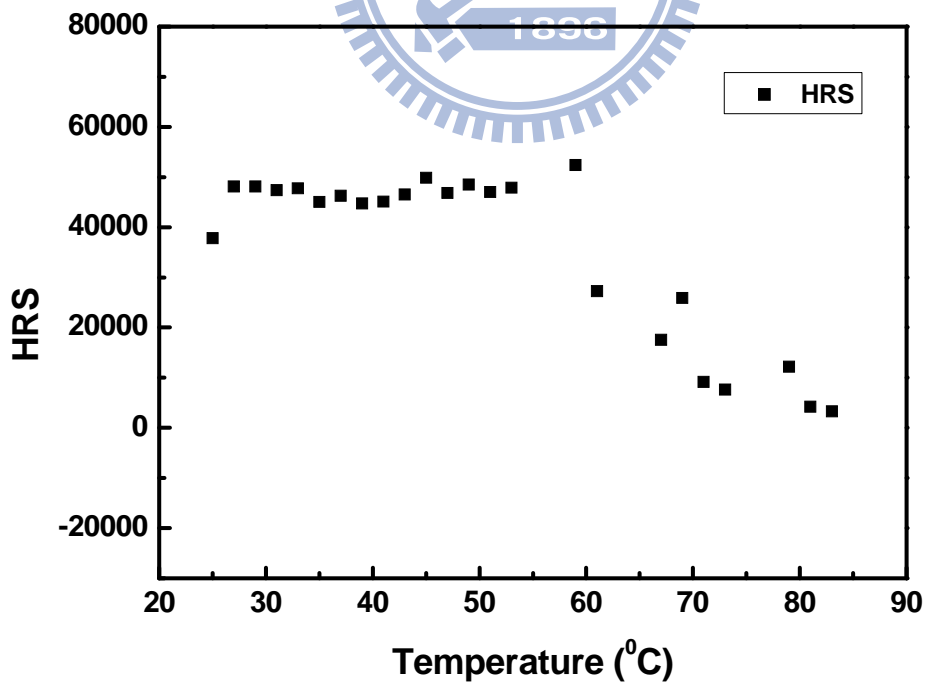


Fig. 4- 34 Relation between the HRS and the temperature show semiconductor-like behavior

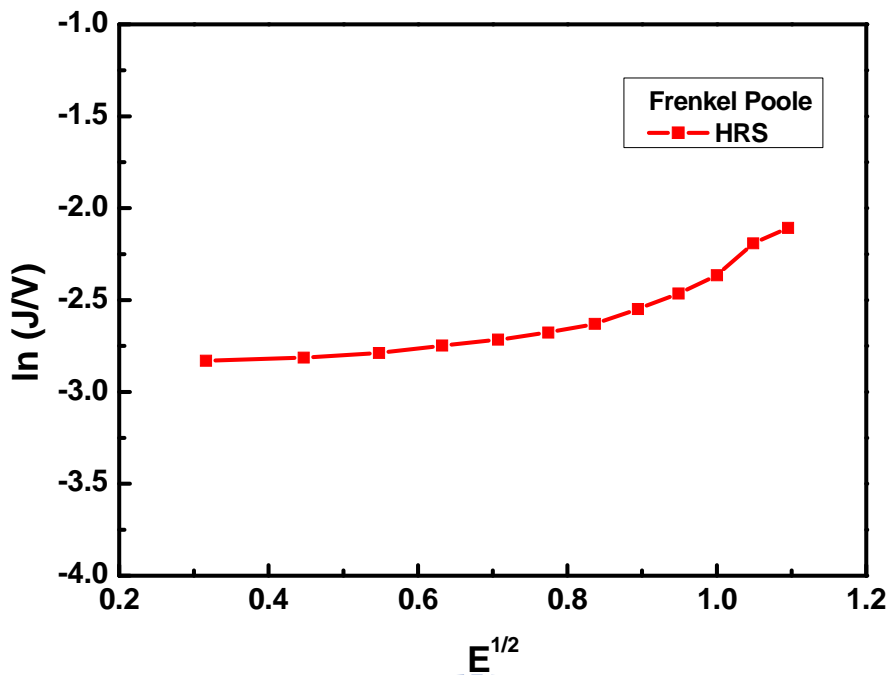


Fig. 4- 35 Frenkel Poole behavior of the HRS

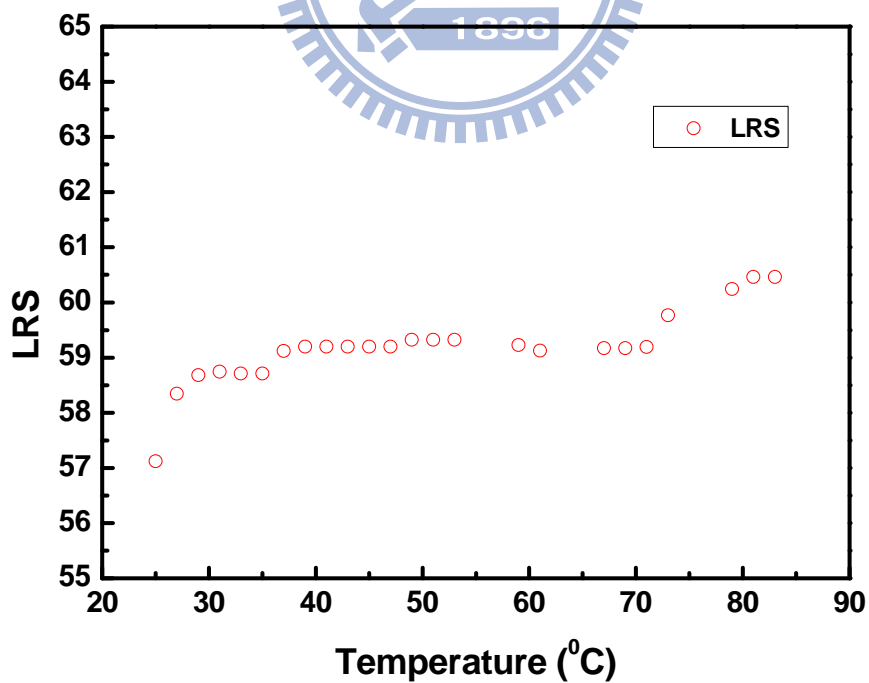


Fig. 4- 36 Relation between the HRS and the temperature show metallic behavior

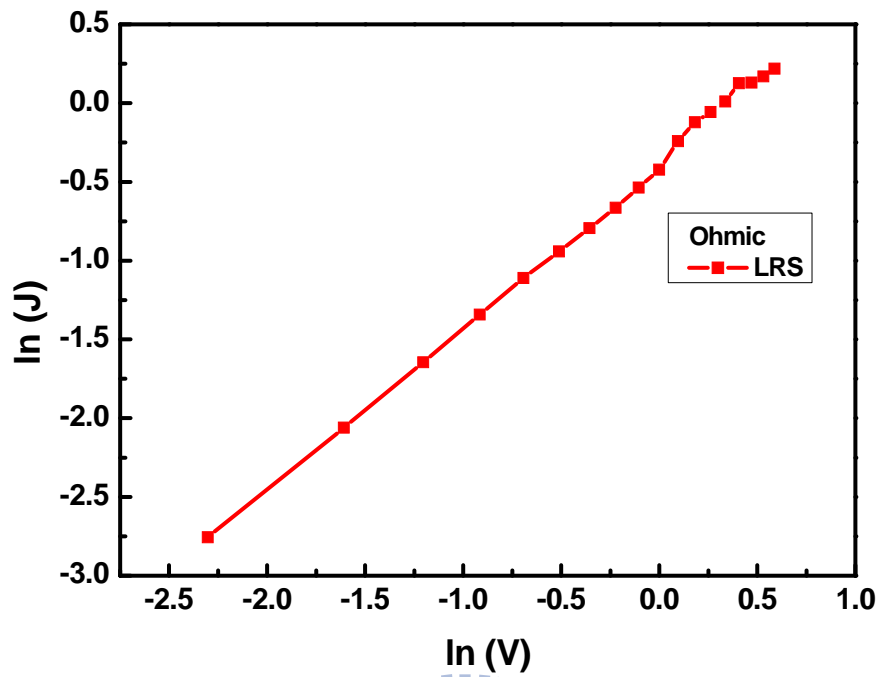


Fig. 4- 37 Ohmic behavior of the LRS

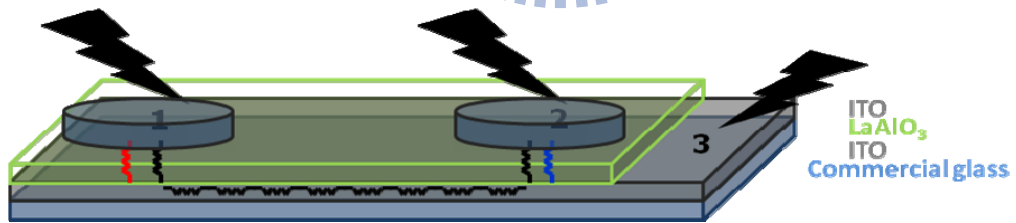
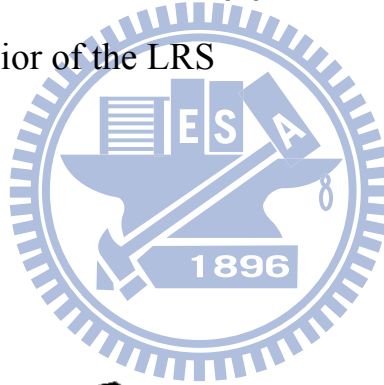


Fig. 4- 38 Schematic diagram of a cross section of the sample structure for the I-V measurement of the ITO/LAO/ITO/LAO/ITO sample

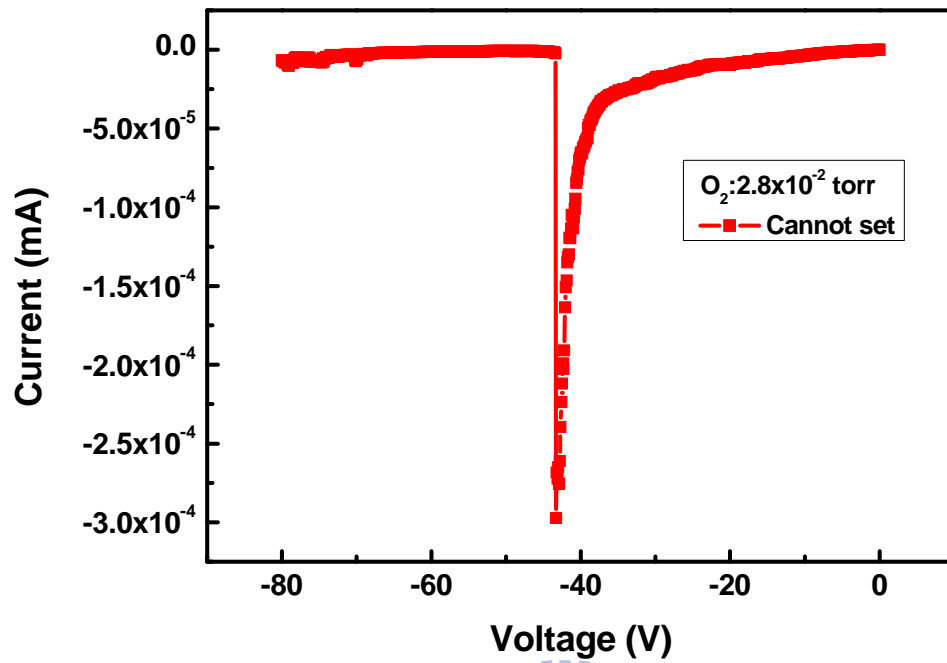


Fig. 4- 39 Abnormal forming of the two pads test

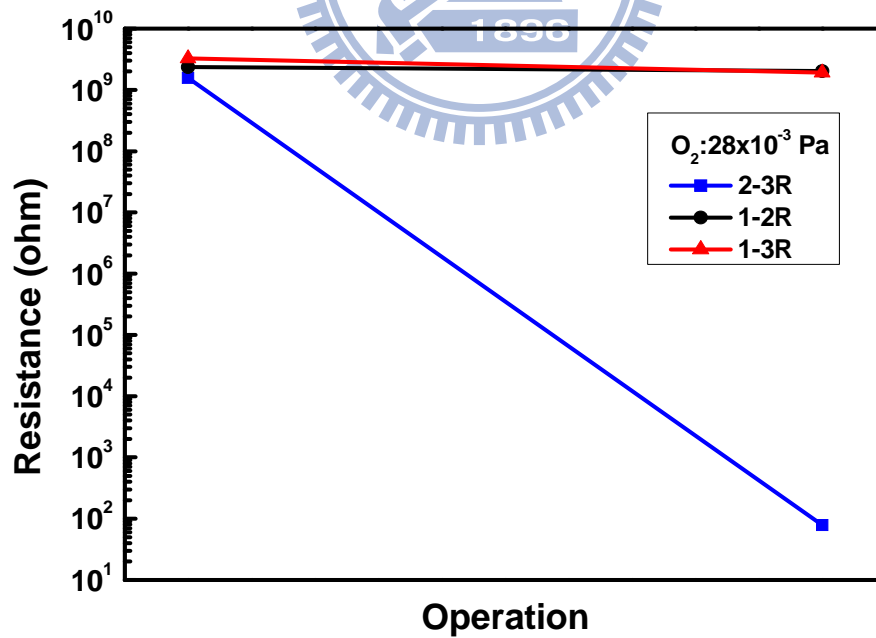


Fig. 4- 40 Resistances change of the different configuration after abnormal forming of the two pads test

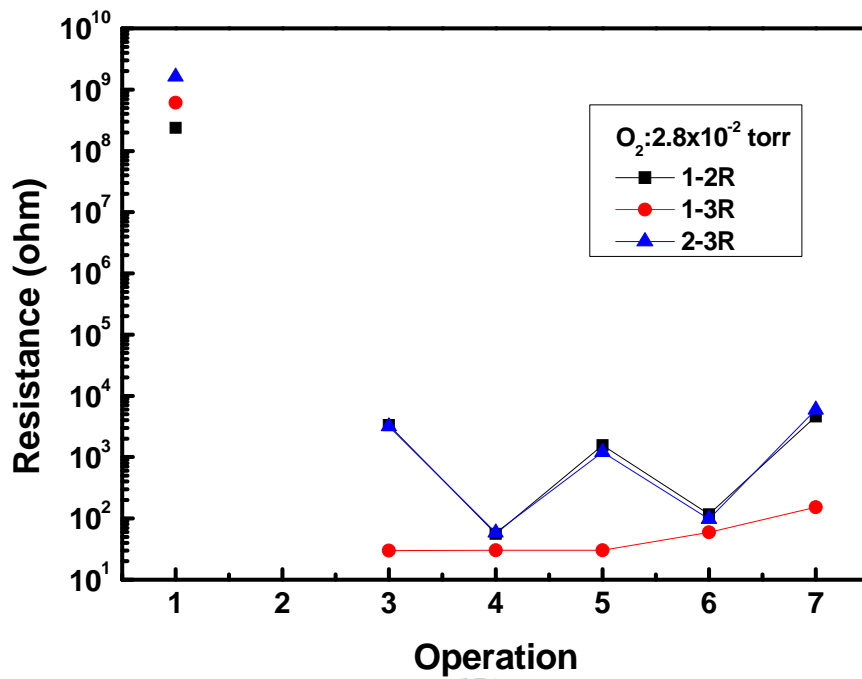


Fig. 4- 41 Resistances change of the different configuration After the subsequent reset and set processes of the two pads test

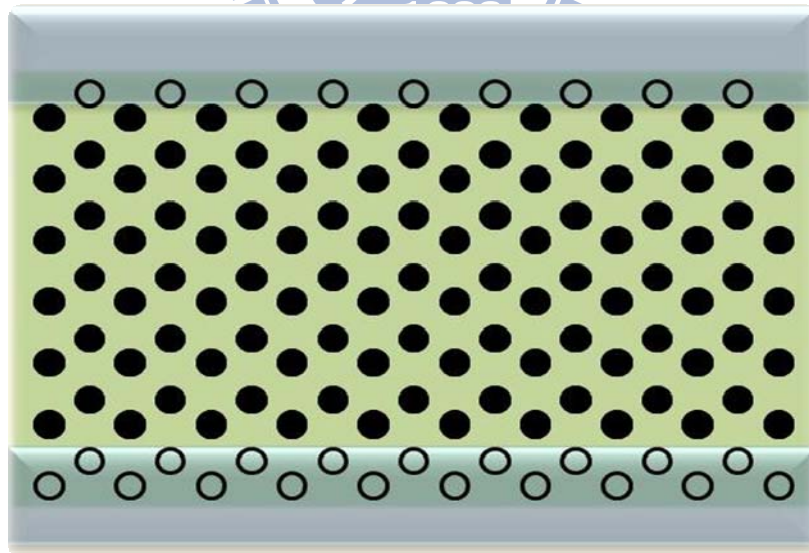


Fig. 4- 42 Pristine state of the ITO/LAO/ITO structure

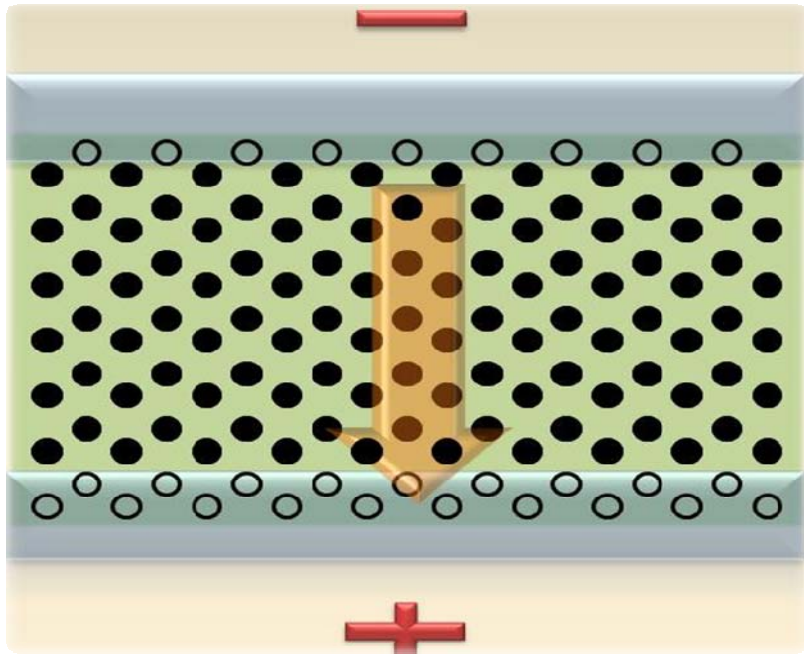


Fig. 4- 43 E-Field generated from the external bias lead to oxygen migration

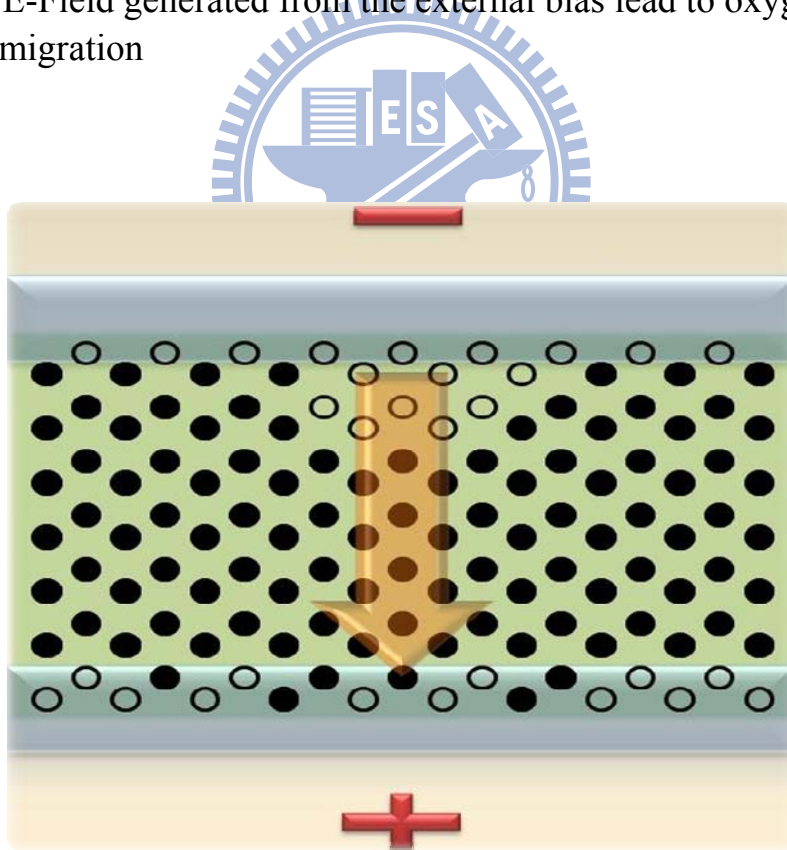


Fig. 4- 44 Oxygen migrate from the cathode to the anode

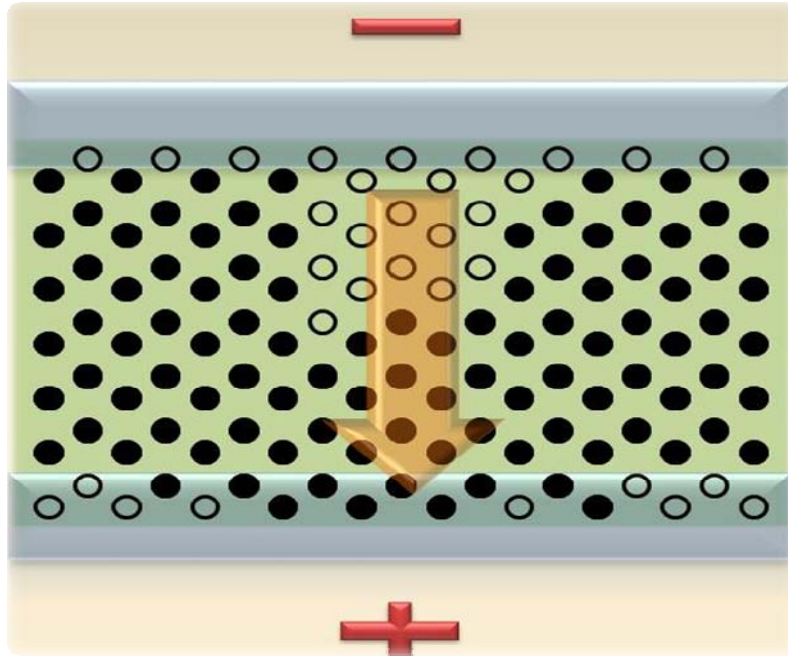


Fig. 4- 45 More vacancies migrate from the anode to the cathode

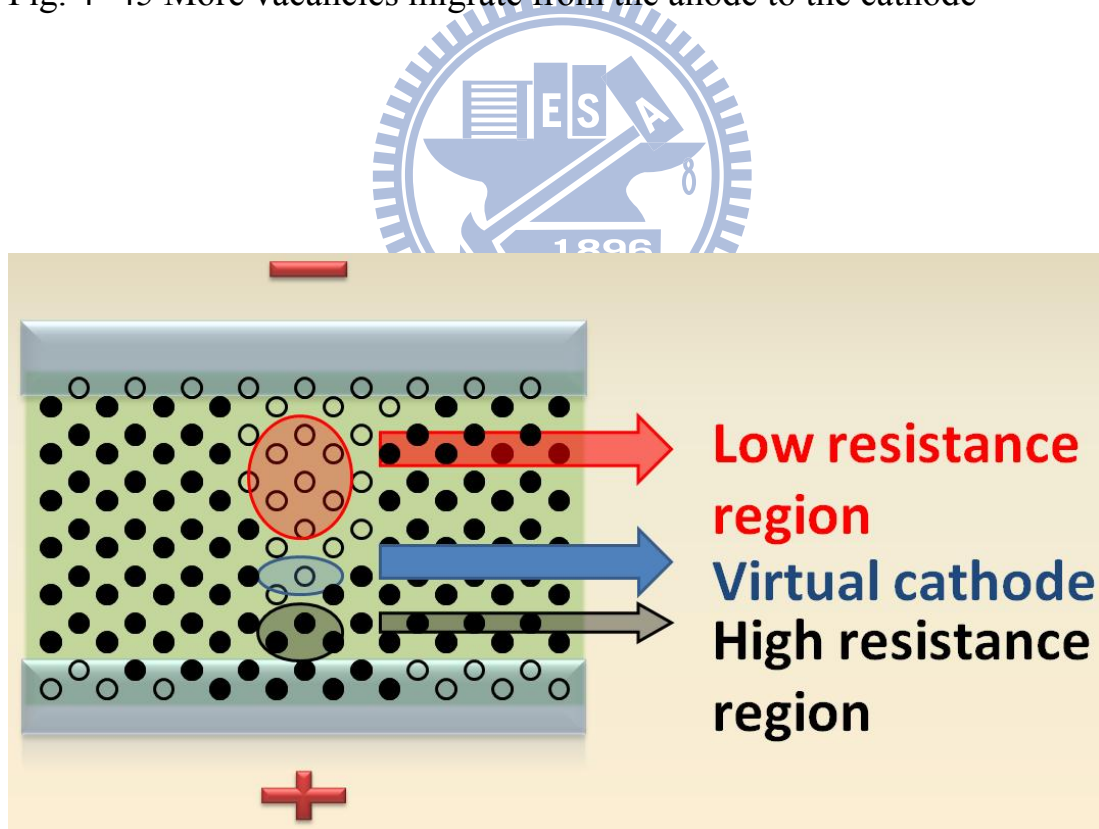


Fig. 4- 46 Regions near the anode and the cathode show different polarity and resistance result from the migration of the oxygen

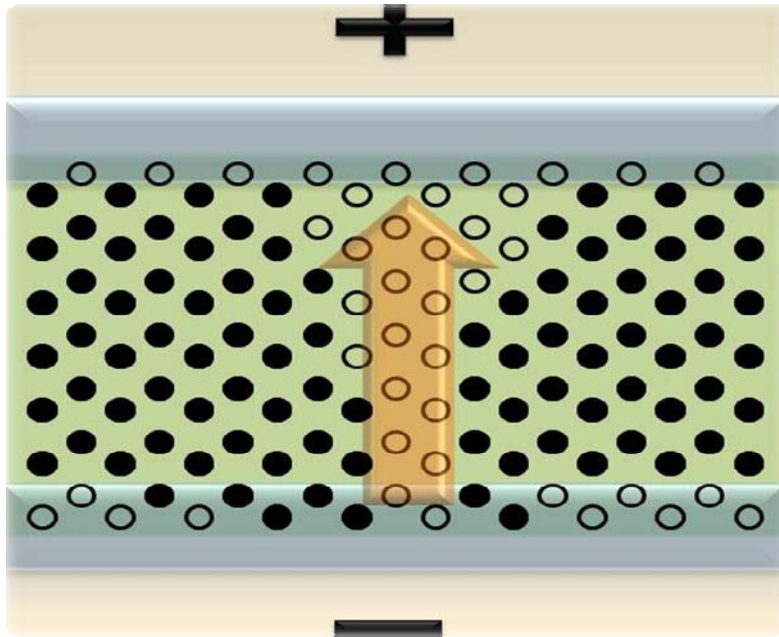


Fig. 4- 47 Reverse polarity of the E-Field leads to the migration of the oxygen from the cathode the to the anode

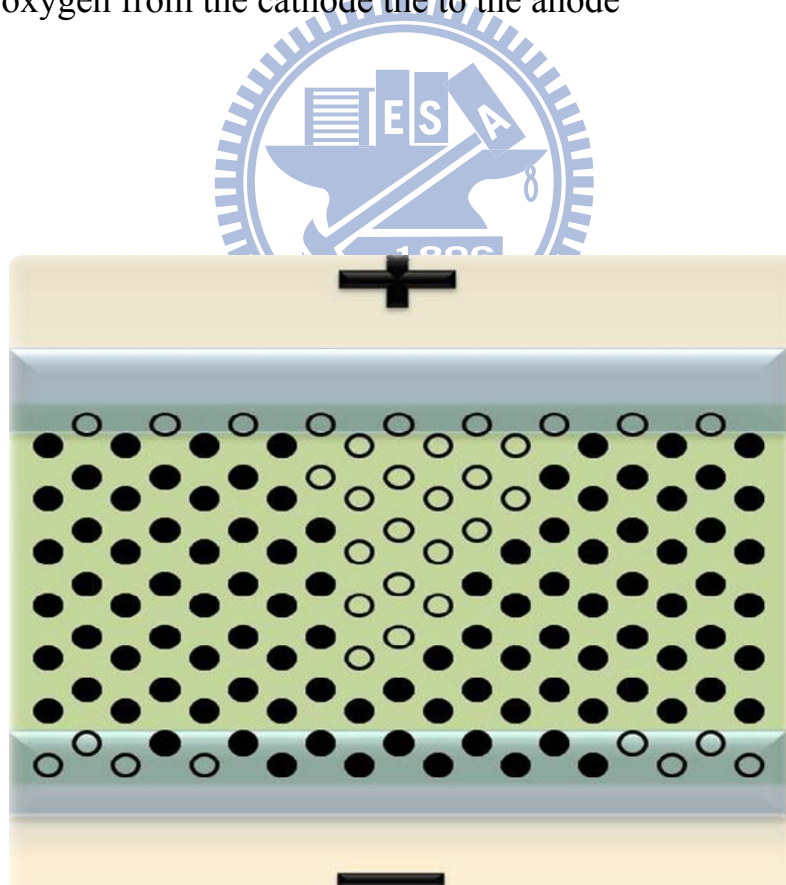


Fig. 4- 48 HRS after the reset operation

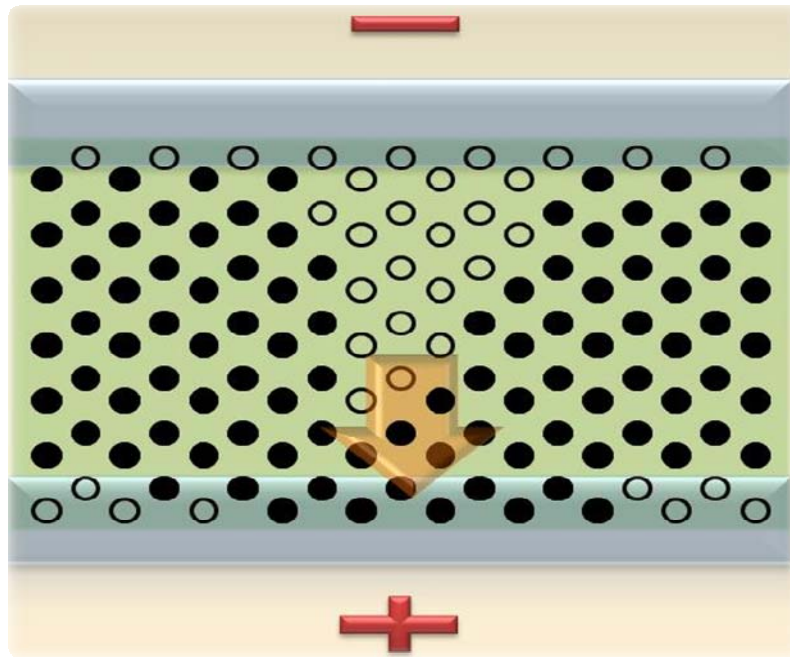


Fig. 4- 49 E-Field makes the oxygen migration from the virtual cathode to the anode

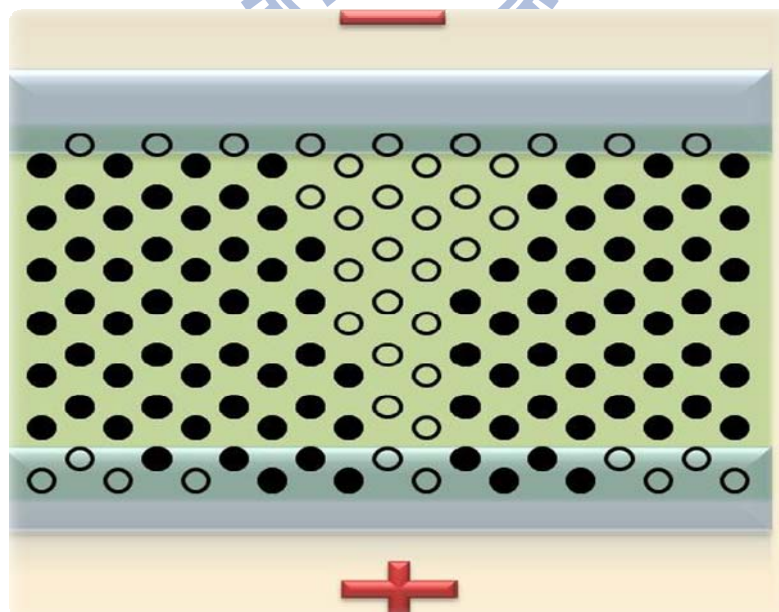


Fig. 4- 50 LRS after the set operation

Chapter 5 Conclusion

In this thesis, we succeeded using LaAlO_3 as resistive switching dielectric, and it shows good endurance, lower leakage current, and almost 1 order HRS/LRS ratio. The leakage current is a function of the oxygen pressure, so does the characteristic of the RS. The more oxygen pressure of the process we deposited in the less leakage current conducted through the oxide for the decreasing of the oxygen vacancies.

The mechanism of the resistive switching in ITO/ LaAlO_3 /ITO structure is oxygen migration. The E-Field generated from the external bias makes the oxygen migrated, and the resistance is changed by the different polarity of the external bias. The RS of the ITO/ LaAlO_3 /ITO is more stable in higher oxygen pressure the lower oxygen pressure in the process, for the more oxygen vacancies make RS unstable. During on state, the resistance changes from different magnitudes of the external bias. The lower the magnitude of the negative bias is applied, the lower LRS we can get it. During off state, the resistance changes from different magnitudes of the external bias. The higher the magnitude of the positive bias is applied, the high HRS we can get it. The multi-level characteristic of the RS in the ITO/ LaAlO_3 /ITO structure is possible.

In a word, the oxygen migration dominated the RS of the ITO/ LaAlO_3 /ITO structure.

Chapter 6 Future Work

We have succeeded in developing the fully-transparent RRAM device by using the LaAlO_3 as a resistive switching layer. In the future work, we have two parts to extend the research. One part is the research of the better characteristic in RRAM, and another part is the combination between the RRAM device and the transparent TFT.

The one part is the treatment. The heat effect and the number of the defects may affect the characteristic of the resistive switching. We proposed some future work.

1. annealing treatment to modify extra defects
2. nitridation to modify extra defects
3. multi-electrode for steady switching characteristic

Another part in future work is the combination of the RRAM and the transparent TFT. We used the function of the Agilent 4156C to restrict the current (I_{cc}) to prevent the device from hard breakdown. We must develop a circuit to replace the function of the machine. There are many papers discussing about the method of the circuits. For the request and the trend of the fully-transparent device, the combination of the transparent TFT and the RRAM we developed is necessary.

References

- [1] Takeshi, Yoshimura, Norifumi, Fujimura and Taichiro Ito, A.P.L., 73, 1998.
- [2] J.J. Yang, M.D. Pickett, X. Li, D.A.A. Ohlberg, D.R. Stewart and R.S. Williams, Nanotechnology (2008).
- [3] Rainer Waser, Regina Dittmann, Georgi Staikov and Kristof Szot, Adv. Mater., 21, 2632–2663, 2009.
- [4] Sheng-Yu Wang, Dai-Ying Lee, Tseung-Yuen Tseng and Chih-Yang Lin, A.P.L. 95, 112904, 2009
- [5] Kyung Min Kim, Byung Joon Choi, Seul Ji Song, Gun Hwan Kim and Cheol Seong Hwang, Journal of The Electrochemical Society, 156, G213-G216, 2009.
- [6] Jung-Bin Yun, Sejin Kim, Sunae Seo, Moun-Jae Lee, Dong-Chul Kim, Seung-Eon Ahn, Younsoo Park, Jiyoung Kim and Hyunjung Shin, phys. Stat. sol., 280-282, 2007.
- [7] Ruth Muenstermann, Regina Dittmann, Krzysztof Szot, Shaobo Mi, Chun-Lin Jia, Paul Meuffels and Rainer Waser, A.P.L., 93, 023110, 2008.
- [8] I.K. Yoo, B.S. Kang, Y.D. Park, M.J. Lee and Y. Park, A.P.L., 92, 202112, 2008.
- [9] A. Odagawa, H. Sato, I.H. Inoue, H. Akoh, M. Kawasaki and Y. Tokura, Physical Review B 70, 224403, 2004
- [10] R.E. Simpson, A. Mairaj, R.J. Curry, C.C. Huang, K. Knight, N. Sessions, M. Hassan and D.W. Hewak, 43, 2007.

- [11]A. Asamitsu, Y. Tomioka, H. Kuwahara and Y. Tokura, 388, 1997.
- [12]H.T. Yi, T. Choi and S.W. Cheong, A.P.L., 95, 063509, 2009.
- [13]Stefan Lai and Tyler Lowrey, IEEE, 2001.
- [14]Xin Guo and Christina Schindler, A.P.L., 91, 133513, 2007.
- [15]Yu Chao Yang, Feng Pan, Qi Liu, Ming Liu and Fei Zeng, 9, 1636-1643, 2009.
- [16]M.N. Jones, Y.W. Kwon and D.P. Norton, A.P.A, 81, 285-288, 2005.
- [17]R. Dong, D.S. Lee, M.B. Pyun, M. Hasan, H.J. Chol, M.S. Jo, D.J. Seong, M. Chang, S.H. Heo, J.M. Lee, H.K. Park and Hyunsang Hwang, A.P.A, 93, 409-414, 2008.
- [18]A. Sawa, T. Fujii, M. Kawasaki and Y. Tokura, Proc. Of SPIE, 5932, 2005.
- [19] S. Seo, M.J. Lee, D.C. Kim, S.E. Ahn, B.-H Park, Y.S. Kim and I.K. Yoo, A.P.L., 87, 263507, 2005.
- [20]T.Zhao, F. Chen, H.B. Lu, G.Z. Yang, J. Appl. Phys. 87, 7442 (2000)
- [21]S.H. Paek, J.H. Won and J.E. Jang, J. Mater. Sci. 31, 957, 2008.
- [22]Wenfeng Xiang, Huibin Lu, Lei Yan, Haizhing Guo, Lifeng Liu, Yueliang Zhou and Guozhen Yang, Journal of Applied Physics, 93, 2003
- [23]Y. Liu, H. Kim, J.J. Wang, H. Li and R.G> Gordon, ECS Transactions, 16 (5) 471~478, 2008
- [24]K.Xiong and J.Robertson, A.P.L., 89, 022907, 2006
- [25]T. Zhao, F. Chen, H.B. Lu, G.Z. Yang and Z.H. Chen, J. Appl. Phys., 87, 7442, 2000
- [26]S.H. Paek, J.H. Won and J.E. Jang, J. Mater. Sci.,31, 4357, 1996.
- [27]S. Choopun, R.D. Vispute, W. Noch, A. Balsamo, R.P. Sharma, T.

Venkatesan, A. Iliadis and D.C. Look, A.P.L., 75, 3947, 1999



簡 歷

- 基本資料

姓名：黃俊傑 (Jun-Jie Huang)

性別：男

生日：民國 74 年 10 月 21 日

住址：高雄市新興區林森一路 130 巷 2 號 2 樓

E-mail: kindy305@hotmail.com

- 學歷

國立清華大學動力工程學系 (93 年 9 月~97 年 9 月)

國立交通大學電子研究所碩士班 (97 年 9 月~99 年 9 月)

- 論文題目

脈衝雷射沉積鋁氧電阻層全透式電阻式記憶體研究

Pulse-laser deposition of LaAlO_3 as resistive switching layer of fully transparent resistive random access memory

- 社會服務

清華大學快樂兒童社社長

清華大學快樂兒童夏令營營長

清華大學動機營活動股長